ISSN : 2349-6495(P) | 2456-1908 (O)

International Journal of Advanced Engineering Research and Science

(IJAERS)

An Open Access Peer-Reviewed International Journal

Journal DOI: 10.22161/ijaers

Issue DOI: 10.22161/ijaers.112

AI PUBLICATIONS

Vol.- 11 | Issue - 2 | Feb 2024

editor.ijaers@gmail.com | editor@ijaers.com | https://www.ijaers.com/

International Journal of Advanced Engineering Research and Science (IJAERS)

(ISSN: 2349-6495(P)| 2456-1908(O))

DOI: 10.22161/ijaers

Vol-11, Issue-2

February, 2024

Publisher

AI Publication

Email: editor.ijaers@gmail.com; editor@ijaers.com

Web: www.ijaers.com

International Editorial/ Reviewer Board

Editor in Chief

- **Dr. Swapnesh Taterh (Chief-Editor),** Amity University, Jaipur, India

Cheif Executive Editor

- **S. Suman Rajest,** Vels Institute of Science, Technology & Advanced Studies, India chief-executive-editor@ijaers.com

Associate Editors

- **Dr. Ram Karan Singh,** King Khalid University, Guraiger, Abha 62529, Saudi Arabia
- **Dr. Shuai Li,** University of Cambridge, England, Great Britain

Editorial Member

- **Behrouz Takabi,** PhD, Texas A&M University, Texas, USA
- **Dr. Gamal Abd El-Nasser Ahmed Mohamed Said,** Port Training Institute (PTI), Arab Academy For Science, Technology and Maritime Transport, Egypt
- **Dr. Hou, Cheng-I ,** Chung Hua University, Hsinchu Taiwan
- **Dr. Ebrahim Nohani,** Islamic Azad University, Dezful, IRAN.
- **Dr. Ahmadad Nabih Zaki Rashed,** Menoufia University, EGYPT
- **Dr. Rabindra Kayastha ,** Kathmandu University, Nepal
- **Dr. Dinh Tran Ngoc Huy,** Banking and Finance, HCM, Viet Nam
- **Dr. Engin NAS,** Duzce University, Turkey
- **Dr. A. Heidari,** California South University (CSU), Irvine, California, USA
- **Dr. Uma Choudhary,** Mody University, Lakshmangarh, India
- **Dr. Varun Gupta,** National Informatic Center, Delhi, India
- **Dr. Ahmed Kadhim Hussein,** University of Babylon, Republic of Iraq
- **Dr. Vibhash Yadav,** Rajkiya Engineering College, Banda. UP, India
- **Dr. M. Kannan,** SCSVMV University, Kanchipuram, Tamil Nadu, India
- **José G. Vargas-Hernández,** University of Guadalajara Periférico Norte 799 Edif. G201-7, Núcleo Universitario Los Belenes, Zapopan, Jalisco, 45100, México
- **Dr. Sambit Kumar Mishra,** Gandhi Institute for Education and Technology, Baniatangi, Bhubaneswar, India
- **DR. C. M. Velu,** Datta Kala Group of Institutions, Pune, India
- **Dr. Deependra Pandey,** Amity University, Uttar Pradesh, India
- **Dr. K Ashok Reddy,** MLR Institute of Technology, Dundigal, Hyderabad, India
- **Dr. S.R.Boselin Prabhu,** SVS College of Engineering, Coimbatore, India
- **N. Balakumar,** Tamilnadu College of Engineering, Karumathampatti, Coimbatore, India
- **R. Poorvadevi,** SCSVMV University, Enathur, Kanchipuram, Tamil Nadu, India
- **Dr. Subha Ganguly,** Arawali Veterinary College, Sikar, India
- **Dr. P. Murali Krishna Prasad,** GVP College of Engineering for Women, Visakhapatnam, Andhra Pradesh, India
- **Anshul Singhal,** Bio Instrumentation Lab, MIT, USA
- **Mr. Lusekelo Kibona,** Ruaha Catholic University, Iringa, Tanzania
- **Sina Mahdavi,** Urmia Graduate Institute, Urmia, Iran
- **Dr. N. S. Mohan,** Manipal Institute of Technology, Manipal, India
- **Dr. Zafer Omer Ozdemir,** University of Health Sciences,Haydarpasa, Uskudar, Istanbul, TURKIYE
- **Bingxu Wang,** 2721 Patrick Henry St Apt 510, Auburn Hills, Michigan, United States

Vol-11, Issue-2, February 2024

(10.22161/ijaers.112)

Detail with DOI (CrossRef)

International Journal of Advanced Engineering Research and Science (IJAERS)
Peer-Reviewed Journal
ISSN: 2349-6495(P) | 2456-1908(O)
Vol-11, Issue-2; Feb, 2024
Journal Home Page Available: https://ijaers.com/
Article DOI: https://dx.doi.org/10.22161/ijaers.112.1

Galala Bridge Scour Model on Ambon's Way Ruhu River

Obednego D. Nara[1], Musper D Soumokil[1], Vector R.R Hutubessy[1], Denny Yatmadi[2]

[1]Department of Civil Engineering, Ambon State Polytechnic, Indonesia
[2]Department of Civil Engineering, Jakarta StatePolytechnic, Indonesia

Received: 17 Dec 2023,

Receive in revised form: 20 Jan 2024,

Accepted: 30 Jan 2024,

Available online: 11 Feb 2024

***Keywords*— Sccour, Contraction, Pier, Abutment, River**

Abstract— *The scouring that occurs on the abutments and pillars of the bridge is total scour, which is a combination of local scour and general scour. It can also be a combination of localized scour, generalized scour and localized scour / constriction scour. Bridge collapses are often the result of scouring. The potential for flooding can increase riverbed degradation, riverbed degradation and local scouring, which adds to the threat of bridge sub-structures. The galala bridge islocated in the lower reaches of the Way Ruhu river with a stretch length of 60 m. Physically, this bridge has been built for a long time so it needs to be evaluated for scour depth by mathematical modeling using the HEC-Ras 6.4.1 application. Scour modeling uses the CSU method and the Froechlich method. Based on the simulation results using three flow conditions against the 10, 25 and 50 year recurrence periods and using physical properties test data (grain size analysis, specific gravity test, and soil content weight test) from the Ambon State Polytechnic Material Test laboratory from soil samples around the Way Ruhu estuary showed that the scouring depth reached the base of the bridge, 2.00 m so that this scouring could affect the stability of the bridge and potentially collapse the bridge based on simulation with flood discharge plan 25 years.*

I. INTRODUCTION

A river is a channel of water that forms naturally on the face of the earth that flows from springs to its flow area according to the conditions of the earth's surface which eventually leads to the lowestarea. Water that flows continuously in the river willresult in the erosion of the bottom soil, continuous scouring forms scouring holes in the river bed. Theexistence of water buildings causes changes in flowcharacteristics such as speed and turbulence, causing changes in sediment transport and scouring. While *scouring* is a natural process that occurs in rivers due to the influence of river morphology, it can be in the form of bends or narrowing parts of river flow and can also be due to water buildings (*hydraulic structures*) such as bridges.

The scouring that occurs on the abutments and pillars of the bridge is total scour, *which is a combination of local* scour *and* general scour. It can also be a combination of localized scour, generalized scour and *localized scour / constriction scour*. Local scouring that occurs around bridge or pillar abutments is caused by a *vortex system* due to disturbances in flow patterns due to obstacles, and localized scouring occurs due to narrowing of the river cross-section by the placement of hydraulic buildings. This scour process can cause erosion and degradation around the *water way opening* of a bridge. This degradation continues continuously until a balance between sediment supply and transport is achieved. If the supply of sediment from upstream is reduced or the amount of sediment transport is greater than the supply of sediment, it can cause a very striking gap betweendegradation and degradation at the base location ofthe bridge waterway.

II. LITERATURE REVIEW

The process of erosion and deposition in rivers generally

occurs due to changes in flow patterns, especially in alluvial rivers. Changes in flow patterns can occur because there are obstacles or obstacles in the flow of the river. According to Raudkivi and Ettema (*Rinaldi, 2002*) the types of scour are as follows:

(1) *General scour* in river channels;

(2) Scour is localized in the river channel;

(3) Local scour around the building.

Local scour includes general scouring types and scour that occurs due to narrowing of the flow. Studying the scour process, it cannot be separated from studying the characteristics of existing sediments. The purpose of sediment transport is to determine whether under certain circumstances there will be *equilibrium*, erosion, or depostition and determine the quantity transported in the process. If the structure is placed in a water current, the flow of water around the structure will change, and the *vertical velocity gradient* of the flow will change to a *pressure gradient* at the end of the surface of the structure. This pressure gradient is the result of the underflow hitting the bottom of the channel. At the base of the structure, this lower flow forms a vortex that eventually sweeps around and the bottom of the structure by filling the entire flow. It is called the horseshoe vortex (Miller, 2003). On the surface of the water, the interaction of flow and structure forms a *bow wave* called a *surface roller*. When there is a separation of flow in the inner structure experiencing wake vortices.

2.1 Scour on the Bridge

Scour is the process of loss of sedimentary materialfrom the bottom and banks of rivers caused by thegrinding power possessed by the flow of water. Themost common cause of bridge failure is a large amount of riverbed material that is eroded andcauses degradation of the riverbed around the bridge foundation. This failure is caused by:

- Lack of knowledge about the scouringphenomenon during bridge construction.
- Lack of data and knowledge regarding floodplans.
- The rate of scour generally depends on:
- Water flow strength, material resistance, andin/out sediment balance (*equilibrium scour*).
- Material piled up due to riprap failure or cliffsaround the river.
- Erosion and failure of dikes with flows formedon two sides of the abutment.

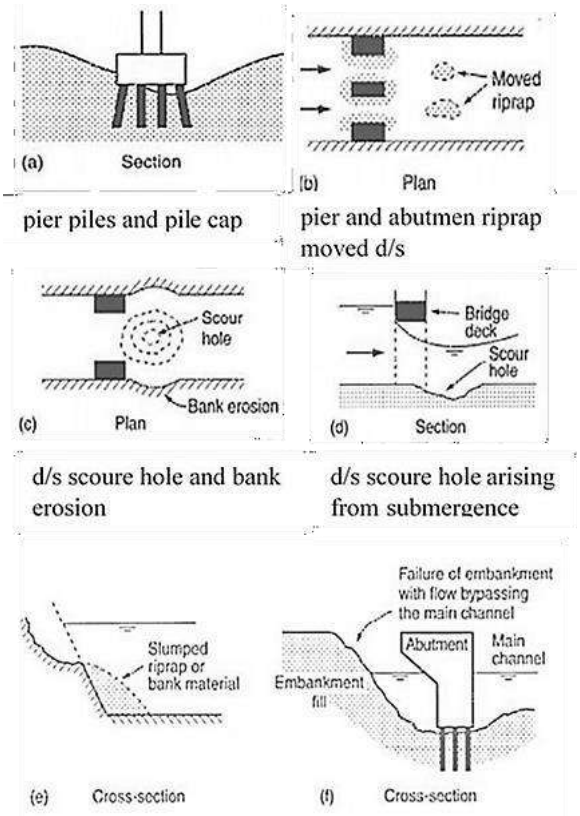

Fig.1 Scour on the Bridge

1. General scouring in river channels, is not related at all to the presence or absence of riverbuildings.
2. Local scouring in the river channel, occurs dueto the narrowing of the river flow to be centralized.
3. Local scouring around buildings, occurs due tolocal flow patterns around river buildings.

Scour of types (2) and (3) can then be divided into scouring with clean water (*clear water scour*) and scouring with sedimentary water (*lived bed scour*). Scour with clean water relates to a situation when the river bed upstream is stationary (no material is transported). While scouring with sediment occurs when flow conditions in the channel cause the base material to move. To determine flow conditions including clear-water or live-bed, the equation given by Neill (1968) below is used, for unobstructed river flow.

$$Vs = 1.58[(Ss-1)gD50]^{\frac{1}{2}}(\frac{y}{D50})^{1/6} \quad (1)$$

With SS = 2.65 (specific attraction for sediments), g = 9.81 m/s2 , D50 is the mean diameter (m) of sediment grain size 50%, Y = average depth (m) upstream. The above equation becomes.

$$V_S = 6{,}36\ Y^{1/6}\ D_{50}^{1/3} \quad (2)$$

During one flood period, the average speed will increase or decrease as the outflow of water also increases and decreases, so it is possible for the initial conditions to be

clear water *then* live bed *and finally clear water again.*

2.2 Local scour (pillars, abutments)

Local scouring results from increased currents passing under bridges and turbulent flows formed by river banks. Local scour occurs at a flow velocity when the transported sediment is greater than the sediment supplied. Sediment transport increases with increasing sediment shear stress andscouring occurs when flow conditions change causing an increase in base shear stress.

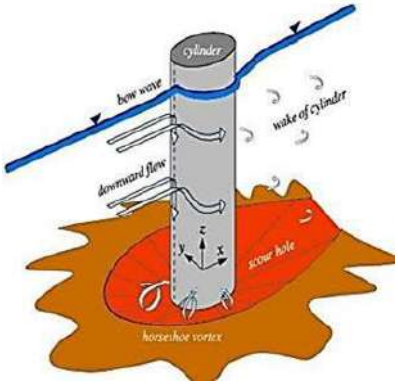

Fig.2 Local scour mechanism

The depth of scour on the pillars, the intensity depends on the flow, bottom sediments, and geometric disturbances of the bridge pillars. Scouraround the pillars begins to occur when the base material begins to move. Particles undergo erosionfollowing the direction of flow starting from the upstream to downstream of the pillar. The base material will continue to be eroded, and if the flowspeed increases, the size and depth of scour also increase.

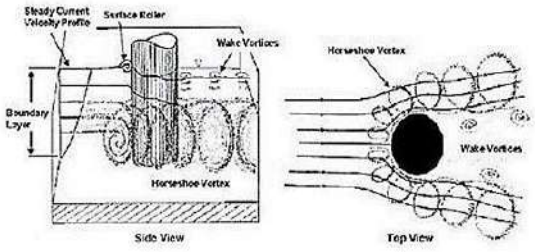

Fig.3 Scour Mechanism due to water Flow Pattern around Pillars

2.3 Rainfall frequency analysis

Rainfall analysis needs to be done to determine the maximum height of river water discharge so that the maximum flood height can be determined. Themaximum flood height is used to find the height ofthe bridge from the maximum flood water table, abutment height, and bridge span length.

The data used in the plan's precipitation analysis isthe average daily maximum rainfall intensity taking into account the dispersion of hydrological variables located or equal to their mean values, butthere may be values greater or smaller than their mean values. In flood estimation, it is necessary toestimate rain in advance which is called plan rain and flood estimation is also called plan flood. In flood estimation, the required parameters are Catchment Area area, rain plan height and flow coefficient.

2.4 Flow Coefficient

This drainage coefficient depends on the land use in the flow area. In this study the runoff coefficient must be adjusted to the development of the city, forthat the planned land use will be used in accordance with the applicable spatial plan land use directives.Each type of land use has a drainage coefficient (C)which is based on the allotment function and building density.

$$C = \frac{Runoff\ (mm)}{Curah\ Hujan\ (mm)} \qquad (3)$$

III. METHODOLOGY

To determine the natural phenomena that occur due to erosion of water flow at the base and cliffs of alluvial channels. So a mathematical model simulation was made using the HEC-RAS 6.4.1 device to find out the scouring that occurred. This application also provides the results of the process of decreasing piers and abutments to the riverbed below the natural surface elevation (*datum*) due to the interaction between the flow and the riverbed material.

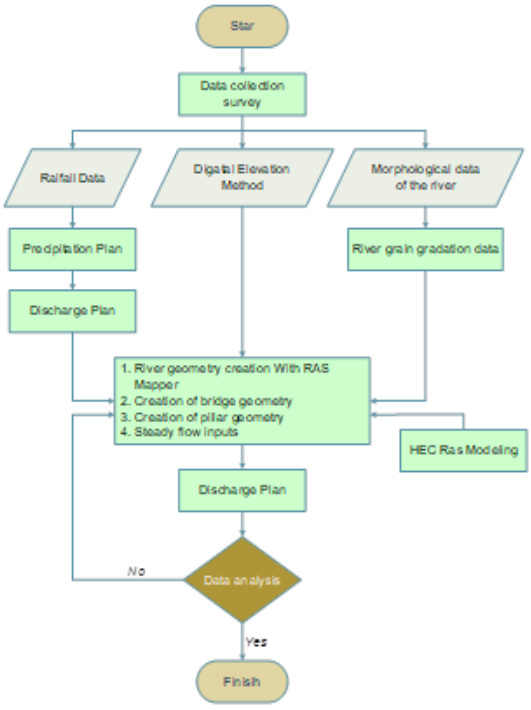

Fig.4 Research flow chart

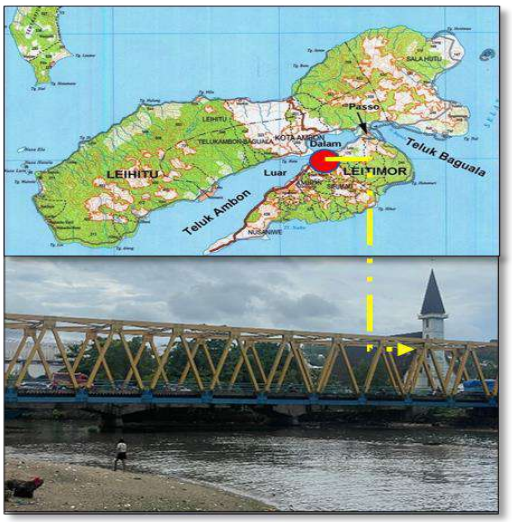

Fig.5 Study location

IV. RESULTS AND DISCUSSION

4.1 General State of Location

Way Ruhu watershed is located in the Great Watershed of Way Batu Merah with the area of Way Ruhu watershed is 1,629 Ha and is located in Sirimau District of Ambon City which is located in 4 villages namely Batu Merah, Galala, Hative Kecil and Halong.

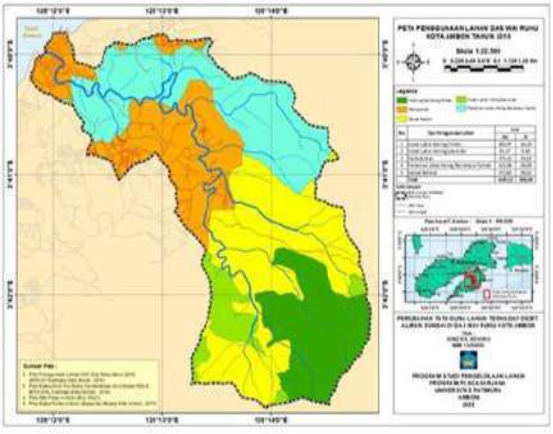

Fig.6 Map of Way Ruhu Watershed AmbonCity

4.2 Land Use

The factor of vegetation land cover is quite significant in reducing or increasing surface flow. Dense forests have a high level of land cover, so if rain falls on the rain area, this land cover factor slows down the surface flow speed, and can even occur near zero speed. The area of the Way Ruhu watershed is greater than 2000 Ha, based on research plans for land use in 2023 as shown in the table below.

Table 1 Land cover in 2023

Land Cover	2023			
	Area (Ha)	(%)	(C)	A x C
Primary Dryland Forest	264.97	16.26	0.3	79.49
Secondary Dryland Forest	187.33	11.50	0.35	65.57
Residential	393.89	24.18	0.25	98.47
Dryland Farming Mixed with Shrubs	379.07	23.27	0.7	265.35
Shrubbery	372.65	22.87	0.3	111.80
Savanna/Grassland/Empty Land	31.31	1.92	0.1	3.13
Total	1629.22	100.00		0.38

4.3 Discharge Frequency Analysis

Analysis of the frequency of discharge is carried out to determine the amount of discharge that occurs in a certain repeat period. Discharge frequency analysis includes determining the type of discharge distribution, then calculating the amountof discharge based on the repeat period using an equation corresponding to the type of distribution.The type of discharge distribution depends on the value of statistical parameters, namely the mean (*X*), standard deviation (*Sd*), coefficient of astonishment (*Cs*), coefficient of variation (*Cv*) and coefficient of curtosis (*Ck*).

Table 2. Distribution Selection Requirements

No	Distribution Type	Available	Calculations	Summary
1	Normal	CS ≤ 0 CS =	2.207	Not compliant
		CK = 3 CK =	-1.43	Not compliant
2	Log Normal	CS = 1.137 CS =	2.207	Not compliant
		CV = 5.383 CK =	2.21	Not compliant
3	Log Pearson III	CS ≠ 0 CS =	2.207	Not compliant
		CV = 0.3 CV =	0.64	*Meet*
4	Gumbel	CS ≤ 1.139 CS =	2.207	Not compliant
		CK ≤ 5.402 CK =	-1.428	Not compliant

From the distribution selection requirements, there are qualified Pearson III logs so that the results of calculating the maximum rainfall re-period with the Pearson III log method for 10, 25 and 50 year re-periods can be seen in the following table.

Table 3. Log Pearson III Maximum Rainfall

RRP	KTr	LogXTr	XTr(mm)
10	1.337	3.009	1021.122
25	2.128	3.085	1216.392
50	2.703	3.140	1381.225

4.4 Plan Flood Discharge Calculation

A commonly used peak flow rate analysis is the rational method of USSCS (1973). The rational method was developed based on the assumption that the rain that occurs has a uniform intensity andevenly distributed throughout the DPS as long as itis at least equal to the time of DPS concentration. After obtaining the flow coefficient (*C*), rainfall intensity (*I*), and drainage area (*A*) then calculated

the peak discharge from the sub-watershed with a rational method.

Table 4 Rational Plan Flood Discharge

Tr	C	A	I	Q
10	0.37	1629.2	25.20	41.89
25	0.37	1629.2	63.00	104.71
50	0.37	1629.2	125.99	209.43

4.5 Gradation Relationship and Grain Uniformity

The analysis carried out is a sieve analysis that aims to determine the percentage of sediment for each specific grain size. From the results of sieve analysis, it can be known the characteristics of the sediment reviewed in the form of grain size distribution graphs. The sieve analysis results for sediment samples taken in Way Ruhu River, while for the table of the percentage of granules that escaped for each sieve can be seen in the following figure.

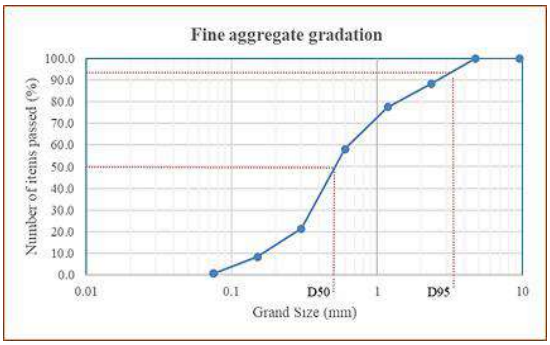

Fig.7. Graph Sediment Sieve Analysis

4.6 Simulated Local Scour on Bridges

Simulating local scour that occurs on the pillars ofthe Way Ruhu Bridge in Galala village using the unsteady flow option contained in the HEC-RAS

6.4.1 program and knowing in local scouring that occurs using hydraulic design after running with HEC-RAS. To run the simulation, the data that has been analyzed previously will be included as imputdata in the HEC-RAS 6.4.1 program. In general, the required data input is:

1) Cross-sectional geometry of the channel.
2) Bridge geometry.
3) Discharge data that will pass at the bottom of the bridge.
4) Sedimentary grain sizes d50 and d95.

After all the geometric data of the bridge is enteredin the HEC-RAS program, it must then be run usingsteady flow simulation.

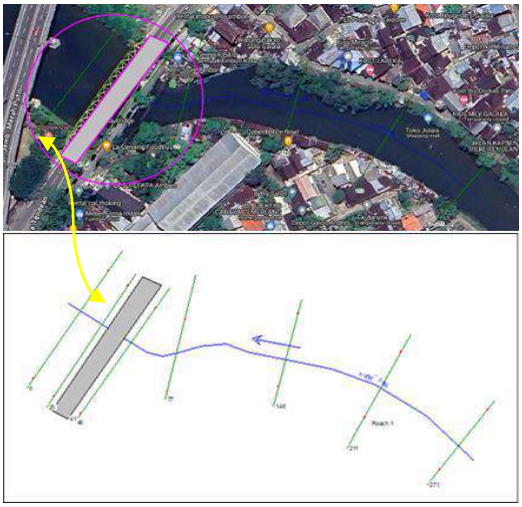

Fig.8 Geometrics of the Way Ruhu River

After all data is inputted based on criteria and river characteristics, from the results of flow simulation in three different flow discharge conditions, the maximum water level difference is obtained in the downstream flow conditions of the bridge and the flow conditions upstream of the bridge as shown below.

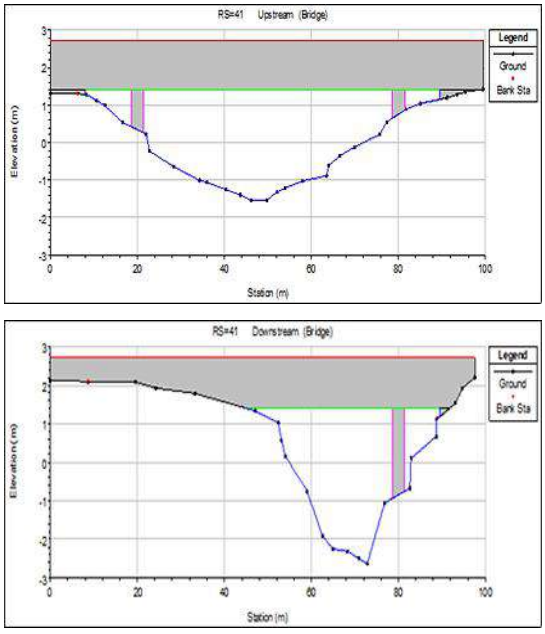

Fig.9 Condition of Existing Model of Bridge

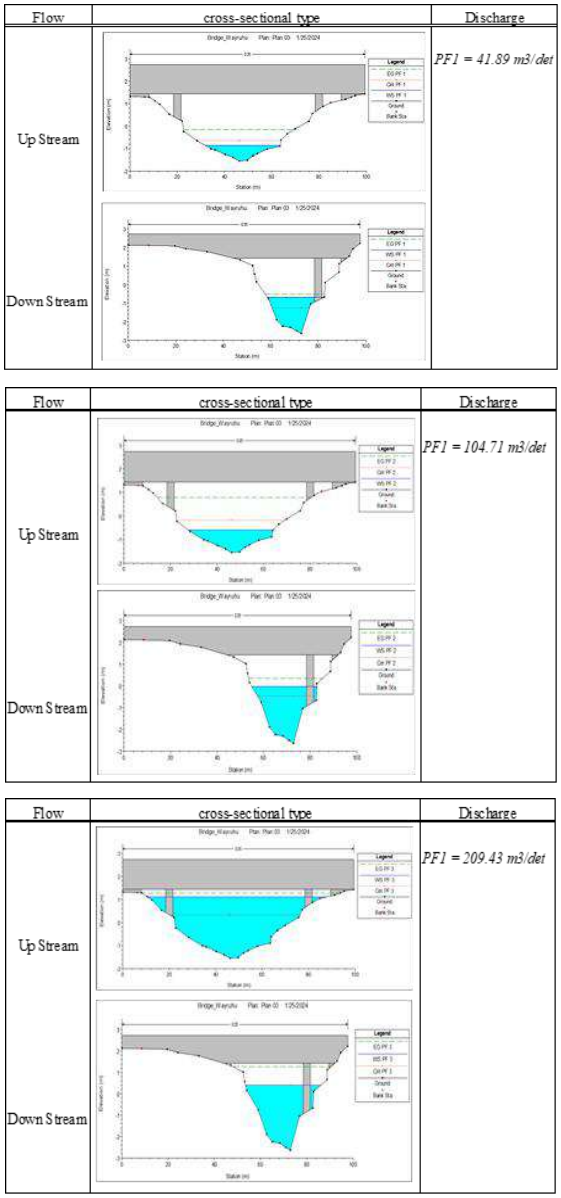

Fig.10 Simulated flow against a bridge

4.7 Analysis of local scour that occurs on the bridge

After running steady flow to determine the amount of local scouring that occurs due to discharge passing through the Way Ruhu, using the analysis in the HEC-RAS program on the perform hydraulic design computation menu. In hydraulic design there are three kinds of scour analysis that can occur. Contraction,pierand abutment.In ontraction scour, almost all data needed to calculate contraction scouring have been automatically taken by the HEC-RAS program from the output of flow calculation results in the selected cross section, namely in the upstream and approach flow. The data that must be inputted is d50 in millimeters and the coefficient K1 as can be seen in. In this study, the diameter of the d50 sediment was 0.20 mm and the d95 was 2.3 mm. The HEC-RAS program calculates the pier scour with the CSU (*California State University*) or Froehlic equation. There are 4 types of data needed, namely the shape and dimensions of the pillars, the angle of incidence of flow to the pillar (*angle*), the shape of the river bed (K3) and the diameter of the sediment (d95). From the results of the HEC-RAS analysis above, the depth of local scour that occurs at the bottom of the bridge is obtained based on the cross-section of the sudetan plan and also the flow discharge that has been entered using a flow hydrograph.

From the results of the scour simulation at the footof the bridge, the condition at PF 3 (*50-year plan discharge*) did not occur contraction and change inthe abutment due to the planned flood discharge water table being at the foot of the abutment whichcaused the bridge structure not to contract becauseno pressure occurred. From the results of the HEC-RAS simulation of the Way Ruhu bridge, the depthof local scour that occurs at the bottom of thebridge is as follows:

Table 5 Scour simulation results

Debit (m3/det)	Section	Contraction (m)	Pier (m)	Abutmen (m)	Total (m)
PF1 = 41.89	Left	0.21	0.96	1.17	1.38
	Channel	0.21	0.96	-	1.17
	Right	0.21	0.96	1.17	1.38
PF1 = 104.71	Left	0.43	1.13	1.57	2.00
	Channel	0.43	1.13	-	1.56
	Right	0.43	1.13	1.57	2.00
PF1 = 209.43	Left	0	1.26	0	1.26
	Channel	0	1.26	-	1.26
	Right	0	1.26	0	1.26

From the results of maximal scour modeling in the Way Ruhu River with three discharge model conditions for the 10, 25 and 50 Year re-periods as shown in table 5 shows that the scouring depth in PF2 conditions (25-year plan discharge) in pillar 1 and pillar 2 is the same, because the shape and size of pillar 1 and pillar 2 are the same. Similarly, the depth of scour in both the left abutment and the right abutment is the same, because the shape and size of the left abutment and right abutment are the same. Where in this condition there is a maximum scouring depth around the pillars.

4.8 Protection against scour on the bridge

Based on the results of modeling with HEC RAS, the scouring that occurred on the left and right piers and abutments as deep as 2.00 meters with a 25- year plan discharge simulation, it is necessary to carry out Operation and Maintenance actions on scouring protection on the Galala Bridge. From these results, there is a need for protection to anticipate structural failure due to continuous scouring. There are several kinds of scour control methods, including:

1. With the installation of a rip-rap floor around the pillars.

2. Creation of foundation blocks around pillars in the river bed.
3. Placement of pseudo-pillars in font (*upstream*) of the real pillars.
4. Placement of pillars in the direction of the flow.
5. Changes in the shape of pillars that can reduce flow resistance.

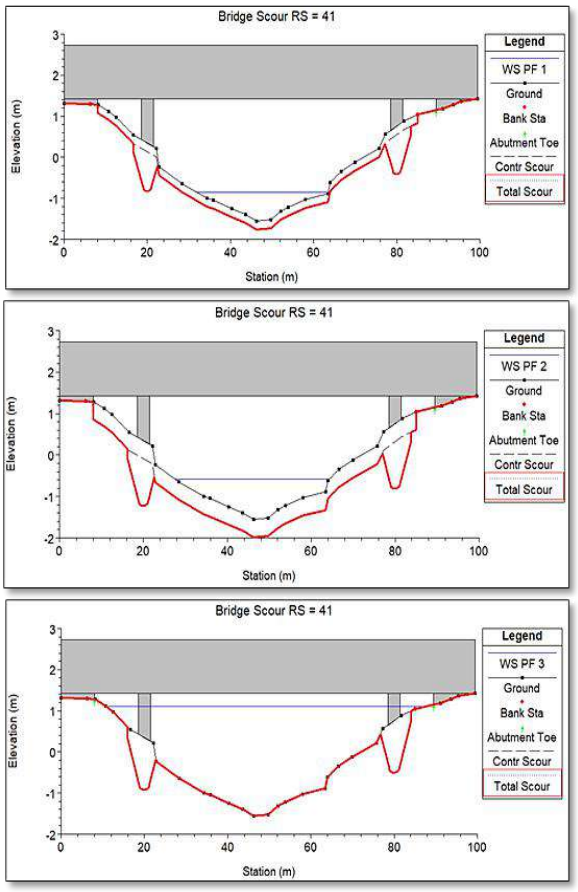

Fig.11 Simulated scour on a bridge

V. CONCLUSION

1) The scouring that occurs on the bridge is caused by a layer of soil with small grains. From the results of HECRAS simulations show that the scouring depth reaches the base of the bridge, 2.00 m. This scouring can affect the stability of the bridge and potentially collapse the bridge.
2) One way to evaluate bridge damage due to scouring is to conduct regular visual inspections.
3) In addition, analysis of weather data and water flow around the bridge can also be carried out to understand the potential for scouring that occurs. By conducting periodic evaluations, it can help in determining the necessary corrective actions to prevent further damage to the bridge due to scouring.

REFERENCES

[1] Barokah, I. and Purwantoro, D., 2014. The effect of flow discharge variations on maximum scour in bridge buildings using the HEC-RAS program. INERTIA.
[2] Breusers, H.N.C and Raudkivi, A.J. 1991. Scouring. Netherlands: A.A. Balkema.
[3] Budianto, Bambang S; Djuwadi; Muttaqin, A. Salim; Karnisah, Iin; Astor, Yackob. 2020. "Impact evaluation of Cilember River normalisation to Purbaleunyi Toll Road using two dimensional model HEC-RAS" IOP Conf. Series: Materials Science and Engineering 830 (2020) 022027 IOP Publishing doi:10.1088/1757- 899X/830/2/ 22027, ICIEVE 2019
[4] Fuad Halim, 2014 ; Effect of discharge on surrounding scouring patterns bridge abutments (laboratory tests on scale megawati bridge model); Media Engineering Scientific Journal Vol.4 No.1, March 2014 (32-40) ISSN: 2087-9334
[5] Hao Wang, Hongwu Tang; Local Scouring around Twin Bridge Piers in Open-Channel Flows. Journal of Hydraulic Engineering Volume 142, Issue 9 https://doi.org/10.1061/(ASCE)HY.1943-7900.0001154
[6] Melville, B. W., 1995. Bridge Abutment Scour In Compound Channels. Journal of Hydraulic Engineering, Vol 121, No. 12, pp. 863-868. ASCE, New York.
[7] Moussa, Ahmed Moustafa Ahmed. 2018. "Evaluation of local scour around bridge piers for various geometrical shapes using mathematical models" Ain Shams Engineering Journal, Volume 9, Issue 4, December 2018, Pages 2571-2580.
[8] Nasr, A.; Kjellström, E.; Björnsson, I.; Honfi, D.; Ivanov, O.L.; Johansson, J. Bridges in a changing climate: A study of the potential impacts of climate change on bridges and their possible adaptations. Struct. Infrastruct. Eng. 2019, 1–12.
[9] Richardson, E.V.; Davis, S.R. Evaluating Scour at Bridges; Hydraulic Engineering Circular (HEC) No. 18; U.S. Department of Transportation: Washington, DC, USA, 2001.
[10] Varaki, Mahdi Esmaeili; Radice, Alessio; Hossini, Seyyedeh Samira; Ola, Ramin Fazl. 2019. "Local Scour at a Complex Pier with Inclined Columns Footed on Capped Piles: Effect of the Pile Arrangement and of the Cap Thickness and
[11] Waqed H. Hassan, Halah K. Jalal; Prediction of the depth of local scouring at a bridge pier using a gene expression programming method. SN Applied Sciences (2021) 3:159 https://doi.org/ 10.1007/s42452-020-04124-9.

International Journal of Advanced Engineering Research and Science (IJAERS)
Peer-Reviewed Journal
ISSN: 2349-6495(P) | 2456-1908(O)
Vol-11, Issue-2; Feb, 2024
Journal Home Page Available: https://ijaers.com/
Article DOI: https://dx.doi.org/10.22161/ijaers.112.2

The Role of the Microbiome in Antibiotic Resistance and Infection Control

Djosci Coêlho de Sá Júnior[1*], Ricardo Baroni Vieira[2], Ana Claudia Borges Braga[2], Hellen Kristina Magalhães Brito[2], Giovanna Uchôa de Souza Cruz[2], Guilherme de Almeida Leite Furtado[2], Victoria Carolinne Oliveira Silva[3], Karina Meira de Miranda[3], Felipe Machado Dourado Bastos[3], Luiza Valesca Barros Teixeira[3], Hugo Soares Lira Azevedo[3], Laura Maria Lopes Sá Luz Costa[3], Isabela Godoy Santos[3], Ana Clara Souza Barreto da Cunha[3], Lucca Pazini Meneghel Paiva[4], Ana Luiza de Pellegrini Maciel Zanina[5], Karollyne Nunes Marinho[5]

[1]Medical Intern, University of Gurupi (UnirG), Gurupi, Brazil.
[2]Medical Resident, Department of Internal Medicine, Palmas General Hospital (HGP), Federal University of Tocantins (UFT), Palmas, Brazil.
[3]Medical Intern, University of Gurupi (UnirG), Gurupi, Brazil.
[4]Medical Intern, President Antônio Carlos Tocantinense Institute (ITPAC), Palmas, Brazil.
[5]Medical Student, University of Gurupi (UnirG), Gurupi, Brazil.
*Corresponding author. Email: djosci@outlook.com.

Received: 05 Dec 2023,
Receive in revised form: 15 Jan 2024,
Accepted: 28 Jan 2024,
Available online: 11 Feb 2024

***Keywords*— Microbiome, Antibiotic Resistance, Infection Control, Therapeutic Strategies, Microbial Communities**

***Abstract*—** *This review explores the critical role of the microbiome in modulating antibiotic resistance and its implications for infection control. By synthesizing recent research, we highlight how microbial communities influence the emergence and dissemination of antibiotic resistance genes and their impact on host health and disease outcomes. The interplay between the microbiome and antibiotics suggests a need for novel strategies to manage resistance, emphasizing microbiome-preserving approaches. Our findings underscore the potential of leveraging microbiome insights to develop more effective infection control practices and antibiotic use policies, aiming to mitigate the global challenge of antibiotic resistance. Future research directions are suggested to further understand the microbiome's mechanisms in resistance and identify therapeutic opportunities for enhancing human health.*

I. INTRODUCTION

The human microbiome, a diverse community of microorganisms residing in and on the human body, is crucial for maintaining health and influencing disease. This complex ecosystem includes bacteria, viruses, fungi, and protozoa, with the highest concentrations found in the gut, skin, mouth, and respiratory tract (Koenig et al., 2010). The microbiome plays a vital role in digesting food, synthesizing essential vitamins, and regulating the immune system, extending its influence beyond simple pathogen resistance (Ogunrinola et al., 2020). The composition and diversity of microbial communities vary significantly across different body sites, reflecting the unique environmental conditions and functions of each location (Koenig et al., 2010). Factors such as genetics, age, diet, and antibiotics influence the microbiome's composition, leading to a highly personalized microbial fingerprint for each individual (Ogunrinola et al., 2020). The interplay between

the microbiome and the human host is a fine balance, where both benefit from each other in a symbiotic relationship (Ogunrinola et al., 2020). Disruptions in this balance, whether through antibiotic use, dietary changes, or illness, can have profound health implications (Ogunrinola et al., 2020).

Recent research has highlighted the microbiome's role in a broad spectrum of health and disease states, extending beyond traditional boundaries of infectious diseases to conditions like obesity, diabetes, allergies, and mental health disorders (Ogunrinola et al., 2020). The concept of the "core" microbiome, a set of microbial species common to most healthy individuals, is central to understanding human microbial diversity (Ogunrinola et al., 2020). Identifying and understanding these core elements are crucial for deciphering how variations in the microbiome relate to disease (Ogunrinola et al., 2020). Lifestyle factors, particularly diet, have a profound influence on microbial composition and diversity, with high-fiber diets promoting a diverse and stable microbiome (Zangara & McDonald, 2019). Physical activity and exposure to natural environments have also been shown to positively influence microbial diversity (Zangara & McDonald, 2019).

In summary, the human microbiome is a complex and dynamic community that plays a critical role in health and disease. Its diversity and composition are influenced by a myriad of factors, making it a central focus in understanding human physiology and developing new approaches to disease prevention and treatment (Ogunrinola et al., 2020). As research progresses, the potential to manipulate the microbiome for therapeutic purposes offers exciting possibilities for future medical advances (Ogunrinola et al., 2020).

II. MECHANISMS OF ANTIBIOTIC RESISTANCE

The misuse and overuse of antibiotics have accelerated the selection for resistant strains and altered the balance of the microbiome, leading to a decrease in microbial diversity and the proliferation of antibiotic-resistant bacteria. Horizontal gene transfer (HGT) within microbial communities, facilitated by mobile genetic elements, accelerates the dissemination of resistance traits, making once-treatable infections increasingly difficult to combat. The emergence of multidrug-resistant (MDR) pathogens, particularly in environments with frequent antibiotic use, poses significant challenges, leading to challenging hospital-acquired infections. Additionally, antibiotics released into the environment through pharmaceutical waste and agricultural runoff can select for resistant bacteria in soil and water, contributing to the environmental reservoir of resistance genes (Gullberg et al., 2011).

The impact of antibiotics on the natural microbiota, including probiotic bacteria, can lead to diminished colonization resistance against pathogenic bacteria, increasing infection risks and contributing to the cycle of resistance (Bakkali, 2013). Recent studies have highlighted the gut microbiome's role in metabolizing and modifying antibiotics, affecting drug efficacy and resistance development (Ashiru-Oredope et al., 2022). Antibiotic stewardship programs aim to optimize antibiotic use, reducing unnecessary exposure and slowing resistance development (Laurenceau et al., 2013). Emerging research is exploring the development of narrow-spectrum antibiotics and bacterial interference as potential strategies to combat antibiotic resistance (Sharkey et al., 2016).

Competing evidence suggests that the widespread misuse of antibiotics may not only be selecting for resistant strains but also causing bacteria to take up more DNA, increasing the chances of acquiring drug resistance and virulence. Additionally, there is evidence that antibiotics targeting DNA replication cause an increase in the copy number of genes proximal to the origin of replication, triggering bacterial competence and gene transfer (Ashiru-Oredope et al., 2022). Furthermore, the competitive trade-off limits the selective advantage of increased antibiotic production, indicating that producer colonies can benefit from inhibiting nearby sensitive colonies, but this benefit is shared with resistant colonies growing in their vicinity (Slager et al., 2014).

Understanding the mechanisms of antibiotic resistance and the role of the microbiome in this process is crucial for developing strategies to combat the growing threat of resistant infections. A multifaceted approach, incorporating antibiotic stewardship, targeted therapies, and microbiome preservation strategies, is essential for safeguarding the effectiveness of antibiotics for future generations.

III. MICROBIOME AND DISEASE SUSCEPTIBILITY

Competing evidence suggests that the relationship between the microbiome and disease susceptibility is complex and multifaceted, involving direct microbial competition, immune modulation, and systemic health effects. While the protective role of a healthy microbiome against pathogenic invasion is well-established, there is evidence that the microbiome can exclude pathogens by competing for common host resources, including nutrients and receptors Baerentsen et al. (2022). Additionally, the gut microbiome has been linked to the pathogenesis of multiple sclerosis, suggesting that the commensal microbiota has a role in the

development of autoimmune diseases (Berer et al., 2017). Furthermore, the respiratory microbiome has been shown to influence chronic lung disease exacerbations, indicating a role in disease development (Adar et al., 2016).

Moreover, the impact of the microbiome on vector competency through induced immunological responses, morphological changes, or direct competition between microbial components of the tick microbiome highlights the complexity of microbiome interactions and their influence on disease susceptibility (Ring et al., 2021). There is also evidence that prenatal maternal diet and infant and child nutrition impact the infant microbiome trajectory and immune competence development, suggesting that early-life exposures play a critical role in immune system development and disease susceptibility (Dogra et al., 2021).

Furthermore, the concept of a trade-off in host innate immunity and protective microbiome indicates that there may be conflicting effects of the microbiome on disease susceptibility, suggesting that the relationship is not always straightforward (Jervis et al., 2021). Additionally, the opposite evidence suggests that with less gut microbiome diversity, microbiota labor together to create energy desires in the host, indicating that the impact of the microbiome on disease susceptibility may not always be protective (Li et al., 2021).

The interplay between the microbiome and disease susceptibility is complex and multifaceted, involving direct microbial competition, immune modulation, and systemic health effects. Understanding and manipulating this relationship holds the key to developing new strategies for disease prevention and treatment, emphasizing the importance of maintaining a healthy and balanced microbiome. While the protective role of a healthy microbiome against pathogenic invasion is well-documented, the competing evidence highlights the complexity of the microbiome's influence on disease susceptibility, indicating that the relationship is multifaceted and may involve conflicting effects on host health and disease susceptibility.

IV. MICROBIOME-BASED THERAPIES

Competing evidence suggests that while microbiome-based therapies, such as fecal microbiota transplants (FMTs), probiotics, and prebiotics, have shown promise in restoring microbial balance and treating infections, there are complexities and challenges that need to be considered. For instance, the relationship between the gut microbiome and neurodegenerative diseases is increasingly plausible, indicating that the microbiome may have a broader impact on health beyond infectious diseases (Xiao-hong et al., 2021). Additionally, the gut microbiome has been linked to the modulation of the immune system and response to anti–PD-1 immunotherapy in cancer patients, suggesting a systemic influence of the microbiome on disease treatment and prevention (Gopalakrishnan et al., 2018). Furthermore, the efficacy of current microbiome-based therapies in treating obesity is being discussed, indicating that the impact of these therapies may extend to metabolic disorders (Lim et al., 2020).

Competing evidence also suggests that the gut microbiome can substantially affect the effectiveness of chemotherapy and immunotherapy, indicating that the microbiome may influence the response to various cancer treatments (Huang et al., 2021). Moreover, the microbiome has been associated with the modulation of host immunity, metabolism, and extraintestinal tumors, indicating a systemic influence of the microbiome on health and disease (Zhang et al., 2019). Additionally, microbiome-based therapies are being investigated to mitigate antibiotic-induced microbial perturbation, highlighting the potential broader applications of these therapies beyond infectious diseases (Theodosiou et al., 2023).

Furthermore, the microbiome has been associated with the modulation of the immune system and response to anti–PD-1 therapy in melanoma patients, indicating that the microbiome may influence the response to cancer immunotherapy (Davar et al., 2021). The gut microbiome has also been linked to the response to immune checkpoint blockade across cancer types, suggesting a systemic influence of the microbiome on cancer therapy (Gopalakrishnan et al., 2018). Additionally, the microbiome has been associated with the modulation of the immune system and response to anti–PD-1 therapy in melanoma patients, indicating that the microbiome may influence the response to cancer immunotherapy (Davar et al., 2021).

In conclusion, while microbiome-based therapies show promise in restoring microbial balance and treating infections, competing evidence suggests that the influence of the microbiome extends beyond infectious diseases to systemic health effects, cancer treatment, and immune modulation. These complexities and broader implications of the microbiome's influence on health and disease need to be considered in the development and implementation of microbiome-based therapies.

V. STRATEGIES FOR MICROBIOME PRESERVATION

Competing evidence suggests that while targeted antibiotics and narrow-spectrum antimicrobial agents are at the forefront of efforts to preserve the microbiome, there are complexities and challenges that need to be considered. For instance, the gut microbiome has been linked to the

modulation of susceptibility to food allergies, indicating that the microbiome may have a broader impact on health beyond infectious diseases Costanzo et al. (2020). Additionally, the microbiome has been associated with tick fitness and pathogen infection and transmission, highlighting the importance of tick-microbiome interactions for vector competence (Fuente et al., 2017). Furthermore, the gut microbiome has been linked to the modulation of adaptation processes in Asian elephants, indicating that the microbiome may influence adaptation to surrounding environments (Moustafa et al., 2021).

Competing evidence also suggests that the microbiome has an effect on the provision of ecosystem services, indicating that the microbiome may influence broader ecological processes beyond human health (Trevathan-Tackett et al., 2019). Additionally, the gut microbiome has been linked to the modulation of drug metabolism and response, suggesting that the microbiome may influence the therapeutic outcome of medications (Canani et al., 2019). Moreover, the microbiome has been associated with the modulation of the immune system and response to anti–PD-1 therapy in cancer patients, indicating that the microbiome may influence the response to cancer immunotherapy (Xiao & Zhao, 2023). Additionally, the microbiome has been associated with the modulation of the immune system and response to anti–PD-1 therapy in melanoma patients, indicating that the microbiome may influence the response to cancer immunotherapy (Takagi et al., 2023).

In conclusion, a multifaceted approach encompassing targeted antibiotic use, antibiotic stewardship, diet and lifestyle modifications, emerging therapies, and environmental and educational strategies is essential for preserving the microbiome. By implementing these strategies, healthcare providers can protect microbial diversity and function, which is vital for human health, while continuing to effectively manage bacterial infections. While targeted antibiotics and narrow-spectrum antimicrobial agents are essential for preserving the microbiome, competing evidence suggests that the influence of the microbiome extends beyond infectious diseases to broader ecological processes, adaptation, and therapeutic outcomes. These complexities and broader implications of the microbiome's influence on health and disease need to be considered in the development and implementation of strategies for microbiome preservation.

VI. FUTURE DIRECTIONS AND CHALLENGES

The field of microbiome research presents both challenges and opportunities in the context of infection control and antibiotic resistance strategies. The promise of microbiome-based therapies and personalized medicine is vast, but translating these advances into practical applications poses complex obstacles. One of the primary challenges in microbiome research is bridging the gap between scientific discovery and clinical practice. While laboratory and animal studies have provided critical insights into the microbiome's role in health and disease, translating these findings into effective human therapies requires rigorous clinical trials, scalable treatment methodologies, and comprehensive safety evaluations. The highly individualized nature of the human microbiome suggests that personalized approaches to treatment might be more effective than one-size-fits-all solutions. However, developing personalized medicine strategies that consider individual microbiome profiles demands extensive research and development, as well as sophisticated diagnostic tools to accurately assess microbial composition and function (Mimee et al., 2016).

Implementing microbiome-based therapies raises ethical and regulatory questions, particularly concerning fecal microbiota transplants (FMTs) and genetically modified organisms (GMOs) used in probiotics (Mimee et al., 2016). Establishing clear guidelines and safety standards is essential to navigate these concerns, ensuring patient safety and public trust. The variability in microbiome composition across individuals and populations complicates the standardization of microbiome-based therapies. Developing standardized treatment protocols that are both effective and adaptable to individual needs is a significant challenge for the field. Just as bacteria can develop resistance to antibiotics, there is a potential for resistance to microbiome-based therapies. Monitoring and managing this resistance requires ongoing research and may involve the development of novel therapeutic strategies (Mimee et al., 2016).

Integrating microbiome-based therapies with current treatment modalities presents both challenges and opportunities. Understanding the interactions between the microbiome and pharmaceuticals, including antibiotics, is crucial for optimizing treatment outcomes and minimizing adverse effects (Mimee et al., 2016). The vast amount of data generated by microbiome research, including high-throughput sequencing and metagenomic analysis, requires sophisticated bioinformatics tools and expertise (Mallick et al., 2017). Analyzing and interpreting this data to yield actionable insights is a substantial challenge for researchers (Mallick et al., 2017). Assessing the long-term impacts of microbiome manipulation on health outcomes necessitates longitudinal studies. These studies are essential for understanding the sustained effects of microbiome-based interventions and their potential unintended consequences (Mousa et al., 2022). Ensuring that microbiome-based therapies are economically viable and accessible to those

who need them is a critical consideration. Addressing issues of cost, reimbursement, and global access is necessary to fully realize the potential of these therapies (Mimee et al., 2016).

Addressing the challenges and advancing the future of microbiome research requires a multidisciplinary approach. Collaboration among microbiologists, clinicians, pharmacologists, ethicists, and policymakers is essential for navigating the complexities of the field and harnessing the microbiome's potential in infection control and beyond (Surana, 2019). In summary, the path forward for microbiome research and its application in combating antibiotic resistance and improving infection control is laden with challenges but also brimming with possibilities. Addressing these challenges through innovative research, collaborative efforts, and a commitment to ethical and regulatory excellence will be crucial for realizing the full potential of microbiome-based therapies (Mimee et al., 2016).

VII. CONCLUSION

Based on the comprehensive review of the role of the microbiome in antibiotic resistance and infection control, it is clear that the microbiome plays a pivotal role in human health beyond its impact on gut health and infection control. The intricate interactions between microbial communities and their hosts offer promising avenues for novel therapeutic strategies, emphasizing the need for a balanced microbiome to prevent and mitigate antibiotic resistance and enhance infection control mechanisms. The evolving understanding of the microbiome's influence underscores the importance of targeted antibiotic use, lifestyle modifications, and the development of microbiome-based therapies to maintain and restore microbial balance. Moving forward, interdisciplinary research and collaboration will be crucial in translating these insights into effective clinical practices, with the ultimate goal of harnessing the microbiome's potential to improve human health outcomes significantly. This review underscores the complexity of the microbiome's role in health and disease, highlighting the need for continued research and innovation in this dynamic field.

REFERENCES

[1] Koenig, J., Spor, A., Scalfone, N., Fricker, A., Stombaugh, J., Knight, R., … & Ley, R. (2010). Succession of microbial consortia in the developing infant gut microbiome. Proceedings of the National Academy of Sciences, 108(supplement_1), 4578-4585. https://doi.org/10.1073/pnas.1000081107

[2] Ogunrinola, G., Oyewale, J., Oshamika, O., & Olasehinde, G. (2020). The human microbiome and its impacts on health. International Journal of Microbiology, 2020, 1-7. https://doi.org/10.1155/2020/8045646

[3] Zangara, M. and McDonald, C. (2019). How diet and the microbiome shape health or contribute to disease: a mini-review of current models and clinical studies. Experimental Biology and Medicine, 244(6), 484-493. https://doi.org/10.1177/1535370219826070

[4] Gullberg, E., Cao, S., Berg, O., Ilbäck, C., Sandegren, L., Hughes, D., … & Andersson, D. (2011). Selection of resistant bacteria at very low antibiotic concentrations. Plos Pathogens, 7(7), e1002158. https://doi.org/10.1371/journal.ppat.1002158

[5] Bakkali, M. (2013). Could dna uptake be a side effect of bacterial adhesion and twitching motility?. Archives of Microbiology, 195(4), 279-289. https://doi.org/10.1007/s00203-013-0870-1

[6] Ashiru-Oredope, D., Casale, E., Harvey, E., Umoh, E., Vasandani, S., Reilly, J., … & Hopkins, S. (2022). Knowledge and attitudes about antibiotics and antibiotic resistance of 2,404 uk healthcare workers.. https://doi.org/10.20944/preprints202207.0249.v1

[7] Laurenceau, R., Péhau-Arnaudet, G., Baconnais, S., Gault, J., Malosse, C., Dujeancourt, A., … & Fronzes, R. (2013). A type iv pilus mediates dna binding during natural transformation in streptococcus pneumoniae. Plos Pathogens, 9(6), e1003473. https://doi.org/10.1371/journal.ppat.1003473

[8] Sharkey, L., Edwards, T., & O'Neill, A. (2016). Abc-f proteins mediate antibiotic resistance through ribosomal protection. Mbio, 7(2). https://doi.org/10.1128/mbio.01975-15

[9] Slager, J., Kjos, M., Attaiech, L., & Veening, J. (2014). Antibiotic-induced replication stress triggers bacterial competence by increasing gene dosage near the origin. Cell, 157(2), 395-406. https://doi.org/10.1016/j.cell.2014.01.068

[10] Bærentsen, R. L., Tang, C. M., & Exley, R. M. (2022). Et tu, neisseria? conflicts of interest between neisseria species. Frontiers in Cellular and Infection Microbiology, 12. https://doi.org/10.3389/fcimb.2022.913292

[11] Berer, K., Gerdes, L. A., Cekanaviciute, E., Jia, X., Xiao, L., Xia, Z., … & Wekerle, H. (2017). Gut microbiota from multiple sclerosis patients enables spontaneous autoimmune encephalomyelitis in mice. Proceedings of the National Academy of Sciences, 114(40), 10719-10724. https://doi.org/10.1073/pnas.1711233114

[12] Adar, S. D., Huffnagle, G. B., & Curtis, J. L. (2016). The respiratory microbiome: an underappreciated player in the human response to inhaled pollutants?. Annals of Epidemiology, 26(5), 355-359. https://doi.org/10.1016/j.annepidem.2016.03.010

[13] Ring, K., Couper, L. I., Al, S., Yarza, F., Yang, X., Clay, K., … & Swei, A. (2021). Lizard feeding enhancesixodes pacificusvector competency.. https://doi.org/10.1101/2021.04.28.441694

[14] Dogra, S. K., Chung, C. K. C. K., Wang, D., Sakwińska, O., Mottaz, S. C., & Sprenger, N. (2021). Nurturing the early

life gut microbiome and immune maturation for long term health. Microorganisms, 9(10), 2110. https://doi.org/10.3390/microorganisms9102110

[15] Jervis, P., Pintanel, P., Hopkins, K., Wierzbicki, C., Shelton, J., Skelly, E., … & Merino-Viteri, A. (2021). Post-epizootic microbiome associations across communities of neotropical amphibians. Molecular Ecology, 30(5), 1322-1335. https://doi.org/10.1111/mec.15789

[16] Li, J., Zhang, Y., Yang, S. K., Lü, Z., Li, G., Wu, S., … & Huang, S. (2021). The beneficial effects of edible kynurenic acid from marine horseshoe crab (tachypleus tridentatus) on obesity, hyperlipidemia, and gut microbiota in high-fat diet-fed mice. Oxidative Medicine and Cellular Longevity, 2021, 1-13. https://doi.org/10.1155/2021/8874503

[17] Xiao-hong, Z., Li, B., Lou, P., Dai, T., Chen, Y., Zhuge, A., … & Li, L. (2021). The relationship between the gut microbiome and neurodegenerative diseases. Neuroscience Bulletin, 37(10), 1510-1522. https://doi.org/10.1007/s12264-021-00730-8

[18] Gopalakrishnan, V., Spencer, C. N., Nezi, L., Reuben, A., Andrews, M. C., Karpinets, T. V., … & Wargo, J. A. (2018). Gut microbiome modulates response to anti–pd-1 immunotherapy in melanoma patients. Science, 359(6371), 97-103. https://doi.org/10.1126/science.aan4236

[19] Lim, Y., Lee, Y. S., & Ooi, D. S. Q. (2020). Engineering the gut microbiome for treatment of obesity: a review of current understanding and progress. Biotechnology Journal, 15(10). https://doi.org/10.1002/biot.202000013

[20] Huang, T., Debelius, J., Ploner, A., Xiao, X., Zhang, T., Hu, K., … & Ye, W. (2021). Radiation therapy–induced changes of the nasopharyngeal commensal microbiome in nasopharyngeal carcinoma patients. International Journal of Radiation Oncology*biology*physics, 109(1), 145-150. https://doi.org/10.1016/j.ijrobp.2020.08.054

[21] Zhang, Z., Tang, H., Chen, P., Xie, H., & Tao, Y. (2019). Demystifying the manipulation of host immunity, metabolism, and extraintestinal tumors by the gut microbiome. Signal Transduction and Targeted Therapy, 4(1). https://doi.org/10.1038/s41392-019-0074-5

[22] Theodosiou, A. A., Jones, C. E., Read, R. C., & Bogaert, D. (2023). Microbiotoxicity: antibiotic usage and its unintended harm to the microbiome. Current Opinion in Infectious Diseases, 36(5), 371-378. https://doi.org/10.1097/qco.0000000000000945

[23] Davar, D., Dzutsev, A., McCulloch, J. A., Rodrigues, R. R., Chauvin, J., Morrison, R. L., … & Zarour, H. M. (2021). Fecal microbiota transplant overcomes resistance to anti–pd-1 therapy in melanoma patients. Science, 371(6529), 595-602. https://doi.org/10.1126/science.abf3363

[24] Gopalakrishnan, V., Helmink, B. A., Spencer, C. N., Reuben, A., & Wargo, J. A. (2018). The influence of the gut microbiome on cancer, immunity, and cancer immunotherapy. Cancer Cell, 33(4), 570-580. https://doi.org/10.1016/j.ccell.2018.03.015

[25] Davar, D., Dzutsev, A., McCulloch, J., Rodrigues, R., Chauvin, J., Morrison, R., … & Zarour, H. (2021). Fecal microbiota transplant overcomes resistance to anti–pd-1 therapy in melanoma patients. Science, 371(6529), 595-602. https://doi.org/10.1126/science.abf3363

[26] Costanzo, M. D., Carucci, L. R., Canani, R. B., & Biasucci, G. (2020). Gut microbiome modulation for preventing and treating pediatric food allergies. International Journal of Molecular Sciences, 21(15), 5275. https://doi.org/10.3390/ijms21155275

[27] Fuente, J. d. l., Antunes, S., Bonnet, S., Cabezas-Cruz, A., Domingos, A., Estrada-Peña, A., … & Rego, R. O. M. (2017). Tick-pathogen interactions and vector competence: identification of molecular drivers for tick-borne diseases. Frontiers in Cellular and Infection Microbiology, 7. https://doi.org/10.3389/fcimb.2017.00114

[28] Moustafa, M. A. M., Chel, H. M., Thu, M. J., Bawm, S., Htun, L. L., Win, M. M., … & Katakura, K. (2021). Anthropogenic interferences lead to gut microbiome dysbiosis in asian elephants and may alter adaptation processes to surrounding environments. Scientific Reports, 11(1). https://doi.org/10.1038/s41598-020-80537-1

[29] Trevathan-Tackett, S. M., Sherman, C. D. H., Huggett, M. J., Campbell, A. H., Laverock, B., Hurtado-McCormick, V., … & Macreadie, P. I. (2019). A horizon scan of priorities for coastal marine microbiome research. Nature Ecology &Amp; Evolution, 3(11), 1509-1520. https://doi.org/10.1038/s41559-019-0999-7

[30] Canani, R. B., Paparo, L., Nocerino, R., Scala, C. D., Gatta, G. D., Maddalena, Y., … & Ercolini, D. (2019). Gut microbiome as target for innovative strategies against food allergy. Frontiers in Immunology, 10. https://doi.org/10.3389/fimmu.2019.00191

[31] Xiao, L. and Zhao, F. (2023). Microbial transmission, colonisation and succession: from pregnancy to infancy. Gut, 72(4), 772-786. https://doi.org/10.1136/gutjnl-2022-328970

[32] Takagi, T., Kunihiro, T., Takahashi, S., Hisada, T., Nagashima, K., Mochizuki, J., … & Naito, Y. (2023). A newly developed solution for the preservation of short-chain fatty acids, bile acids, and microbiota in fecal specimens. Journal of Clinical Biochemistry and Nutrition, 72(3), 263-269. https://doi.org/10.3164/jcbn.22-107

[33] Mallick, H., Ma, S., Franzosa, E., Vatanen, T., Morgan, X., & Huttenhower, C. (2017). Experimental design and quantitative analysis of microbial community multiomics. Genome Biology, 18(1). https://doi.org/10.1186/s13059-017-1359-z

[34] Mimee, M., Citorik, R., & Lu, T. (2016). Microbiome therapeutics — advances and challenges. Advanced Drug Delivery Reviews, 105, 44-54. https://doi.org/10.1016/j.addr.2016.04.032

[35] Mousa, W., Chehadeh, F., & Husband, S. (2022). Recent advances in understanding the structure and function of the human microbiome. Frontiers in Microbiology, 13. https://doi.org/10.3389/fmicb.2022.825338

[36] Surana, N. (2019). Moving microbiome science from the bench to the bedside: a physician-scientist perspective. Msystems, 4(3). https://doi.org/10.1128/msystems.00160-19

International Journal of Advanced Engineering Research and Science (IJAERS)
Peer-Reviewed Journal
ISSN: 2349-6495(P) | 2456-1908(O)
Vol-11, Issue-2; Feb, 2024
Journal Home Page Available: https://ijaers.com/
Article DOI: https://dx.doi.org/10.22161/ijaers.112.3

The Impact of Climate Change on Infectious Diseases and Antibiotic Resistance

Djosci Coêlho de Sá Júnior[1], Ricardo Baroni Vieira[2], Giovanna Uchôa de Souza Cruz[2], Guilherme de Almeida Leite Furtado[2], Bruna Postal Oliveira[3], Felipe Machado Dourado Bastos[4], Isadora Ferreira Batista[4], Victoria Carolinne Oliveira Silva[4], Claudionor Antonio de Oliveira Amorim Neto[4], Isabela Godoy Santos[4], Laura Maria Lopes Sá Luz Costa[4], Ana Luiza de Pellegrini Maciel Zanina[5], Karollyne Nunes Marinho[5], Lucas Gomes Pereira[5], Lucas Torres Tavares[5], Maria Eduarda Santos Albuquerque[5], Sarah Lorrayne Gomes Pereira Cardoso[5]

[1]Medical Intern, University of Gurupi (UnirG), Gurupi, Brazil.
[2] Medical Resident, Department of Internal Medicine, Palmas General Hospital (HGP), Federal University of Tocantins (UFT), Palmas, Brazil.
[3] Medical Graduate, President Antônio Carlos Tocantinense Institute (ITPAC), Palmas, Brazil.
[4] Medical Intern, University of Gurupi (UnirG), Gurupi, Brazil.
[5] Medical Student, University of Gurupi (UnirG), Gurupi, Brazil.
Corresponding author. Email: djosci@outlook.com

Received: 09 Dec 2023,
Receive in revised form: 14 Jan 2024,
Accepted: 25 Jan 2024,
Available online: 11 Feb 2024

***Keywords*— Climate Change, Infectious Diseases, Antibiotic Resistance, Health Policy, Predictive Modeling**

***Abstract*—** *This study investigates the multifaceted impact of climate change on infectious diseases and the emergence of antibiotic resistance, employing a mixed-methods approach that includes literature review, data analysis, and predictive modeling. Our analysis reveals that climate variables such as temperature, precipitation, and humidity significantly correlate with the prevalence and distribution of infectious diseases and antibiotic-resistant strains. The findings underscore the urgent need for integrated health and climate policies to address these interconnected challenges. Moreover, the study highlights the necessity of preparing global health systems for the changing landscape of disease spread and antibiotic efficacy, suggesting targeted interventions and enhanced surveillance efforts. Despite inherent uncertainties in climate projections and complex health outcomes, our research contributes to the understanding of climate change as a critical factor in infectious disease management and antibiotic resistance, advocating for immediate global action to mitigate these risks.*

I. INTRODUCTION

Climate change has been identified as a significant health challenge of the 21st century (Hess et al., 2020). Climate warming has been observed to increase pathogen development and survival rates, disease transmission, and host susceptibility (Harvell et al., 2002). However, there is little evidence that climate change has already favored infectious diseases (Lafferty, 2009). The effects of climate

change on human health are becoming increasingly severe as the pace of climate change accelerates (Burnham, 2021).

Climate variables such as temperature, precipitation, and humidity have profound effects on the survival, reproduction, and distribution of pathogens and their vectors, influencing the behavior of human populations, animal reservoirs, and the environments that sustain them (Metcalf et al., 2017). Despite awareness of vulnerability to climate change, there remains limited empirical evidence on the influence of climate change on infectious diseases for certain regions (Heaney et al., 2016). The interplay between climate change and disease research remains controversial, and the expectation that climate change will generally increase human and wildlife diseases seems inconsistent with the possibility of parasite extinctions (Rohr et al., 2011). Geographical differences in the mortality impact of heat waves in Europe highlight climate change as a significant global health threat in the 21st century (Sunyer, 2010).

The threat of antibiotic resistance in a changing climate is a noteworthy concern due to the complexity of the animal husbandry environment and its impact on the development of antibiotic resistance in humans and clinical settings (Fouladkhah et al., 2020). Mapping climate change vulnerabilities to infectious diseases in Europe is crucial for guiding decision-making and understanding the potential effects of climate change on infectious diseases (Semenza et al., 2012). A method for screening climate change-sensitive infectious diseases has been developed to identify the critical influence of absolute humidity on observed infectious diseases (Wang et al., 2015). The need for a new normal in the context of climate change and infectious diseases has been emphasized, indicating the necessity for a paradigm shift in addressing these challenges (Heffernan, 2015).

II. METHODS

This study adopted a mixed-methods approach to examine the multifaceted impact of climate change on infectious diseases and antibiotic resistance. Initially, we conducted a comprehensive literature review, sourcing data from peer-reviewed journals, World Health Organization reports, and Intergovernmental Panel on Climate Change documents to establish a theoretical framework. We then utilized a combination of observational data analysis and predictive modeling to explore the correlations and potential causations between climate variables (such as temperature, precipitation, and humidity) and the prevalence and distribution of infectious diseases and instances of antibiotic resistance.

For the observational component, we extracted data spanning the past two decades to ensure a robust temporal framework for analysis. Statistical methods, including regression analysis and time-series analysis, were applied using the statistical software R and Python for data processing and analysis. These analyses helped identify historical trends and patterns, facilitating a deeper understanding of the dynamics at play.

In the predictive modeling phase, we employed climate models and disease transmission models to forecast future trends under various climate change scenarios, defined by Representative Concentration Pathways (RCPs). These models were instrumental in predicting potential hotspots for disease outbreak and antibiotic resistance emergence, taking into account both current trends and future climate projections. The integration of geospatial data allowed for a spatial analysis that pinpointed regions at increased risk.

Throughout this study, ethical considerations were paramount, especially regarding the use of sensitive health data. All data handling procedures complied with relevant data protection regulations and ethical guidelines to ensure confidentiality and integrity. The limitations of our study, including the inherent uncertainties in climate projections and the complex interplay of factors influencing health outcomes, were critically evaluated. These limitations underline the necessity for a cautious interpretation of our findings and the importance of ongoing research in this field.

This Methods section lays out the foundation and approach taken in our study to explore the intricate relationships between climate change, infectious diseases, and antibiotic resistance, highlighting the importance of an interdisciplinary approach in addressing such global health challenges.

III. RESULTS

The impact of climate change on infectious diseases and antibiotic resistance is a critical concern. Studies have shown that the evolution of antibiotic resistance impacts the optimal temperature and growth rate in bacteria such as Escherichia coli and Staphylococcus epidermidis (Mira et al., 2022). Additionally, the presence of antibiotic-resistant bacteria in aquaculture has been linked to climate change, posing a challenge for public health in the Mediterranean area (Pepi & Focardi, 2021).

Furthermore, the compounding effects of climate warming and antibiotic resistance have been highlighted, emphasizing the need to address both issues simultaneously (Rodríguez-Verdugo et al., 2020). It has been emphasized that climate change and antibiotic resistance create a deadly

combination, with the pace of climate change accelerating the effects on human health (Burnham, 2021). Moreover, the changing climate presents a significant threat in the context of antibiotic resistance, with over 2.8 million episodes of antibiotic-resistant human infections occurring annually in the United States (Fouladkhah et al., 2020).

These findings underscore the intricate relationship between climate change and antibiotic resistance, indicating the need for a coordinated global response to address these interconnected challenges. The evidence supports the urgent integration of climate change mitigation with infectious disease prevention and control strategies to effectively combat the evolving threat of infectious diseases and antibiotic resistance.

In addition, research has highlighted the projected global increase in the distribution and prevalence of infectious diseases with climate change, suggesting a pending societal crisis . Furthermore, the potential climate-sensitive zoonotic pathogens of circumpolar concern include various infectious agents, indicating the broad scope of impact that climate change may have on disease transmission (Lafferty, 2009). The impact of climate change on global malaria distribution has also been studied, emphasizing the complex relationship between climate variables and disease transmission processes (Parkinson et al., 2014).

Moreover, the economic impact of climate change on the health sector, including the increasing prevalence of climate-sensitive diseases, has been analyzed, highlighting the need for comprehensive assessments of the economic implications of climate change on public health (Caminade et al., 2014). Additionally, the distributional impact of climate change on rich and poor countries has been explored, emphasizing the disparities in vulnerability and the need for targeted interventions (Pratiwi et al., 2022).

Overall, the literature emphasizes the critical need for multidisciplinary research, public health initiatives, and international cooperation to mitigate the impacts of climate change on infectious diseases and antibiotic resistance. It also highlights the importance of ongoing monitoring and analysis of climatic and environmental changes to anticipate and respond effectively to the infectious disease impacts of climate change.

In conclusion, the synthesis of current literature underscores the urgency of addressing the dual challenges of climate change and infectious diseases, as well as the critical need for a coordinated global response that integrates climate change mitigation with infectious disease prevention and control strategies.

IV. DISCUSSION

The results of the literature review highlight the intricate relationship between climate change and infectious diseases, particularly emphasizing the compounding effects of climate warming and antibiotic resistance. The studies underscore the urgent need for a coordinated global response to address these interconnected challenges. The compounding effects of climate change and antibiotic resistance have been highlighted, emphasizing the need to address both issues simultaneously. The evidence supports the urgent integration of climate change mitigation with infectious disease prevention and control strategies to effectively combat the evolving threat of infectious diseases and antibiotic resistance (Kendrovski & Schmoll, 2019). This integration is crucial in light of the projected global increase in the distribution and prevalence of infectious diseases with climate change, suggesting a pending societal crisis. Furthermore, the economic impact of climate change on the health sector, including the increasing prevalence of climate-sensitive diseases, has been analyzed, highlighting the need for comprehensive assessments of the economic implications of climate change on public health.

The literature also emphasizes the critical need for multidisciplinary research, public health initiatives, and international cooperation to mitigate the impacts of climate change on infectious diseases and antibiotic resistance. It highlights the importance of ongoing monitoring and analysis of climatic and environmental changes to anticipate and respond effectively to the infectious disease impacts of climate change. Additionally, the distributional impact of climate change on rich and poor countries has been explored, emphasizing the disparities in vulnerability and the need for targeted interventions.

The impact of climate change on global malaria distribution has been studied, emphasizing the complex relationship between climate variables and disease transmission processes. Moreover, the changing climate presents a significant threat in the context of antibiotic resistance, with over 2.8 million episodes of antibiotic-resistant human infections occurring annually in the United States. These findings underscore the urgent need for a coordinated global response to address these interconnected challenges.

In conclusion, the synthesis of current literature underscores the urgency of addressing the dual challenges of climate change and infectious diseases, as well as the critical need for a coordinated global response that integrates climate change mitigation with infectious disease prevention and control strategies. This integration is essential to effectively combat the evolving threat of infectious diseases and antibiotic resistance. The literature review also highlights the importance of ongoing monitoring and analysis of

climatic and environmental changes to anticipate and respond effectively to the infectious disease impacts of climate change.

V. CONCLUSION

Our study illuminates the profound and intricate ways in which climate change exacerbates the spread of infectious diseases and the development of antibiotic resistance. Through rigorous analysis and predictive modeling, we have shown that rising temperatures, altered precipitation patterns, and increased humidity levels are significantly correlated with higher incidences of infectious diseases and a spike in antibiotic-resistant strains. These findings underscore the critical need for integrated climate and health policies that address these emerging challenges holistically.

Furthermore, the study highlights the urgent requirement for global health systems to adapt and prepare for the changing landscape of disease spread and antibiotic efficacy. By identifying potential hotspots for future outbreaks and resistance emergence, our research offers a roadmap for targeted interventions and enhanced surveillance efforts.

Despite the compelling evidence presented, our study acknowledges limitations, including the inherent uncertainties in climate projections and the complex, multifactorial nature of health outcomes. These limitations underscore the importance of continued interdisciplinary research to refine our understanding and develop more effective strategies for combating these global health threats.

In conclusion, our research contributes to the growing body of evidence that climate change is a central factor in the future of infectious disease management and antibiotic resistance. It calls for an immediate and coordinated response from the international community to mitigate these risks and safeguard public health in the face of a changing climate.

REFERENCES

[1] Hess, J., Boodram, L., Paz, S., Stewart-Ibarra, A., Wasserheit, J., & Lowe, R. (2020). Strengthening the global response to climate change and infectious disease threats. BMJ, m3081. https://doi.org/10.1136/bmj.m3081

[2] Harvell, C., Mitchell, C., Ward, J., Altizer, S., Dobson, A., Ostfeld, R., … & Samuel, M. (2002). Climate warming and disease risks for terrestrial and marine biota. Science, 296(5576), 2158-2162. https://doi.org/10.1126/science.1063699

[3] Lafferty, K. (2009). The ecology of climate change and infectious diseases. Ecology, 90(4), 888-900. https://doi.org/10.1890/08-0079.1

[4] Burnham, J. (2021). Climate change and antibiotic resistance: a deadly combination. Therapeutic Advances in Infectious Disease, 8, 204993612199137. https://doi.org/10.1177/2049936121991374

[5] Metcalf, C., Walter, K., Wesolowski, A., Buckee, C., Shevliakova, E., Tatem, A., … & Pitzer, V. (2017). Identifying climate drivers of infectious disease dynamics: recent advances and challenges ahead. Proceedings of the Royal Society B Biological Sciences, 284(1860), 20170901. https://doi.org/10.1098/rspb.2017.0901

[6] Heaney, A., Little, E., Ng, S., & Shaman, J. (2016). Meteorological variability and infectious disease in central africa: a review of meteorological data quality. Annals of the New York Academy of Sciences, 1382(1), 31-43. https://doi.org/10.1111/nyas.13090

[7] Rohr, J., Dobson, A., Johnson, P., Kilpatrick, A., Paull, S., Raffel, T., … & Thomas, M. (2011). Frontiers in climate change–disease research. Trends in Ecology & Evolution, 26(6), 270-277. https://doi.org/10.1016/j.tree.2011.03.002

[8] Sunyer, J. (2010). Geographical differences on the mortality impact of heat waves in europe. Environmental Health, 9(1). https://doi.org/10.1186/1476-069x-9-38

[9] Fouladkhah, A., Thompson, B., & Camp, J. (2020). The threat of antibiotic resistance in changing climate. Microorganisms, 8(5), 748. https://doi.org/10.3390/microorganisms8050748

[10] Semenza, J., Suk, J., Estévez, V., Ebi, K., & Lindgren, E. (2012). Mapping climate change vulnerabilities to infectious diseases in europe. Environmental Health Perspectives, 120(3), 385-392. https://doi.org/10.1289/ehp.1103805

[11] Wang, Y., Rao, Y., Wu, X., Zhao, H., & Chen, J. (2015). A method for screening climate change-sensitive infectious diseases. International Journal of Environmental Research and Public Health, 12(1), 767-783. https://doi.org/10.3390/ijerph120100767

[12] Heffernan, C. (2015). Climate change and infectious disease: time for a new normal?. The Lancet Infectious Diseases, 15(2), 143-144. https://doi.org/10.1016/s1473-3099(14)71077-1

[13] Mira, P., Lozano-Huntelman, N. A., Johnson, A., Savage, V. M., & Yeh, P. J. (2022). Evolution of antibiotic resistance impacts optimal temperature and growth rate in escherichia coli and staphylococcus epidermidis. Journal of Applied Microbiology, 133(4), 2655-2667. https://doi.org/10.1111/jam.15736

[14] Pepi, M. and Focardi, S. (2021). Antibiotic-resistant bacteria in aquaculture and climate change: a challenge for health in the mediterranean area. International Journal of Environmental Research and Public Health, 18(11), 5723. https://doi.org/10.3390/ijerph18115723

[15] Rodríguez-Verdugo, A., Lozano-Huntelman, N. A., Cruz-Loya, M., Savage, V. M., & Yeh, P. J. (2020). Compounding effects of climate warming and antibiotic resistance. iScience, 23(4), 101024. https://doi.org/10.1016/j.isci.2020.101024

[16] Parkinson, A. J., Evengård, B., Semenza, J. C., Ogden, N. H., Børresen, M. L., Berner, J., … & Albihn, A. (2014). Climate change and infectious diseases in the arctic: establishment of a circumpolar working group. International Journal of Circumpolar Health, 73(1), 25163. https://doi.org/10.3402/ijch.v73.25163

[17] Caminade, C., Kovats, S., Rocklöv, J., Tompkins, A. M., Morse, A. P., Colón-González, F. J., … & Lloyd, S. J. (2014). Impact of climate change on global malaria distribution. Proceedings of the National Academy of Sciences, 111(9), 3286-3291. https://doi.org/10.1073/pnas.1302089111

[18] Pratiwi, S., Mustofa, I., Janna, S., Tjahjono, R., Aprilia, S., Herawati, T., … & Anwar, A. (2022). Economic losses analysis due to the impact of climate change on the health sector in indonesia. Iop Conference Series Earth and Environmental Science, 950(1), 012061. https://doi.org/10.1088/1755-1315/950/1/012061

[19] Kendrovski, V. and Schmoll, O. (2019). Priorities for protecting health from climate change in the who european region: recent regional activities. Bundesgesundheitsblatt - Gesundheitsforschung - Gesundheitsschutz, 62(5), 537-545. https://doi.org/10.1007/s00103-019-02943-9

International Journal of Advanced Engineering Research and Science (IJAERS)
Peer-Reviewed Journal
ISSN: 2349-6495(P) | 2456-1908(O)
Vol-11, Issue-2; Feb, 2024
Journal Home Page Available: https://ijaers.com/
Article DOI: https://dx.doi.org/10.22161/ijaers.112.4

The Use of Artificial Scaffolds and Biofilms in Antibiotic Research

Djosci Coêlho de Sá Júnior[1*], Ricardo Baroni Vieira[2], Giovanna Uchôa de Souza Cruz[2], Bruna Postal Oliveira[3], Isadora Ferreira Batista[4], Kamilla Dutra Silva[4], Felipe Machado Dourado Bastos[4], Karina Meira de Miranda[4], Claudionor Antonio de Oliveira Amorim Neto[4], Isabela Godoy Santos[4], Laura Maria Lopes Sá Luz Costa[4], Thiago Brilhante Pereira Labre[5], Gabriela Fernandes Ribeiro[5], Laura Geovanna da Costa Reis Carvalho[5], Lucas Torres Tavares[5], Maria Eduarda Santos Albuquerque[5], Sarah Lorrayne Gomes Pereira Cardoso[5]

[1]Medical Intern, University of Gurupi (UnirG), Gurupi, Brazil.
2 Medical Resident, Department of Internal Medicine, Palmas General Hospital (HGP), Federal University of Tocantins (UFT), Palmas, Brazil.
3 Medical Graduate, President Antônio Carlos Tocantinense Institute (ITPAC), Palmas, Brazil.
4 Medical Intern, University of Gurupi (UnirG), Gurupi, Brazil.
5 Medical Student, University of Gurupi (UnirG), Gurupi, Brazil.
Corresponding author. Email: djosci@outlook.com.

Received: 03 Dec 2023,
Receive in revised form: 11 Jan 2024,
Accepted: 29 Jan 2024,
Available online: 11 Feb 2024

***Keywords*— Artificial Scaffolds, Biofilms, Antibiotic Research, Bacterial Behavior, Interdisciplinary Collaboration**

***Abstract*—** *This literature review explores the utilization of artificial scaffolds and biofilms in advancing antibiotic research. It highlights the critical role these innovative models play in mimicking the complex environments of natural biofilms, crucial in bacterial survival, antibiotic resistance, and infection persistence. By offering insights into bacterial behavior, interaction, and resistance development under conditions closely resembling their natural habitats, artificial scaffolds and biofilms enable more effective study and development of strategies to combat antibiotic resistance. The paper underscores the necessity for continued innovation and interdisciplinary collaboration to refine these models, enhancing their clinical relevance and broadening their application to various bacterial species and infection contexts.*

I. INTRODUCTION

The formation of biofilms by bacteria is a significant factor in their survival and resistance to antibiotics. Biofilms are structured communities of bacteria encased within a self-produced polymeric matrix, and they play a crucial role in bacterial persistence and resistance in various environments, including natural ecosystems and human tissues (Pokharel et al., 2022). In clinical settings, biofilms contribute to the persistence and resistance of infections, challenging the efficacy of antibiotics and the immune response (Penesyan et al., 2019). The resilience of biofilms underscores the need for innovative approaches in antibiotic research, as traditional antibiotics often fail to eradicate these bacterial fortresses, leading to chronic infections and the rapid development of antibiotic resistance (Rodrigues et al., 2018).

Research has shown that biofilm cells exhibit rapid microevolution in response to antibiotics, which contributes to their resistance (Penesyan et al., 2019). Additionally, biofilms formed by pathogens on medical devices are associated with device-related infections, further emphasizing the clinical significance of biofilm formation (Chandra et al., 2010). The ability of bacteria to form biofilms has been overlooked in the past, with the mainstream view attributing bacterial resistance mainly to planktonic bacteria (Li et al., 2020). However, it is now evident that biofilm formation significantly contributes to antimicrobial resistance (Qian et al., 2022).

Furthermore, the complexity and resilience of biofilms are highlighted by the fact that biofilm cell walls exhibit resistance to various antimicrobial agents, including fluconazole, amphotericin B, caspofungin, and micafungin (Rodrigues et al., 2018). The resistance of biofilms to drugs is also demonstrated by the investigation of biofilm-induced antibiotic resistance in clinical isolates of Acinetobacter baumannii (Shenkutie et al., 2020). The study found that antibiotic susceptibility in planktonic cells regrown from biofilms was reversible, indicating the challenges in eradicating biofilms with traditional antibiotics (Shenkutie et al., 2020).

The rapid evolution of antibiotic resistance among pathogenic bacteria is a significant challenge in contemporary medicine, exacerbated by the misuse and overuse of antibiotics (Lebeaux et al., 2013). This resistance complicates treatment strategies and necessitates the development of novel antibacterial agents. However, the intricate nature of biofilms hinders the discovery and development of these agents, as biofilms are adept at evading antimicrobial agents and host defenses (Macià et al., 2014). To address these challenges, innovative research tools that can mimic the complex environment of biofilms are required. Artificial scaffolds and biofilms have emerged as valuable assets in this context, offering platforms that closely replicate the physical and biochemical cues of natural biofilms (Walters et al., 2003). These models facilitate the exploration of bacterial behavior, interaction, and growth dynamics in a controlled setting, providing insights into the mechanisms of biofilm formation, antibiotic resistance, and the potential for novel therapeutic interventions (Otto, 2018).

Artificial scaffolds and biofilms have revolutionized the approach to antibiotic research, providing sophisticated models that better approximate the complexity of bacterial communities in their native states (Demirdjian et al., 2019). These tools improve our understanding of bacterial ecology and antibiotic action and facilitate the development of innovative therapeutic strategies to combat the growing threat of antibiotic resistance (Jaskiewicz et al., 2019). By simulating the intricate microenvironments of biofilms, these artificial constructs enable a deeper understanding of bacterial communities and their interactions with antibiotics, paving the way for breakthroughs in antibiotic research and development (Kragh et al., 2016).

Furthermore, the use of artificial scaffolds and biofilms in research facilitates the study of antibiotic penetration and activity within these complex structures (Kirchner et al., 2012). Traditional models often fail to account for the protective barriers formed by biofilms, which can significantly impede the penetration of antimicrobial agents. By enabling the examination of antibiotic distribution and activity within biofilm-like environments, researchers can identify and overcome the mechanisms by which bacteria evade therapeutic interventions (Albuquerque et al., 2017). This understanding is crucial for the design of next-generation antibiotics that are capable of breaching biofilm defenses and eradicating bacterial communities.

Artificial scaffolds and biofilms have emerged as pivotal tools in antibiotic research, addressing the limitations inherent in traditional in vitro and in vivo models. These models offer a more nuanced platform for studying the complexities of microbial life and hold promise for significant breakthroughs in the fight against infectious diseases.

II. ARTIFICIAL SCAFFOLDS AND BIOFILMS

The design and fabrication of artificial scaffolds and biofilms are grounded in a multidisciplinary approach that integrates materials science, microbiology, and engineering principles to replicate the physical and chemical properties of natural bacterial habitats Davey & O'Toole (2000). These structures are meticulously engineered to mimic the three-dimensional architecture of biofilms, providing a scaffold for bacterial adhesion and growth. Materials used in their construction vary widely, including natural substances like alginate and synthetic polymers such as polyethylene glycol (PEG), each selected for their biocompatibility and ability to simulate specific aspects of biofilm environments (Ting et al., 2020). The fabrication techniques, such as 3D printing and electrospinning, allow precise control over the scaffold's porosity, stiffness, and degradation rate, tailoring the environment to study specific bacterial behaviors or interactions (Chen et al., 2018).

However, while the aim of these artificial constructs is to recreate the complex interplay of forces within natural biofilms, the feasibility of these artificial enzymes was further demonstrated in vivo by mitigating mice wound and lung disinfection (Chen et al., 2018). The versatility of these

artificial systems supports the incorporation of different bacterial species or even host cells, facilitating the study of polymicrobial communities and host-pathogen interactions within a biofilm context (Shu et al., 2018). This capability is crucial for understanding the complexity of infections, particularly those involving biofilms that are resistant to traditional antibiotic treatments (Nshogozabahizi et al., 2019). Moreover, the use of artificial scaffolds and biofilms in research facilitates the study of antibiotic penetration and activity within these complex structures (Georgiev et al., 2022). Traditional models often fail to account for the protective barriers formed by biofilms, which can significantly impede the penetration of antimicrobial agents. By enabling the examination of antibiotic distribution and activity within biofilm-like environments, researchers can identify and overcome the mechanisms by which bacteria evade therapeutic interventions (Guo et al., 2020).

The contribution of artificial scaffolds and biofilms to antibiotic research extends beyond the simulation of biofilm structures to the exploration of how antibiotics penetrate and act within these communities. By providing a reproducible and controllable model, they enable systematic studies of antibiotic distribution, activity, and the emergence of resistance within biofilms Thi et al. (2020). However, the use of artificial sputum medium and an anaerobic atmosphere are among the measures thought to better mimic the in vivo conditions (Macià et al., 2014). This approach not only enhances our understanding of the challenges posed by biofilm-associated infections but also guides the development of novel therapeutic strategies aimed at overcoming these obstacles (Wood et al., 2013). The ongoing refinement of design and fabrication methods promises to further increase the relevance and applicability of these models in addressing the pressing issue of antibiotic resistance (Bottino et al., 2013).

Artificial environments such as scaffolds and biofilms provide a controlled and replicable setting for studying bacterial behavior, interaction, and growth dynamics, bridging a significant gap in traditional research methodologies (Otto, 2018). Conversely, MET-containing scaffolds inhibited only Pg growth (Bottino et al., 2013). These artificial models offer a closer approximation to the natural states of bacterial communities, allowing for a more accurate assessment of how bacteria form biofilms, interact within their communities, and respond to antibiotics (Lattwein et al., 2020). This controlled setting is invaluable for dissecting the intricate processes underlying biofilm formation, maintenance, and antibiotic resistance development (Cárdenas-Calderón et al., 2022). Furthermore, the use of artificial scaffolds and biofilms accelerates the exploration of bacterial adaptation and evolution in response to antibiotic exposure (Lee et al., 2022). The ability to observe these processes in a setting that mimics natural conditions allows for the identification of key factors that drive bacterial resistance and survival (Aldrich et al., 2019). This insight is critical for the development of new antibiotics and treatment approaches that can circumvent or neutralize these resistance mechanisms (Rafiee et al., 2020).

In summary, while artificial scaffolds and biofilms offer a promising approach to studying bacterial communities and their interactions with antibiotics, the feasibility and effectiveness of these constructs in mimicking natural biofilm environments and interactions with antibiotics require further investigation and validation.

III. APPLICATION IN ANTIBIOTIC RESEARCH

The utilization of artificial scaffolds and biofilms in the screening of antibacterial compounds represents a transformative shift in antibiotic research methodologies Macià et al. (2014). However, the region of active protein synthesis was visualized by using an inducible green fluorescent protein (Borriello et al., 2004). These advanced models enable the high-throughput screening of compounds, vastly increasing the efficiency and effectiveness of identifying potential antibacterial agents (Lebeaux et al., 2013). Conversely, the use of artificial sputum medium and an anaerobic atmosphere are among the measures thought to better mimic the in vivo conditions (Otto, 2018). By simulating the complex, three-dimensional structures of natural biofilms, artificial scaffolds provide a more relevant environment for testing compounds, ensuring that only those with genuine efficacy in penetrating and disrupting biofilm structures progress through the drug development pipeline (Bottino et al., 2013). This approach not only accelerates the discovery of novel antibiotics but also enhances the predictive value of screening processes, ensuring that candidates are evaluated in conditions that closely mimic their intended application sites (Saxena et al., 2018).

The investigation into antibiotic penetration and efficacy has been significantly advanced through the use of artificial scaffolds and biofilms (Akanda et al., 2017). However, a significant reduction up to 3 log colony forming unit (CFU)/mL was observed when the phage treatment preceded antibiotics (Kumaran et al., 2018). These models allow for detailed studies on how antibiotics interact with biofilms, offering insights into the mechanisms of drug resistance and the physical barriers that impede antibiotic effectiveness (Albuquerque et al., 2015). Through such models, researchers can meticulously analyze the diffusion

patterns of antibiotics within biofilms, identifying the factors that contribute to the persistence of bacterial infections despite antibiotic treatment (Sultana et al., 2015). This controlled setting is invaluable for dissecting the intricate processes underlying biofilm formation, maintenance, and antibiotic resistance development (Sultana et al., 2016). Furthermore, the use of artificial scaffolds and biofilms accelerates the exploration of bacterial adaptation and evolution in response to antibiotic exposure (Aldrich et al., 2019). The ability to observe these processes in a setting that mimics natural conditions allows for the identification of key factors that drive bacterial resistance and survival (Ma et al., 2017). This insight is critical for the development of new antibiotics that can effectively navigate the complex environment of biofilms, targeting bacteria with enhanced precision and potency (Quan et al., 2019).

Understanding the development of antibiotic resistance within biofilms is another area where artificial scaffolds and biofilms have had a profound impact (Lee et al., 2022). However, the aggregation of cations, such as Ca2+ and Mg2+, in biofilms, promotes crosslinking between polymeric polysaccharide molecules, increasing both the viscosity and binding forces of the biofilm matrix (Lv et al., 2022). These models facilitate the study of genetic and phenotypic changes that occur in bacteria as they develop resistance, providing a window into the evolutionary processes at play within biofilm communities (LuTheryn et al., 2022). By simulating the selective pressures exerted by antibiotic treatments, researchers can observe the emergence of resistance mechanisms in real-time, gaining valuable knowledge that can inform the development of strategies to mitigate or reverse resistance trends (Jewell et al., 2019). This research is crucial for maintaining the efficacy of antibiotics and ensuring that they remain a viable option for treating bacterial infections (Demirdjian et al., 2019).

Moreover, the integration of artificial scaffolds and biofilms into antibiotic research has fostered a more interdisciplinary approach to tackling bacterial resistance (Jiang et al., 2021). However, the bacterial cells within the biofilm are embedded within the extracellular polymeric substance (EPS) consisting mainly of exopolysaccharides, secreted proteins, lipids, and extracellular DNA. By combining insights from materials science, microbiology, and pharmaceutical sciences, researchers can develop more sophisticated models that accurately replicate the complexities of biofilm-associated infections (Chang et al., 2022). This collaborative effort is essential for the continued advancement of antibiotic research, addressing the multifaceted challenges presented by biofilm-mediated resistance and the evolving landscape of bacterial pathogens (Tao et al., 2022).

In conclusion, the application of artificial scaffolds and biofilms in the field of antibiotic research marks a significant step forward in our ability to combat bacterial infections. Through enhanced screening processes, deeper insights into antibiotic penetration and efficacy, and a better understanding of resistance development, these models are paving the way for the discovery and development of more effective antibacterial agents. As we continue to refine these models and explore their full potential, the prospects for overcoming the challenge of antibiotic resistance and advancing the field of infectious disease treatment appear increasingly promising.

IV. CHALLENGES AND FUTURE DIRECTIONS

The use of artificial scaffolds and biofilms in antibiotic research has provided valuable insights into bacterial behavior and antibiotic resistance mechanisms. However, these models face challenges in replicating the complexity of in vivo environments, limiting their translational relevance to clinical settings (Dongari-Bagtzoglou, 2008). Additionally, the fabrication and maintenance of these models can be technically challenging and resource-intensive, impacting their accessibility and reproducibility across different studies. Despite these limitations, the potential applications of artificial scaffolds and biofilms in personalized medicine and interdisciplinary collaboration offer promising avenues for developing more effective antimicrobial therapies (Dongari-Bagtzoglou, 2008).

The challenges in utilizing artificial biofilm models are well-documented in the literature. These models may not entirely capture the host's immune responses or the full spectrum of stresses and stimuli encountered within living organisms, impacting their translational relevance to clinical settings. Furthermore, the technical complexity and resource-intensiveness of fabricating and maintaining artificial scaffolds and biofilms can limit their accessibility and reproducibility across different studies, affecting the comparability of results. These challenges underscore the need for ongoing technological and methodological innovations to enhance the fidelity and ease of use of artificial biofilm models (Dongari-Bagtzoglou, 2008).

In conclusion, while artificial scaffolds and biofilms offer valuable insights into bacterial behavior and antibiotic resistance mechanisms, their limitations necessitate continued innovation and interdisciplinary collaboration to enhance their utility and impact. Addressing these challenges and exploring new applications can pave the way for breakthroughs in understanding and treating biofilm-

related infections, ultimately contributing to the development of more effective and targeted antimicrobial therapies (Dongari-Bagtzoglou, 2008).

V. CONCLUSION

In this literature review, we have explored the critical role of artificial scaffolds and biofilms in antibiotic research, highlighting their significance in advancing our understanding of bacterial communities and developing new strategies to combat antibiotic resistance. These innovative models represent a pivotal shift from traditional research methods, providing a more nuanced and realistic simulation of the biofilm environment that plays a crucial role in bacterial survival, antibiotic resistance, and infection persistence. By enabling the study of bacterial behavior, interaction, and resistance development in conditions that closely mirror their natural habitats, artificial scaffolds and biofilms offer invaluable insights into the mechanisms underlying biofilm formation, the efficacy of antibiotic penetration, and the evolution of resistance.

The importance of continued innovation in the design, application, and analysis of artificial scaffolds and biofilms cannot be overstated. As we face one of the most pressing health challenges of our time—the rise of antibiotic-resistant infections—these models stand at the forefront of research efforts aimed at identifying new antibacterial compounds and elucidating the complex interactions within bacterial communities. The future of antibiotic research and development hinges on our ability to refine these models further, enhancing their relevance to clinical settings and expanding their application to encompass a broader range of bacterial species and infection contexts.

Looking ahead, the potential for interdisciplinary collaboration in this field is immense. By integrating advancements in materials science, microbiology, engineering, and computational modeling, researchers can develop more sophisticated and effective tools for studying biofilms and antibiotic resistance. This collaborative approach will not only accelerate the pace of discovery but also pave the way for personalized medicine strategies and the development of targeted treatments that can overcome the formidable defenses of biofilms.

In conclusion, artificial scaffolds and biofilms are indispensable in our ongoing battle against antibiotic-resistant bacteria. The insights gained from research utilizing these models have the potential to revolutionize the way we approach the development of antibiotics and the treatment of biofilm-associated infections. To address the evolving threat of antibiotic resistance, it is imperative that we continue to support and expand upon this innovative area of research, fostering a multidisciplinary approach that will lead to groundbreaking advancements in infectious disease treatment and prevention.

REFERENCES

[1] Pokharel, K., Dawadi, B., & Shrestha, L. (2022). Role of biofilm in bacterial infection and antimicrobial resistance. Journal of Nepal Medical Association, 60(253), 836-840. https://doi.org/10.31729/jnma.7580

[2] Penesyan, A., Nagy, S., Kjelleberg, S., Gillings, M., & Paulsen, I. (2019). Rapid microevolution of biofilm cells in response to antibiotics. NPJ Biofilms and Microbiomes, 5(1). https://doi.org/10.1038/s41522-019-0108-3

[3] Rodrigues, C., Boas, D., Haynes, K., & Henriques, M. (2018). The mnn2 gene knockout modulates the antifungal resistance of biofilms of candida glabrata. Biomolecules, 8(4), 130. https://doi.org/10.3390/biom8040130

[4] Chandra, J., Mukherjee, P., & Ghannoum, M. (2010). Fungal biofilms in the clinical lab setting. Current Fungal Infection Reports, 4(3), 137-144. https://doi.org/10.1007/s12281-010-0020-z

[5] Li, J., Fan, Q., Mao, C., Jin, M., Li, Y., & Wang, Y. (2020). Effect of biofilm formation on the escherichia coli drug resistance of isolates from pigs in central china. Indian Journal of Animal Research, (Of). https://doi.org/10.18805/ijar.b-1304

[6] Qian, W., Li, X., Yang, M., Liu, C., Kong, Y., Wang, T., … & Zhang, Q. (2022). Relationship between antibiotic resistance, biofilm formation, and biofilm-specific resistance in escherichia coli isolates from ningbo, china. Infection and Drug Resistance, Volume 15, 2865-2878. https://doi.org/10.2147/idr.s363652

[7] Shenkutie, A., Yao, M., Siu, G., Wong, B., & Leung, P. (2020). Biofilm-induced antibiotic resistance in clinical acinetobacter baumannii isolates. Antibiotics, 9(11), 817. https://doi.org/10.3390/antibiotics9110817

[8] Lebeaux, D., Chauhan, A., Rendueles, O., & Beloin, C. (2013). From in vitro to in vivo models of bacterial biofilm-related infections. Pathogens, 2(2), 288-356. https://doi.org/10.3390/pathogens2020288

[9] Macià, M. D., Rojo-Molinero, E., & Oliver, A. (2014). Antimicrobial susceptibility testing in biofilm-growing bacteria. Clinical Microbiology and Infection, 20(10), 981-990. https://doi.org/10.1111/1469-0691.12651

[10] Walters, M. C., Roe, F. L., Bugnicourt, A., Franklin, M. J., & Stewart, P. S. (2003). Contributions of antibiotic penetration, oxygen limitation, and low metabolic activity to tolerance of pseudomonas aeruginosa biofilms to ciprofloxacin and tobramycin. Antimicrobial Agents and Chemotherapy, 47(1), 317-323. https://doi.org/10.1128/aac.47.1.317-323.2003

[11] Otto, M. (2018). Staphylococcal biofilms. Microbiology Spectrum, 6(4). https://doi.org/10.1128/microbiolspec.gpp3-0023-2018

[12] Demirdjian, S., Sanchez, H., Hopkins, D., & Berwin, B. (2019). Motility-independent formation of antibiotic-tolerant pseudomonas aeruginosa aggregates. Applied and Environmental Microbiology, 85(14). https://doi.org/10.1128/aem.00844-19

[13] Jaskiewicz, M., Janczura, A., Nowicka, J., & Kamysz, W. (2019). Methods used for the eradication of staphylococcal biofilms. Antibiotics, 8(4), 174. https://doi.org/10.3390/antibiotics8040174

[14] Kragh, K., Hutchison, J., Melaugh, G., Rodesney, C., Roberts, A., Irie, Y., … & Bjarnsholt, T. (2016). Role of multicellular aggregates in biofilm formation. Mbio, 7(2). https://doi.org/10.1128/mbio.00237-16

[15] Kirchner, S., Fothergill, J. L., Wright, E. A., James, C. E., Mowat, E., & Winstanley, C. (2012). Use of artificial sputum medium to test antibiotic efficacy against pseudomonas aeruginosa in conditions more relevant to the cystic fibrosis lung. Journal of Visualized Experiments, (64). https://doi.org/10.3791/3857

[16] Albuquerque, M. T. P. d., Nagata, J. Y., & Bottino, M. C. (2017). Antimicrobial efficacy of triple antibiotic–eluting polymer nanofibers against multispecies biofilm. Journal of Endodontics, 43(9), S51-S56. https://doi.org/10.1016/j.joen.2017.06.009

[17] Davey, M. E. and O'Toole, G. A. (2000). Microbial biofilms: from ecology to molecular genetics. Microbiology and Molecular Biology Reviews, 64(4), 847-867. https://doi.org/10.1128/mmbr.64.4.847-867.2000

[18] Ting, D., Beuerman, R., Dua, H., Lakshminarayanan, R., & Mohammed, I. (2020). Strategies in translating the therapeutic potentials of host defense peptides. Frontiers in Immunology, 11. https://doi.org/10.3389/fimmu.2020.00983

[19] Chen, Z., Wang, Z., Ren, J., & Qu, X. (2018). Enzyme mimicry for combating bacteria and biofilms. Accounts of Chemical Research, 51(3), 789-799. https://doi.org/10.1021/acs.accounts.8b00011

[20] Shu, Z., Merino, N., Okamoto, A., & Gedalanga, P. (2018). Interkingdom microbial consortia mechanisms to guide biotechnological applications. Microbial Biotechnology, 11(5), 833-847. https://doi.org/10.1111/1751-7915.13300

[21] Nshogozabahizi, J., Aubrey, K., Ross, J., & Thakor, N. (2019). Applications and limitations of regulatoryrnaelements in synthetic biology and biotechnology. Journal of Applied Microbiology, 127(4), 968-984. https://doi.org/10.1111/jam.14270

[22] Georgiev, K., Filipov, I., & Pecheva, A. (2022). Biofilm reactor calibration for in vitro investigation of composite biodegradation. Folia Medica, 64(2), 248-251. https://doi.org/10.3897/folmed.64.e61540

[23] Guo, S., Dubuc, E., Rave, Y., Verhagen, M., Twisk, S., Hek, T., … & Greef, T. (2020). Engineered living materials based on adhesin-mediated trapping of programmable cells. Acs Synthetic Biology, 9(3), 475-485. https://doi.org/10.1021/acssynbio.9b00404

[24] Thi, M. T. T., Wibowo, D., & Rehm, B. H. A. (2020). Pseudomonas aeruginosa biofilms. International Journal of Molecular Sciences, 21(22), 8671. https://doi.org/10.3390/ijms21228671

[25] Wood, T. K., Knabel, S. J., & Kwan, B. W. (2013). Bacterial persister cell formation and dormancy. Applied and Environmental Microbiology, 79(23), 7116-7121. https://doi.org/10.1128/aem.02636-13

[26] Bottino, M. C., Kamocki, K., Yassen, G. H., Platt, J. A., Vail, M. M., Ehrlich, Y., … & Gregory, R. L. (2013). Bioactive nanofibrous scaffolds for regenerative endodontics. Journal of Dental Research, 92(11), 963-969. https://doi.org/10.1177/0022034513505770

[27] Lattwein, K. R., Shekhar, H., Kouijzer, J. J. P., Wamel, W. J. B. v., Holland, C. K., & Kooiman, K. (2020). Sonobactericide: an emerging treatment strategy for bacterial infections. Ultrasound in Medicine &Amp; Biology, 46(2), 193-215. https://doi.org/10.1016/j.ultrasmedbio.2019.09.011

[28] Cárdenas-Calderón, C., Veloso-Giménez, V., González, T., Wozniak, A., García, P., Martín, S. S., … & Egaña, J. T. (2022). Development of an implantable three-dimensional model of a functional pathogenic multispecies biofilm to study infected wounds. Scientific Reports, 12(1). https://doi.org/10.1038/s41598-022-25569-5

[29] Lee, J., Park, J., Son, K., & Lee, J. W. (2022). Pcl/sodium-alginate based 3d-printed dual drug delivery system with antibacterial activity for osteomyelitis therapy. Gels, 8(3), 163. https://doi.org/10.3390/gels8030163

[30] Aldrich, A., Kuss, M., Duan, B., & Kielian, T. (2019). 3d bioprinted scaffolds containing viable macrophages and antibiotics promote clearance of staphylococcus aureus craniotomy-associated biofilm infection. ACS Applied Materials &Amp; Interfaces, 11(13), 12298-12307. https://doi.org/10.1021/acsami.9b00264

[31] Rafiee, A., Memarpour, M., Najibi, Y., Khalvati, B., Kianpour, S., & Morowvat, M. (2020). Antimicrobial efficacy of a novel antibiotic-eluting injectable platelet-rich fibrin scaffold against a dual-species biofilm in an infected immature root canal model. Biomed Research International, 2020, 1-8. https://doi.org/10.1155/2020/6623830

[32] Borriello, G., Werner, E. M., Roe, F. L., Kim, A. M., Ehrlich, G. D., & Stewart, P. S. (2004). Oxygen limitation contributes to antibiotic tolerance of pseudomonas aeruginosa in biofilms. Antimicrobial Agents and Chemotherapy, 48(7), 2659-2664. https://doi.org/10.1128/aac.48.7.2659-2664.2004

[33] Saxena, P., Joshi, Y., Rawat, K., & Bisht, R. (2018). Biofilms: architecture, resistance, quorum sensing and control mechanisms. Indian Journal of Microbiology, 59(1), 3-12. https://doi.org/10.1007/s12088-018-0757-6

[34] Akanda, Z. Z., Taha, M., & Abdelbary, H. (2017). Current review—the rise of bacteriophage as a unique therapeutic platform in treating peri-prosthetic joint infections. Journal of Orthopaedic Research, 36(4), 1051-1060. https://doi.org/10.1002/jor.23755

[35] Kumaran, D., Taha, M., Yi, Q., Ramírez-Arcos, S., Diallo, J., Carli, A., … & Abdelbary, H. (2018). Does treatment order matter? investigating the ability of bacteriophage to augment antibiotic activity against staphylococcus aureus biofilms. Frontiers in Microbiology, 9. https://doi.org/10.3389/fmicb.2018.00127

[36] Albuquerque, M. T. P. d., Ryan, S. J., Münchow, E. A., Kamocka, M. M., Gregory, R. L., Valera, M. C., … & Bottino, M. C. (2015). Antimicrobial effects of novel triple antibiotic paste–mimic scaffolds on actinomyces naeslundii

biofilm. Journal of Endodontics, 41(8), 1337-1343. https://doi.org/10.1016/j.joen.2015.03.005

[37] Sultana, S. T., Atçı, E., Babauta, J. T., Falghoush, A., Snekvik, K., Call, D. R., … & Beyenal, H. (2015). Electrochemical scaffold generates localized, low concentration of hydrogen peroxide that inhibits bacterial pathogens and biofilms. Scientific Reports, 5(1). https://doi.org/10.1038/srep14908

[38] Sultana, S. T., Call, D. R., & Beyenal, H. (2016). Eradication of pseudomonas aeruginosa biofilms and persister cells using an electrochemical scaffold and enhanced antibiotic susceptibility. NPJ Biofilms and Microbiomes, 2(1). https://doi.org/10.1038/s41522-016-0003-0

[39] Ma, D., Shanks, R. M. Q., Davis, C. M., Craft, D. W., Wood, T. K., Hamlin, B. R., … & Urish, K. L. (2017). Viable bacteria persist on antibiotic spacers following two-stage revision for periprosthetic joint infection. Journal of Orthopaedic Research, 36(1), 452-458. https://doi.org/10.1002/jor.23611

[40] Quan, K., Zhang, Z., Hong, C., Ren, X., Ren, Y., Peterson, B. W., … & Busscher, H. J. (2019). Artificial channels in an infectious biofilm created by magnetic nanoparticles enhanced bacterial killing by antibiotics. Small, 15(39). https://doi.org/10.1002/smll.201902313

[41] Lv, X., Wang, L., Mei, A., Xu, Y., Ruan, X., Wang, W., … & Dong, X. (2022). Recent nanotechnologies to overcome the bacterial biofilm matrix barriers. Small, 19(6). https://doi.org/10.1002/smll.202206220

[42] Jewell, M. P., Galyean, A. A., Harris, J. K., Zemanick, E. T., & Cash, K. J. (2019). Luminescent nanosensors for ratiometric monitoring of three-dimensional oxygen gradients in laboratory and clinical pseudomonas aeruginosa biofilms. Applied and Environmental Microbiology, 85(20). https://doi.org/10.1128/aem.01116-19

[43] Jiang, N., Dusane, D. H., Brooks, J. R., Delury, C., Aiken, S. S., Laycock, P. A., … & Stoodley, P. (2021). Antibiotic loaded β-tricalcium phosphate/calcium sulfate for antimicrobial potency, prevention and killing efficacy of pseudomonas aeruginosa and staphylococcus aureus biofilms. Scientific Reports, 11(1). https://doi.org/10.1038/s41598-020-80764-6

[44] Chang, C., Yu, X., Guo, W., Guo, C., Guo, X., Li, Q., … & Zhu, Y. (2022). Bacteriophage-mediated control of biofilm: a promising new dawn for the future. Frontiers in Microbiology, 13. https://doi.org/10.3389/fmicb.2022.825828

[45] Tao, Q., Wu, Q., Zhang, Z., Liu, J., Tian, C., Huang, Z., … & Yong, Z. (2022). Meta-analysis for the global prevalence of foodborne pathogens exhibiting antibiotic resistance and biofilm formation. Frontiers in Microbiology, 13. https://doi.org/10.3389/fmicb.2022.906490

[46] Dongari-Bagtzoglou, A. (2008). Pathogenesis of mucosal biofilm infections: challenges and progress. Expert Review of Anti-Infective Therapy, 6(2), 201-208. https://doi.org/10.1586/14787210.6.2.201

International Journal of Advanced Engineering Research and Science (IJAERS)
Peer-Reviewed Journal
ISSN: 2349-6495(P) | 2456-1908(O)
Vol-11, Issue-2; Feb, 2024
Journal Home Page Available: https://ijaers.com/
Article DOI: https://dx.doi.org/10.22161/ijaers.112.5

Power budget Analysis for Passive Optical Network Deployment as Mobile Communication Backhaul Network

Okeke Remigius Obinna[1], Idigo Victor Eze[2]

[1]Department of Electrical and Electronic Engineering, University of Port Harcourt, Choba, Rivers State, Nigeria.
[2]Department of Electronic and Computer Engineering, Nnamdi Azikiwe University, Awka, Anambra State, Nigeria.

Received: 15 Dec 2023,

Receive in revised form: 26 Jan 2024,

Accepted: 10 Feb 2024,

Available online: 22 Feb 2024

***Keywords*— PON, Power budget, upstream, downstream, DCF, margin, attenuation, ONU, OLT,**

***Abstract*—** *This study focused on providing a robust power budget analysis for Passive Optical Network (PON) deployed as a backhaul network for a mobile communication network in Port Harcourt Nigeria. In this research, optimal power budget model for both upstream and downstream transmission was introduced. The power budget model developed is a bidirectional Passive Optical Network transmission tailored for Cellular Backhaul purposes. The focus is SMILE 4G Mobile Networks, operating in the geographical area of Port Harcourt, Rivers State, Nigeria. Utilizing the coordinates of all the SMILE eNBs in port Harcourt, and adopting systematic/ automatic approach for optimal splitter coordinates, fibre lengths between each eNB and the splitter was obtained. This approach ensures the lowest length of fibre which translates that cheapest cost of deployment was achieved. Employing parameters like attenuation, margin, etc, power budget analysis for both downstream and upstream transmission was obtained. From the results, it was evident that eNBs with longer fibre cable lengths exhibit correspondingly higher levels of fibre attenuation but lower margin values. This consistent pattern was observed across all the eNBs within the network for both Upstream and Downstream transmissions. Power Budget achieved in this research ensured that attenuation was greatly reduced and significant power was available for both transmitter and receiver sensitivity.*

I. INTRODUCTION

Passive Optical Network, known as a PON, is essentially an optical network that operates in a point-to-multipoint or multipoint-to-point configuration. It facilitates the optical transmission of various forms of information, including voice, data, and video, between a central point referred to as the Optical Line Terminal (OLT) and other endpoints known as Optical Network Units (ONUs). A typical PON setup comprises a central node, the OLT, and multiple ONUs connected by fiber optics and splitters. When designing Passive Optical Networks with cellular backhaul capabilities, several factors need to be taken into account to ensure the project's success. One of these crucial considerations is power budgeting. In this research Power budget analysis for a PON network is presented. PON is a fibre optic technology and fibre optics can be categorized into different classes (Class A, B, B+, C, and C+) based on their power budget. These classifications are determined by various Passive Optical Network (PON) deployment scenarios, which take into account both the split ratios and the available power budget. A white paper presented by ADC Telecommunications in 2006 [1] specifies that for Broadband PON (BPON) with a maximum split ratio of 32

falls into Class A, B, and C optics when the power budget is 20dB, 25dB, and 30dB, respectively. Similarly, Gigabit PON (GPON) with a maximum logical split ratio of 64 is classified into Class A, B, B+, and C optics, depending on whether the power budget is 20dB, 25dB, 28dB, or 30dB.

In a related study, the Calix User Group presented an article during their conference in 2016 [2] that also categorizes PON networks into classes, assigning power budgets as follows: Class A, Class B, Class B+, Class C, and Class C+ with power budgets of 20dB, 25dB, 28dB, 30dB, and 32dB, respectively. It's worth noting that despite these classifications, the actual optical link budgets may sometimes be influenced by factors such as the operator's choice of active components, including lasers, receivers, and PON chips, as well as the type of protection mechanisms employed.

The calculations for the power budget in this study are conducted in two parts: downstream and upstream budgets (downstream-when OLT is sending while ONUs receiving and Upstream-when ONUs are sending while OLT is receiving). According to [3], commercially available single-mode connectors typically exhibit losses of less than 0.5dB, while the splice loss for a single-mode fibre is approximately 0.1dB. The National Electrical Contractors Association [4] also confirms a splice loss of 0.1dB for single-mode fibre. Transition networks [5], suggests that the typical distance between two splices is 6km, and the minimum value for the safety margin usually starts at 3dB, though it may vary depending on the specific design.

Given the typical 6km distance between two splices, the design plan anticipates three splicing points (worst case) for each OLT-ONU connection, considering the fibre length as given in table 3. Table 1 presents the expected losses within the system, including connector losses at OLT, ONU, WDM mux, WDM demux, power splitter, fibre ends, DCF ends, and the switch. The switch will be utilized to transfer transmissions to the protection link in the event of a failure. To ensure a consistent OLT transmit power for each OLT-ONU pair, a variable margin will be applied. This margin, denoted by varying values in the design, accounts for unforeseen losses and those stemming from the chosen protection scheme. It's important to note that the ITU-T specifies a maximum loss of 32dB for Class C+ optics.

Table 1: Expected losses per component in the system

Components Losses	**Quantity**	**Values (dB)**
Splice	3 x 0.1	0.3dB
Connectors with insertion loss from OLT, ONU and Switch	(each 0.5dB)	0.5dB each
Fibre Attenuation @ 1560 or 1310	Length x attenuation	0.25dB/km at 1550nm and 0.3dB/km at 1310 nm
WDM Mux/Dmux	(8x1)/(1x8)	< or = 3.5dB
Margin Power Splitter/Combiner	Protection and other Loss 1 x 4/4 x1	Variable 6.8dB per OLT-ONU pair
DCF attenuation	0.6dB/km	

II. RESEARCH METHODOLOGY

1.1 Location of Study

The study location is Port Harcourt, which is both the capital and the largest city of Rivers State in the southern region of Nigeria. Positioned along the Bonny River, Port Harcourt is situated 41 miles (66 km) upstream from the Gulf of Guinea. This locale has experienced significant population growth primarily attributed to the discovery of oil, subsequent exploration activities, and the development of related industries. Port Harcourt has become a hub for major oil and gas companies, which has, in turn, catalyzed substantial commercial activities within the city. As per Wikipedia [6], it is estimated that Port Harcourt is home to approximately 1,865,000 residents. Figure 2, shows a satellite view of Port Harcourt situated along the Bonny River upstream from the Gulf of Guinea.

The population of Port Harcourt can be segmented into three distinct subdivisions as follows:

(i) Densely Populated Areas: These regions are characterized by a high concentration of various establishments, including schools, hotels, residential and commercial buildings, places of worship such as churches and mosques, and the presence of multinational companies, among others. Notable areas falling under this category encompass D line, GRA phase 1-5, Aba Road, Woji, and more. Prominent businesses in these localities include the Port Harcourt Pleasure Park, Shell residential area, Meridiane Hospital, and Agip, to name a few. Given the significant population in these areas, a multitude of eNBs (enhanced Node B, a key component in mobile telecommunications) are strategically situated to support robust mobile network coverage.

(ii) Medium Population Areas: This classification pertains to areas with a moderate population density and a notable presence of businesses such as banks, schools, churches, and multinational companies. Notable examples

include Rumuokoro market, Choba market, and the University of Port Harcourt (Uniport).

(iii) Low Population Areas: In this category, areas with a sparse population and fewer business establishments are found. Locations like Emeoha, Ndele, and Elele communities fall within this classification.

Port Harcourt, owing to its dense population and urbanized environment, serves as a significant base for numerous mobile telecommunication network operators in Nigeria, contributing substantially to mobile traffic. It is worth noting that this research primarily focused on the SMILE 4G network provider.

For optimal power budgeting, the geographical location of the telecommunication nodes is a vital operation. The approach used to identify SMILE eNBs (enhanced Node Bs) in Port Harcourt involves the following steps:

(i) Data collection involving the acquisition of latitude and longitude coordinates for 60 eNB stations through the use of a network monitor application.

(ii) Data analysis, including the conversion of coordinates into radian measurements, the calculation of great circle distances, and the determination of walking distances between these coordinates.

In the quest to ascertain the best and optimal locations for the splitter for Passive Optical Network (PON) deployments, two methods, namely the 'Manual' and 'Automatic' approaches, were employed. The entries generated represented the highest and lowest values for fibre length, as well as the cost of fibre and attenuation incurred, respectively. Opting for the coordinates 4.82778640N, 7.0265820E as the optimal location results for splitter location, a total cumulative fibre length of 440.745 km was obtained. This choice, in turn, reduces both the cost of fibre procurement and the attenuation within the design. A comparison of the optimum splitter coordinates obtained from both methods, as presented in Table 2, reveals that both the manual and automatic/systematic methodologies yielded similar results for both locations and total distances. Table 2 also showed that both approaches yielded very similar values for both the great circle distance and walking distance. Additionally, it is evident that both approaches resulted in locations that are closely aligned.

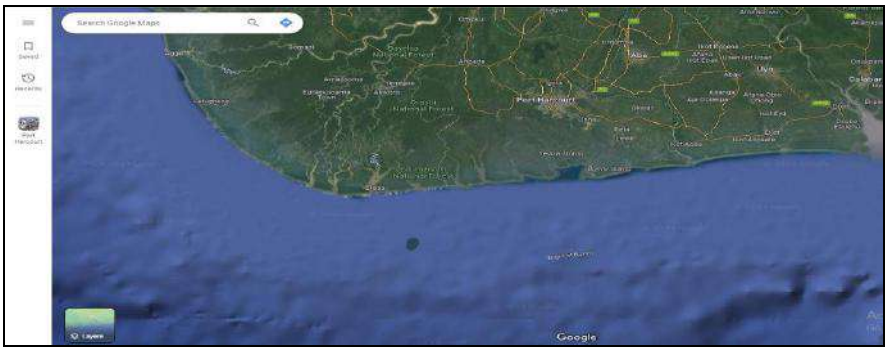

Fig.2: Satellite view of Port Harcourt

Table 2: Coordinates from Manual and Automatic/Systematic Methods (Computational Analysis of Optimal Splitter Coordinates for Passive Optical Network (PON) Deployment, R.O Okeke and V.E Idigo (2021))

METHOD	LOCATION	GREAT CIRCLE DISTANCE	WALKING DISTANCE
MANUAL	4.8277864, 7.026582	440.7447 KM	577.7 KM
AUTOMATIC	4.8276, 7.0254	440.2402 KM	564.45 KM

Based on research conducted by R.O Okeke and V.E Idigo in [7], the coordinates 4.82778640N, 7.0265820E is chosen as the optimal splitter location, optimal splitter location is needed to help determine the fibre length distribution for power budget calculation. Table 3 shows distribution of fibre lengths from the Splitter situated at the chosen optimal splitter location. For the purposes of this research, a total route length of 577km from table 3 is approximated 580km and was considered as the total fibre length. This approximation allows for contingencies and unforeseen factors during the design and power budgeting process. Furthermore, the walking distance values obtained from the Automatic approach were adopted for various OLT – ONU pairs.

Table 3: Breakdown of distances between coordinate 4.8277864^{0}N, 7.026582^{0}E, Exchange/ switch and eNBs

EXCHANGE/NODB PARAMETERS					SPLITTER PARAMETERS (1km from eNB1 to eNB 2)				GREAT CIRCLE DISTANCE (KM)	WALKING DISTANCE (KM)
	LAT1 (Degrees)	LAT1 (Radians)	LONG1 (Degrees)	LONG1 (Radians)	LAT2 (Degrees)	LAT2 (Radians)	LONG2 (Degrees)	LONG2 (Radians)		
exchange	4.808117	0.08392	6.996657	0.12211	4.8277864	0.0842604	7.026582	0.1226365	3.97211	6.2
eNB 1	4.8366	0.08441	7.0286	0.12267	4.827786	0.08426	7.026582	0.122636	1.005203	1.6
eNB 2	4.7737	0.08332	7.0142	0.12242	4.827786	0.08426	7.026582	0.122636	6.16862	10.2
eNB 3	4.7999	0.08377	6.9939	0.12207	4.827786	0.08426	7.026582	0.122636	4.767435	6.1
eNB 4	4.8294	0.08429	7.0919	0.12378	4.827786	0.08426	7.026582	0.122636	7.239448	10
eNB 5	4.7706	0.08326	7.0224	0.12256	4.827786	0.08426	7.026582	0.122636	6.375677	8.1
eNB 6	4.8746	0.08508	6.983	0.12188	4.827786	0.08426	7.026582	0.122636	7.100198	10.1
eNB 7	4.8692	0.08498	7.1137	0.12416	4.827786	0.08426	7.026582	0.122636	10.69458	13.7
eNB 8	4.7196	0.08237	7.1518	0.12482	4.827786	0.08426	7.026582	0.122636	18.36402	23.6
eNB 9	4.8554	0.08474	7.0641	0.12329	4.827786	0.08426	7.026582	0.122636	5.167951	6
eNB 10	4.7909	0.08362	7.1207	0.12428	4.827786	0.08426	7.026582	0.122636	11.20614	14.3
eNB 11	4.7854	0.08352	7.0082	0.12232	4.827786	0.08426	7.026582	0.122636	5.13441	6.4
eNB 12	4.8327	0.08435	7.0685	0.12337	4.827786	0.08426	7.026582	0.122636	4.676523	7.2
eNB 13	4.8039	0.08384	6.9883	0.12197	4.827786	0.08426	7.026582	0.122636	5.00467	6.9
eNB 14	4.8197	0.08412	7.0656	0.12332	4.827786	0.08426	7.026582	0.122636	4.415736	6.7
eNB 15	4.743	0.08278	7.0417	0.1229	4.827786	0.08426	7.026582	0.122636	9.575454	12.6
eNB 16	4.7939	0.08367	7.0308	0.12271	4.827786	0.08426	7.026582	0.122636	3.796858	5.5
eNB 17	4.748	0.08287	7.0989	0.1239	4.827786	0.08426	7.026582	0.122636	11.955	18.9
eNB 18	4.7773	0.08338	7.062	0.12325	4.827786	0.08426	7.026582	0.122636	6.849545	8.2
eNB 19	4.8341	0.08437	6.9845	0.1219	4.827786	0.08426	7.026582	0.122636	4.715218	6
eNB 20	4.8565	0.08476	7.0405	0.12288	4.827786	0.08426	7.026582	0.122636	3.545691	4.9
eNB 21	4.8064	0.08389	7.0424	0.12291	4.827786	0.08426	7.026582	0.122636	2.954143	4.3
eNB 22	4.8146	0.08403	6.9788	0.1218	4.827786	0.08426	7.026582	0.122636	5.493586	7.6
eNB 23	4.8298	0.0843	6.9588	0.12145	4.827786	0.08426	7.026582	0.122636	7.51357	9.3
eNB 24	4.8923	0.08539	6.9143	0.12068	4.827786	0.08426	7.026582	0.122636	14.36035	16.5
eNB 25	4.848	0.08461	7.0492	0.12303	4.827786	0.08426	7.026582	0.122636	3.366318	4
eNB 26	4.8514	0.08467	6.9835	0.12188	4.827786	0.08426	7.026582	0.122636	5.447904	7.7
eNB 27	4.8081	0.08392	6.9967	0.12211	4.827786	0.08426	7.026582	0.122636	3.969176	5.3
eNB 28	4.9028	0.08557	6.999	0.12216	4.827786	0.08426	7.026582	0.122636	8.88327	11.5
eNB 29	4.9789	0.0869	6.9611	0.12149	4.827786	0.08426	7.026582	0.122636	18.30218	23.7
eNB 30	4.9969	0.08721	6.95	0.1213	4.827786	0.08426	7.026582	0.122636	20.62986	24.4
eNB 31	4.9539	0.08646	7.0111	0.12237	4.827786	0.08426	7.026582	0.122636	14.12764	17.3
eNB 32	4.9669	0.08669	6.9869	0.12194	4.827786	0.08426	7.026582	0.122636	16.08126	20.7
eNB 33	4.8289	0.08428	7.0219	0.12255	4.827786	0.08426	7.026582	0.122636	0.533338	1
eNB 34	4.8169	0.08407	7.0112	0.12237	4.827786	0.08426	7.026582	0.122636	2.09048	3.1
eNB 35	4.9317	0.08607	7.0021	0.12221	4.827786	0.08426	7.026582	0.122636	11.86871	14.5
eNB 36	4.8407	0.08449	6.9681	0.12162	4.827786	0.08426	7.026582	0.122636	6.636936	8.3
eNB 37	4.8598	0.08482	6.9792	0.12181	4.827786	0.08426	7.026582	0.122636	6.342878	8.6
eNB 38	4.8469	0.08459	7.0369	0.12282	4.827786	0.08426	7.026582	0.122636	2.413286	3.3
eNB 39	4.8585	0.0848	6.9658	0.12158	4.827786	0.08426	7.026582	0.122636	7.550949	9.1
eNB 40	4.88	0.08517	7.01	0.12235	4.827786	0.08426	7.026582	0.122636	6.089612	8.1

eNB 41	4.8669	0.08494	7.03	0.1227	4.827786	0.08426	7.026582	0.122636	4.36567	7.1
eNB 42	4.8378	0.08444	7.037	0.12282	4.827786	0.08426	7.026582	0.122636	1.603808	2.1
eNB 43	4.8842	0.08525	7.138	0.12458	4.827786	0.08426	7.026582	0.122636	13.84695	17.7
eNB 44	4.7815	0.08345	7.0398	0.12287	4.827786	0.08426	7.026582	0.122636	5.351128	6.3
eNB 45	4.8116	0.08398	6.9561	0.12141	4.827786	0.08426	7.026582	0.122636	8.014217	10.6
eNB 46	4.9011	0.08554	6.9269	0.1209	4.827786	0.08426	7.026582	0.122636	13.72697	17
eNB 47	4.9058	0.08562	6.9066	0.12054	4.827786	0.08426	7.026582	0.122636	15.87325	18.4
eNB 48	4.8024	0.08382	6.944	0.1212	4.827786	0.08426	7.026582	0.122636	9.575779	12.4
eNB 49	4.8354	0.08439	7.0528	0.12309	4.827786	0.08426	7.026582	0.122636	3.025785	4.4
eNB 50	4.7947	0.08368	7.0497	0.12304	4.827786	0.08426	7.026582	0.122636	4.482936	5.9
eNB 51	4.7581	0.08304	7.0119	0.12238	4.827786	0.08426	7.026582	0.122636	7.917683	10
eNB 52	4.8269	0.08424	6.9961	0.1221	4.827786	0.08426	7.026582	0.122636	3.378845	4.7
eNB 53	4.815	0.08404	7.0419	0.1229	4.827786	0.08426	7.026582	0.122636	2.214073	3.3
eNB 54	4.71	0.0822	7.165	0.12505	4.827786	0.08426	7.026582	0.122636	20.16908	25.3
eNB 55	4.8233	0.08418	7.0572	0.12317	4.827786	0.08426	7.026582	0.122636	3.428968	5.8
eNB 56	4.815	0.08404	7.0652	0.12331	4.827786	0.08426	7.026582	0.122636	4.508943	6.7
eNB 57	4.894	0.08542	7.0153	0.12244	4.827786	0.08426	7.026582	0.122636	7.467938	10
eNB 58	4.8626	0.08487	7.0153	0.12244	4.827786	0.08426	7.026582	0.122636	4.067895	6.3
eNB 59	4.8276	0.08426	7.0145	0.12243	4.827786	0.08426	7.026582	0.122636	1.338846	2.2
									440.7447	577.7

1.2 Calculating For Downstream Power Budget

In this backhaul network design, a PON (Passive Optical Network) link with a capacity of 160Gbit/s (comprising two 80Gbit/s streams), extending from the Optical Line Terminal (OLT) to the splitter is considered. The PON network is designed to have a bidirectional transmission and these are Downstream (when the OLT is transmitting to the ONUs) and upstream transmission (when each ONUs are transmitting to the OLT). To achieve the 80Gbit/s data rate, eight 10Gbit/s PON connections were employed, and these are aggregated using an 8x1 multiplexer. Additionally, a switch is incorporated to facilitate the seamless transfer of traffic from the active link to the protection link in case of an active network failure. It's important to note that the losses incurred by these components have been factored into the power budget calculations. The individual losses associated with each of these equipment elements are detailed below:

(i) Connection loss from eight 10Gbit/s OLT = 0.5 x 8 = 4dB (need 80Gbit/s)

(ii) Connection loss from switch = 0.5dB

(iii) Connection loss from the ONU =0.5dB

(iv) Insertion loss from 1 x 8 WDM demultiplexer = 3.5dB

(v) Insertion loss from 8 x 1 WDM multiplexer = 3.5dB

(vi) 1x 4 splitter insertion loss = 6.8dB

(vii) Attenuation at 1550nm =0.25 x fibre length

(viii) Attenuation at 1310nm = 0.3 x fibre length

(ix) Attenuation of DCF = 0.6 x DCF length

(x) Splice loss = 0.1dB

(xi) Margin = Variable

From the proposed network diagram shown in figure 3, aside connection losses due to i, ii and iii above, the network has additional 4 connections in between and that made up a 2dB loss. Total loss due to connections is 4+0.5+0.5+2 = 7dB. Since the losses in the system is established, the transmit power of the OLT in the downstream direction can also be obtained. Equation 1 is PON power budget formula used for the OLT transmit power calculation in the downstream direction.

OLT Tx - ONU Rx = atten x fibre length
+ atten x DCF length
+ WDM mux loss + WDM demux loss
+ Splitter loss + connector losses
+ splice losses + Margin (1)

Where OLT Tx = OLT transmit Power; ONU Rx = ONU receiver sensitivity; atten x fibre length = loss due to length of fibre cable; atten x DCF length = loss due to dispersion compensation fibre; WDM mux loss = insertion loss due to WDM multiplexer; WDM demux loss = insertion loss due to WDM demultiplexer; Connector losses = losses accrued due to connectors; Splice losses = losses accrued due to splicing; Margin = varying value of loss in the system that will take care for unaccounted losses and as such keep all OLT Tx and all ONU Rx value constant on every OLT-ONU pair.

The process of determining the losses, margin, and ONU Rx for each OLT Tx - ONU Rx pair, as previously outlined, is replicated for all 60 OLT Tx – ONU Rx pairs

employing a spreadsheet. The outcomes of this analysis are presented in Table 4. The margin is applied to ensure consistent losses across all 60 OLT – ONU pairs.

The margin is varied in each case to maintain the same loss for the entire OLT – ONU pairs and as such to maintain constant ONU Rx for each. The range of values for the margin is 3.11– 9.32dB.

Parameters:

(i) Attenuation at 1550nm downstream is 0.25dB/km

(ii) Maximum loss for class C+ is 32dB as specified by ITU –T

(iii) In downstream, OLT Tx is usually from 3 - 7dBm and ONU Rx is -32dBm maximum while in upstream direction, ONU Tx is always from 0.5 – 5 dBm and OLT Rx is -30dBm for a worst case.

OLT - ONU1 pair calculation is as shown;

Fibre length = (4.8 + 1.4) km = 6.2km

Attenuation per length = 0.25 x 6.2 = 1.5dB/km

Loss due to DCF, atten x DCF length =

0.6 x 0.4km = 0.24dB/km

Loss due to connectors = 4 + 0.5 + 0.5 + 2 = 7dB

Loss due to splicing (3 possible splicing) = 0.1x 3 = 0.3dB

Insertion loss due to WDM mux =3.5dB

Insertion loss due to WDM demux = 3.5dB

Insertion loss due to 1 x 4 Splitter = 6.8dB

Margin = unknown (varies)

From equation 1,

OLT Tx - ONU Rx = (1.5dB/km + 0.24dB/km + 3.5dB + 3.5dB + 6.8dB + 7dB + 0.3dB + M)

OLT Tx - ONU Rx = (22.84 + M)dB

Hence, total loss;

32 = 22.84 + M

M = 32 - 22.84 = 9.16dB (margin for OLT - ONU1 pair)

Assuming the lowest OLT Tx power (3dBm) for class C+ optics is adopted, OLT Tx power becomes 3dBm; hence, equation 1 becomes:

3 - (ONU1 Rx) = 22.84 + M

ONU1 Rx = - 29dBm

The network is divided into two segments for ease of presentation, segment A consist of ONU 1 to ONU 32 while segment B covered ONU 33 to ONU 59. Figure 3 is a block diagram showing Segment A

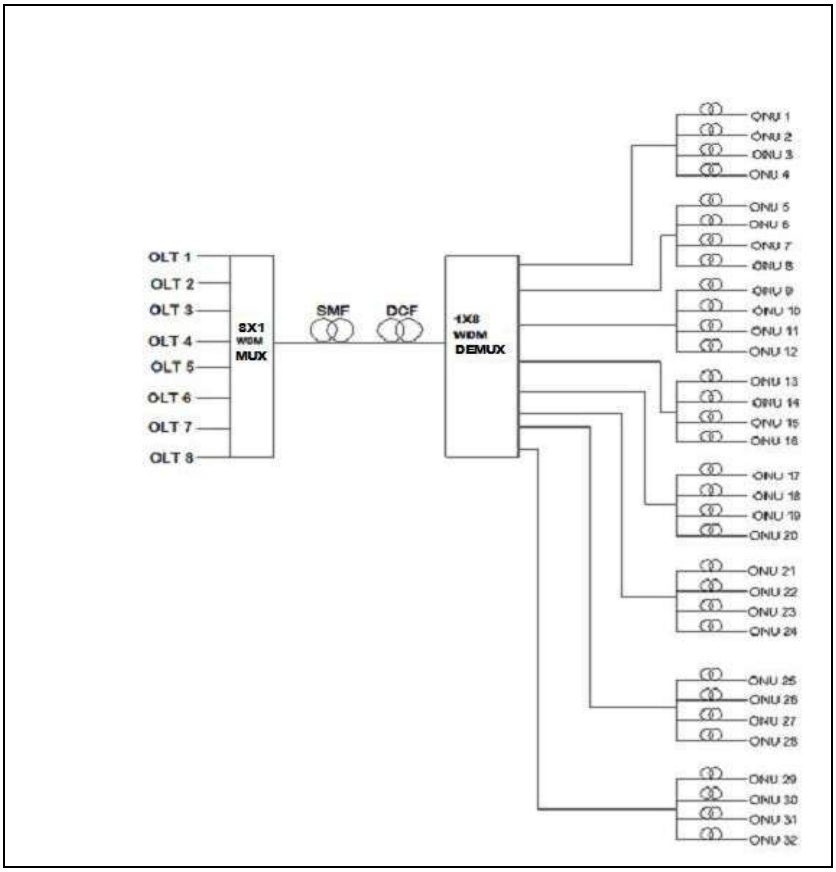

Fig.3: Block diagram of segment A of the network

Table 4: Downstream Power Budget

S/N	OLT TX (dBm)	ONU RX (dBm)	FIBRE LTH (km)	ATTN (dB/km)	FIBRE ATTN (dB/km)	DCF LTH (km)	ATTN (dB/km)	DCF ATTN (dB/km)	WDM MUX LOSS (dB)	WDM DEMUX LOSS (dB)	SPT. LOSS (dB)	CONNT. LOSS (dB)	SPL. LOSS (dB)	MARGIN (dB)
eNB1	3	-29	6.2	0.25	1.55	0.4	0.6	0.24	3.5	3.5	6.8	7	0.3	9.11
eNB2	3	-29	12.6	0.25	3.15	0.4	0.6	0.24	3.5	3.5	6.8	7	0.3	7.51
eNB3	3	-29	10.4	0.25	2.6	0.4	0.6	0.24	3.5	3.5	6.8	7	0.3	8.06
eNB4	3	-29	14.9	0.25	3.725	0.4	0.6	0.24	3.5	3.5	6.8	7	0.3	6.935
eNB5	3	-29	12.5	0.25	3.125	0.4	0.6	0.24	3.5	3.5	6.8	7	0.3	7.535
eNB6	3	-29	14.5	0.25	3.625	0.4	0.6	0.24	3.5	3.5	6.8	7	0.3	7.035
eNB7	3	-29	18.6	0.25	4.65	0.4	0.6	0.24	3.5	3.5	6.8	7	0.3	6.01
eNB8	3	-29	28.5	0.25	7.125	0.4	0.6	0.24	3.5	3.5	6.8	7	0.3	3.535
eNB9	3	-29	10.8	0.25	2.7	0.4	0.6	0.24	3.5	3.5	6.8	7	0.3	7.96
eNB10	3	-29	19.1	0.25	4.775	0.4	0.6	0.24	3.5	3.5	6.8	7	0.3	5.885
eNB11	3	-29	10.7	0.25	2.675	0.4	0.6	0.24	3.5	3.5	6.8	7	0.3	7.985
eNB12	3	-29	12.1	0.25	3.025	0.4	0.6	0.24	3.5	3.5	6.8	7	0.3	7.635
eNB13	3	-29	11.3	0.25	2.825	0.4	0.6	0.24	3.5	3.5	6.8	7	0.3	7.835
eNB14	3	-29	11.9	0.25	2.975	0.4	0.6	0.24	3.5	3.5	6.8	7	0.3	7.685
eNB15	3	-29	16.9	0.25	4.225	0.4	0.6	0.24	3.5	3.5	6.8	7	0.3	6.435
eNB16	3	-29	9.8	0.25	2.45	0.4	0.6	0.24	3.5	3.5	6.8	7	0.3	8.21
eNB17	3	-29	23.8	0.25	5.95	0.4	0.6	0.24	3.5	3.5	6.8	7	0.3	4.71
eNB18	3	-29	12.9	0.25	3.225	0.4	0.6	0.24	3.5	3.5	6.8	7	0.3	7.435
eNB19	3	-29	10.8	0.25	2.7	0.4	0.6	0.24	3.5	3.5	6.8	7	0.3	7.96
eNB20	3	-29	9.6	0.25	2.4	0.4	0.6	0.24	3.5	3.5	6.8	7	0.3	8.26
eNB21	3	-29	8.6	0.25	2.15	0.4	0.6	0.24	3.5	3.5	6.8	7	0.3	8.51
eNB22	3	-29	11.9	0.25	2.975	0.4	0.6	0.24	3.5	3.5	6.8	7	0.3	7.685
eNB23	3	-29	13.7	0.25	3.425	0.4	0.6	0.24	3.5	3.5	6.8	7	0.3	7.235
eNB24	3	-29	21.3	0.25	5.325	0.4	0.6	0.24	3.5	3.5	6.8	7	0.3	5.335
eNB25	3	-29	8.8	0.25	2.2	0.4	0.6	0.24	3.5	3.5	6.8	7	0.3	8.46
eNB26	3	-29	12.6	0.25	3.15	0.4	0.6	0.24	3.5	3.5	6.8	7	0.3	7.51
eNB27	3	-29	9.6	0.25	2.4	0.4	0.6	0.24	3.5	3.5	6.8	7	0.3	8.26
eNB28	3	-29	16	0.25	4	0.4	0.6	0.24	3.5	3.5	6.8	7	0.3	6.66
eNB29	3	-29	28.3	0.25	7.075	0.4	0.6	0.24	3.5	3.5	6.8	7	0.3	3.585
eNB30	3	-29	28.9	0.25	7.225	0.4	0.6	0.24	3.5	3.5	6.8	7	0.3	3.435
eNB31	3	-29	21.8	0.25	5.45	0.4	0.6	0.24	3.5	3.5	6.8	7	0.3	5.21
eNB32	3	-29	25.2	0.25	6.3	0.4	0.6	0.24	3.5	3.5	6.8	7	0.3	4.36
eNB33	3	-29	5.35	0.25	1.3375	0.4	0.6	0.24	3.5	3.5	6.8	7	0.3	9.3225
eNB34	3	-29	7.4	0.25	1.85	0.4	0.6	0.24	3.5	3.5	6.8	7	0.3	8.81
eNB35	3	-29	19.1	0.25	4.775	0.4	0.6	0.24	3.5	3.5	6.8	7	0.3	5.885
eNB36	3	-29	13.1	0.25	3.275	0.4	0.6	0.24	3.5	3.5	6.8	7	0.3	7.385
eNB37	3	-29	13.5	0.25	3.375	0.4	0.6	0.24	3.5	3.5	6.8	7	0.3	7.285
eNB38	3	-29	7.9	0.25	1.975	0.4	0.6	0.24	3.5	3.5	6.8	7	0.3	8.685
eNB39	3	-29	13.9	0.25	3.475	0.4	0.6	0.24	3.5	3.5	6.8	7	0.3	7.185
eNB40	3	-29	12.6	0.25	3.15	0.4	0.6	0.24	3.5	3.5	6.8	7	0.3	7.51

eNB41	3	-29	11.7	0.25	2.925	0.4	0.6	0.24	3.5	3.5	6.8	7	0.3	7.735
eNB42	3	-29	7	0.25	1.75	0.4	0.6	0.24	3.5	3.5	6.8	7	0.3	8.91
eNB43	3	-29	22.6	0.25	5.65	0.4	0.6	0.24	3.5	3.5	6.8	7	0.3	5.01
eNB44	3	-29	10.6	0.25	2.65	0.4	0.6	0.24	3.5	3.5	6.8	7	0.3	8.01
eNB45	3	-29	15	0.25	3.75	0.4	0.6	0.24	3.5	3.5	6.8	7	0.3	6.91
eNB46	3	-29	21.8	0.25	5.45	0.4	0.6	0.24	3.5	3.5	6.8	7	0.3	5.21
eNB47	3	-29	23.3	0.25	5.825	0.4	0.6	0.24	3.5	3.5	6.8	7	0.3	4.835
eNB48	3	-29	16.8	0.25	4.2	0.4	0.6	0.24	3.5	3.5	6.8	7	0.3	6.46
eNB49	3	-29	9.2	0.25	2.3	0.4	0.6	0.24	3.5	3.5	6.8	7	0.3	8.36
eNB50	3	-29	10.3	0.25	2.575	0.4	0.6	0.24	3.5	3.5	6.8	7	0.3	8.085
eNB51	3	-29	14.3	0.25	3.575	0.4	0.6	0.24	3.5	3.5	6.8	7	0.3	7.085
eNB52	3	-29	9	0.25	2.25	0.4	0.6	0.24	3.5	3.5	6.8	7	0.3	8.41
eNB53	3	-29	8.6	0.25	2.15	0.4	0.6	0.24	3.5	3.5	6.8	7	0.3	8.51
eNB54	3	-29	30.2	0.25	7.55	0.4	0.6	0.24	3.5	3.5	6.8	7	0.3	3.11
eNB55	3	-29	11	0.25	2.75	0.4	0.6	0.24	3.5	3.5	6.8	7	0.3	7.91
eNB56	3	-29	11.9	0.25	2.975	0.4	0.6	0.24	3.5	3.5	6.8	7	0.3	7.685
eNB57	3	-29	14.6	0.25	3.65	0.4	0.6	0.24	3.5	3.5	6.8	7	0.3	7.01
eNB58	3	-29	10.9	0.25	2.725	0.4	0.6	0.24	3.5	3.5	6.8	7	0.3	7.935
eNB59	3	-29	6.6	0.25	1.65	0.4	0.6	0.24	3.5	3.5	6.8	7	0.3	9.01

1.3 Calculating For Upstream Power Budget

Calculating for upstream, equation 2 is adopted:

ONU Tx - OLT Rx = atten x fibre length
+ atten x DCF length + WDM mux loss
+ WDM demux loss + combiner loss
+ connector losses + splice losses + Margin (2)

In this case, eNBs (ONUs) are transmitting and the power splitter is replaced by combiners. Attenuation coefficient at 1310nm window is used and it is 0.3dB/km. A worst case OLT Rx (-30dBm) for class C+ optics is adopted.

ONU1 Tx - OLT Rx pair calculation is as shown;

Fibre length = (4.8 + 1.4) km = 6.2km
Attenuation per length = 0.3 x 6.2 = 1.86dB/km
Loss due to DCF, atten x DCF length = 0.6 x 0.4km
= 0.24dB/km
Loss due to connection = 4 + 0.5 + 0.5 + 2 = 7dB
Loss due to splicing (3 possible splicing) = 0.1x 3 = 0.3dB
Insertion loss due to WDM mux =3.5dB
Insertion loss due to WDM demux = 3.5dB
Insertion loss due to 4 x 1 Combiner = 6.8dB
Margin = unknown (varies)

From equation 2,

ONU1 Tx - OLT Rx = (1.86dB/km + 0.24dB/km
+ 3.5dB + 3.5dB + 6.8dB + 7dB + 0.3dB + M)
ONU1 Tx - OLT Rx = (23.2 + M)

If a total loss of 32 is adopted because class C+ optics is considered, M =32-23.2 = 8.8dB

Assuming worst probable OLT Rx (sensitivity) for class C+ optics is adopted, OLT Rx power becomes -30dBm.

ONU1 Tx - (-30dBm) = 32dB (23.2 + 8.8)
ONU1 Tx = 2dBm

The method for calculating the losses, margin, and ONU Tx for every ONU Tx - OLT Rx pair, as detailed earlier, is reiterated for all 59 ONU Tx - OLT Rx pairs utilizing a spreadsheet. The outcomes of this process are displayed in Table 5. The margin is employed to ensure uniform losses across all 59 OLT – ONU pairs.

The margin is adjusted individually in each instance to uphold consistent loss levels across the entire range of OLT – ONU pairs. This adjustment is essential for maintaining a uniform ONU Tx for each pair. The margin values span a range from 1.60 dB to 9.055 dB.

Table 5: Upstream Power Budget

S/N	ONU TX (dBm)	OLT RX (dBm)	FIBRE LTH (km)	ATTN (dB/km)	FIBRE ATTN (dB/km)	DCF LTH (km)	ATTN (dB/km)	DCF ATTN (dB/km)	WDM MUX LOSS (dB)	WDM DEMUX LOSS (dB)	SP.T LOSS (dB)	CONNT. LOSS (dB)	SPL. LOSS (dB)	MARGIN (dB)
eNB1	2	-30	6.2	0.3	1.86	0.4	0.6	0.24	3.5	3.5	6.8	7	0.3	8.8
eNB2	2	-30	12.6	0.3	3.78	0.4	0.6	0.24	3.5	3.5	6.8	7	0.3	6.88
eNB3	2	-30	10.4	0.3	3.12	0.4	0.6	0.24	3.5	3.5	6.8	7	0.3	7.54
eNB4	2	-30	14.9	0.3	4.47	0.4	0.6	0.24	3.5	3.5	6.8	7	0.3	6.19
eNB5	2	-30	12.5	0.3	3.75	0.4	0.6	0.24	3.5	3.5	6.8	7	0.3	6.91
eNB6	2	-30	14.5	0.3	4.35	0.4	0.6	0.24	3.5	3.5	6.8	7	0.3	6.31
eNB7	2	-30	18.6	0.3	5.58	0.4	0.6	0.24	3.5	3.5	6.8	7	0.3	5.08
eNB8	2	-30	28.5	0.3	8.55	0.4	0.6	0.24	3.5	3.5	6.8	7	0.3	2.11
eNB9	2	-30	10.8	0.3	3.24	0.4	0.6	0.24	3.5	3.5	6.8	7	0.3	7.42
eNB10	2	-30	19.1	0.3	5.73	0.4	0.6	0.24	3.5	3.5	6.8	7	0.3	4.93
eNB11	2	-30	10.7	0.3	3.21	0.4	0.6	0.24	3.5	3.5	6.8	7	0.3	7.45
eNB12	2	-30	12.1	0.3	3.63	0.4	0.6	0.24	3.5	3.5	6.8	7	0.3	7.03
eNB13	2	-30	11.3	0.3	3.39	0.4	0.6	0.24	3.5	3.5	6.8	7	0.3	7.27
eNB14	2	-30	11.9	0.3	3.57	0.4	0.6	0.24	3.5	3.5	6.8	7	0.3	7.09
eNB15	2	-30	16.9	0.3	5.07	0.4	0.6	0.24	3.5	3.5	6.8	7	0.3	5.59
eNB16	2	-30	9.8	0.3	2.94	0.4	0.6	0.24	3.5	3.5	6.8	7	0.3	7.72
eNB17	2	-30	23.8	0.3	7.14	0.4	0.6	0.24	3.5	3.5	6.8	7	0.3	3.52
eNB18	2	-30	12.9	0.3	3.87	0.4	0.6	0.24	3.5	3.5	6.8	7	0.3	6.79
eNB19	2	-30	10.8	0.3	3.24	0.4	0.6	0.24	3.5	3.5	6.8	7	0.3	7.42
eNB20	2	-30	9.6	0.3	2.88	0.4	0.6	0.24	3.5	3.5	6.8	7	0.3	7.78
eNB21	2	-30	8.6	0.3	2.58	0.4	0.6	0.24	3.5	3.5	6.8	7	0.3	8.08
eNB22	2	-30	11.9	0.3	3.57	0.4	0.6	0.24	3.5	3.5	6.8	7	0.3	7.09
eNB23	2	-30	13.7	0.3	4.11	0.4	0.6	0.24	3.5	3.5	6.8	7	0.3	6.55
eNB24	2	-30	21.3	0.3	6.39	0.4	0.6	0.24	3.5	3.5	6.8	7	0.3	4.27
eNB25	2	-30	8.8	0.3	2.64	0.4	0.6	0.24	3.5	3.5	6.8	7	0.3	8.02
eNB26	2	-30	12.6	0.3	3.78	0.4	0.6	0.24	3.5	3.5	6.8	7	0.3	6.88
eNB27	2	-30	9.6	0.3	2.88	0.4	0.6	0.24	3.5	3.5	6.8	7	0.3	7.78
eNB28	2	-30	16	0.3	4.8	0.4	0.6	0.24	3.5	3.5	6.8	7	0.3	5.86
eNB29	2	-30	28.3	0.3	8.49	0.4	0.6	0.24	3.5	3.5	6.8	7	0.3	2.17
eNB30	2	-30	28.9	0.3	8.67	0.4	0.6	0.24	3.5	3.5	6.8	7	0.3	1.99
eNB31	2	-30	21.8	0.3	6.54	0.4	0.6	0.24	3.5	3.5	6.8	7	0.3	4.12
eNB32	2	-30	25.2	0.3	7.56	0.4	0.6	0.24	3.5	3.5	6.8	7	0.3	3.1
eNB33	2	-30	5.35	0.3	1.605	0.4	0.6	0.24	3.5	3.5	6.8	7	0.3	9.055
eNB34	2	-30	7.4	0.3	2.22	0.4	0.6	0.24	3.5	3.5	6.8	7	0.3	8.44
eNB35	2	-30	19.1	0.3	5.73	0.4	0.6	0.24	3.5	3.5	6.8	7	0.3	4.93
eNB36	2	-30	13.1	0.3	3.93	0.4	0.6	0.24	3.5	3.5	6.8	7	0.3	6.73
eNB37	2	-30	13.5	0.3	4.05	0.4	0.6	0.24	3.5	3.5	6.8	7	0.3	6.61
eNB38	2	-30	7.9	0.3	2.37	0.4	0.6	0.24	3.5	3.5	6.8	7	0.3	8.29
eNB39	2	-30	13.9	0.3	4.17	0.4	0.6	0.24	3.5	3.5	6.8	7	0.3	6.49
eNB40	2	-30	12.6	0.3	3.78	0.4	0.6	0.24	3.5	3.5	6.8	7	0.3	6.88

eNB41	2	-30	11.7	0.3	3.51	0.4	0.6	0.24	3.5	3.5	6.8	7	0.3	7.15
eNB42	2	-30	7	0.3	2.1	0.4	0.6	0.24	3.5	3.5	6.8	7	0.3	8.56
eNB43	2	-30	22.6	0.3	6.78	0.4	0.6	0.24	3.5	3.5	6.8	7	0.3	3.88
eNB44	2	-30	10.6	0.3	3.18	0.4	0.6	0.24	3.5	3.5	6.8	7	0.3	7.48
eNB45	2	-30	15	0.3	4.5	0.4	0.6	0.24	3.5	3.5	6.8	7	0.3	6.16
eNB46	2	-30	21.8	0.3	6.54	0.4	0.6	0.24	3.5	3.5	6.8	7	0.3	4.12
eNB47	2	-30	23.3	0.3	6.99	0.4	0.6	0.24	3.5	3.5	6.8	7	0.3	3.67
eNB48	2	-30	16.8	0.3	5.04	0.4	0.6	0.24	3.5	3.5	6.8	7	0.3	5.62
eNB49	2	-30	9.2	0.3	2.76	0.4	0.6	0.24	3.5	3.5	6.8	7	0.3	7.9
eNB50	2	-30	10.3	0.3	3.09	0.4	0.6	0.24	3.5	3.5	6.8	7	0.3	7.57
eNB51	2	-30	14.3	0.3	4.29	0.4	0.6	0.24	3.5	3.5	6.8	7	0.3	6.37
eNB52	2	-30	9	0.3	2.7	0.4	0.6	0.24	3.5	3.5	6.8	7	0.3	7.96
eNB53	2	-30	8.6	0.3	2.58	0.4	0.6	0.24	3.5	3.5	6.8	7	0.3	8.08
eNB54	2	-30	30.2	0.3	9.06	0.4	0.6	0.24	3.5	3.5	6.8	7	0.3	1.6
eNB55	2	-30	11	0.3	3.3	0.4	0.6	0.24	3.5	3.5	6.8	7	0.3	7.36
eNB56	2	-30	11.9	0.3	3.57	0.4	0.6	0.24	3.5	3.5	6.8	7	0.3	7.09
eNB57	2	-30	14.6	0.3	4.38	0.4	0.6	0.24	3.5	3.5	6.8	7	0.3	6.28
eNB58	2	-30	10.9	0.3	3.27	0.4	0.6	0.24	3.5	3.5	6.8	7	0.3	7.39
eNB59	2	-30	6.6	0.3	1.98	0.4	0.6	0.24	3.5	3.5	6.8	7	0.3	8.68

2 RESULTS AND DISCUSSION

2.1 Downstream Power Budget Analysis

The margin is adjusted individually in each instance to uphold consistent loss levels across the entire range of OLT – ONU pairs. This adjustment is essential for maintaining a uniform ONU Tx for each pair. The margin values span a range from 1.60 dB to 9.055 dB.

(i) OLT Tx for all the eNBs has value of 3dBm

(ii) Receiver sensitivity for all the 59 eNBs in the network is -29dBm

(iii) Attenuation coefficient in downstream is 0.25dB/km

(iv) DCF attenuation coefficient is 0.6dB/km

(v) OLT – eNB1 pair has fibre length of 6.2km

(vi) OLT – eNB1 pair has fibre attenuation of 1.55dB/km

(vii) OLT – eNB1 pair has dispersion compensation fibre (DCF) of length 0.4km

(viii) OLT – eNB1 pair has DCF attenuation of 0.24dB/km

(ix) WDM mux used has insertion loss of 3.5dB

(x) WDM demux used has insertion loss of 3.5dB

(xi) Losses accrued due to connection is 7dB

(xii) Losses accrued due to spicing is 0.3dB

(xiii) Margin of 9.11dB was used to maintain fixed OLT Tx and ONU Rx.

The same methodology was applied to derive the aforementioned parameters (items i to xiii) for all OLT – ONU pairs within the network. Across all pairs, the margin was employed to ensure a consistent OLT Tx and ONU Rx, despite variations in fibre lengths and attenuations. Figure 4 illustrates a graphical representation of the results obtained from downstream power budget. The result shows fibre lengths, fibre attenuations, and varying margin values for all 59 eNBs serving as ONUs within the network. It is noteworthy that eNBs with longer fibre cable lengths exhibit correspondingly higher levels of fibre attenuation but lower margin values. For instance, eNB54, which boasts the longest fibre cable length of 30.2km, demonstrates a fibre attenuation of 7.55dB and a margin of 3.11dB. Conversely, eNB33, with the shortest fibre cable length of 5.35km, exhibits a fibre attenuation of 1.34dB and a margin of 9.32dB. This pattern is consistent across all 59 eNBs within the network, as evident in Figure 4.

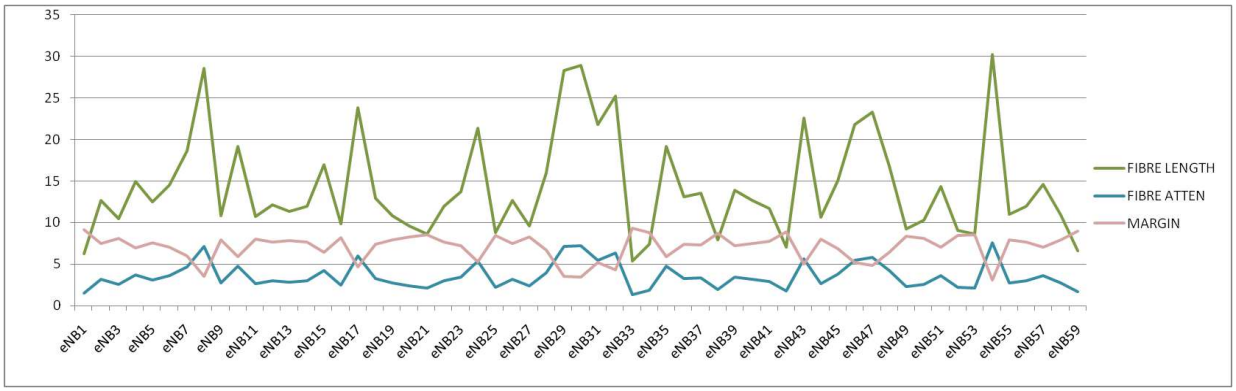

Fig.4: Downstream power budget graphic representation

2.2 Upstream Power Budget Analysis

In the upstream transmission, each eNB transmits data to the OLT located at the exchange/switch, while the OLT, in turn, receives data from each ONU. This section focuses on the findings of the upstream power budget analysis. The calculations in Table 5 were performed using Equation 2. The ONUs are configured with a transmit power of 2dBm, whereas the OLT receiver sensitivity is set at -30dBm. For the ONU1 Tx – OLT Rx pair, the following parameters were determined in accordance with the data provided in Table 5.

(i) All the 59 eNBs (ONU) has transmitter power of value 2dBm

(ii) Receiver sensitivity of the OLT in the network is -30dBm

(iii) Attenuation coefficient in upstream is 0.3dB/km

(iv) DCF attenuation coefficient is 0.6dB/km

(v) OLT – eNB1 pair has fibre length of 6.2km

(vi) OLT – eNB1 pair has fibre attenuation of 1.86dB/km

(vii) OLT – eNB1 pair has dispersion compensation fibre (DCF) of length 0.4km

(viii) OLT – eNB1 pair has DCF attenuation of 0.24dB/km

(ix) WDM mux used has insertion loss of 3.5dB

(x) WDM demux used has insertion loss of 3.5dB

(xi) Losses accrued due to connection is 7dB

(xii) Losses accrued due to spicing is 0.3dB

Margin of 8.8dB was used to maintain fixed OLT Rx and ONU Tx

The same procedure was applied to acquire the aforementioned parameters (items i to xiii) for all ONU – OLT pairs within the network. In all these pairs, a margin was implemented to maintain a consistent ONU Tx and OLT Rx, even when faced with varying fibre lengths and attenuations. Figure 5 illustrates a graphical representation of fibre lengths, fibre attenuations, and the varying margin values for all 59 eNBs serving as ONUs in the network. It is evident that eNBs with longer fibre cable lengths exhibit correspondingly higher levels of fibre attenuation but lower margin values. For instance, eNB54, which features the lengthiest fibre cable at 30.2km, displays a fibre attenuation of 9.06dB and a margin of 1.6dB. On the other hand, eNB33 with the shortest fibre cable length of 5.35km, demonstrates a fibre attenuation of 1.61dB and a margin of 9.06dB. This consistent pattern is observable across all 59 eNBs within the network, as depicted in Figure 5.

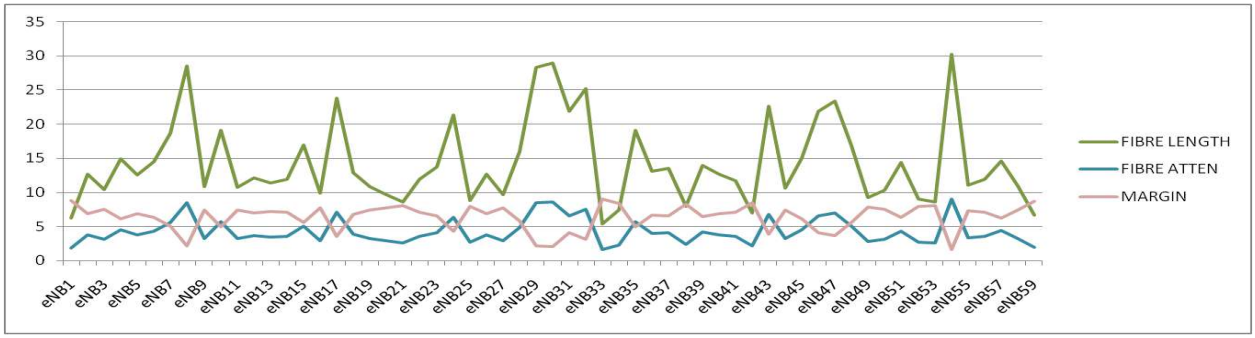

Fig.5: upstream power budget graph

III. CONCLUSION

This study focuses on attaining optimal power budget analysis for Passive Optical Networks (PON) utilized as backhaul deployment for mobile communication network. It achieves its cost-effectiveness because optimal splitter location was chosen by utilizing the coordinates obtained via computational optimal splitter coordinates from research carried out in [7]. The primary objective of this study is to establish an efficient power budgeting approach for PONs, taking into consideration the locations of eNodeBs of the mobile operator (SMILE). The research is conducted within the geographical area of Port-Harcourt city, located in Rivers State, Nigeria.

The investigation incorporates the coordinates of 60 SMILE eNBs to calculate the respective distances between the eNBs and the splitter. An algorithmic model in [7] was employed to determine the optimal location for the splitter, minimizing the distance between the splitter and the 60 eNBs. This approach is referred to as the automatic/systematic method. Power bedget calculation was carried out using spreadsheet for all eNBs. It was evident that eNBs with longer fibre cable lengths exhibit correspondingly higher levels of fibre attenuation but lower margin values. This consistent pattern was observed across all 59 eNBs within the network for both Upstream and Downstream transmissions. The Power Budget achieved in this research ensured that attenuation was greatly reduced and significant receiver sensitivity was achieved.

REFERENCES

[1] ADC (2006), GPON Migration (103132AE), Ensuring my Network is Ready to Migrate to GPON.
[2] Calix (2016), FTTP design Strategies, https://www.iowaheartlandscte.org/.../2016_october_fttp_design_strategies_bret2.pdf
[3] Peter B, (2010), Optical and Broadband Networks, Module POO336 lecture note, Oxford Brookes University.
[4] Neca (2016), National Electrical Contractors Association, USA https://www.stl.tech/.../optical-fibre/.../Field_Test_Procedure_for_Optical_Fibre_Link
[5] Transition networks (2003), (Fibre Optics Basics) www.synginc.com/docs/Fiber_Optics.pdf
[6] (Wikipedia, n.d), https://en.wikipedia.org/wiki/4G
[7] R.O Okeke and V.E Idigo (2021), Computational Analysis of Optimal Splitter Coordinates for Passive Optical Network (PON) Deployment. Volume 16, Issue 2, Ser. I (Mar - Apr 2021), PP 27-40.
[8] R.O Okeke et al (2021), Passive Optical Network: A Fibre to the 'X' Approach: EJERS, European Journal of Engineering and Technology Research Vol. 6, No. 3, April 2021

International Journal of Advanced Engineering Research and Science (IJAERS)
Peer-Reviewed Journal
ISSN: 2349-6495(P) | 2456-1908(O)
Vol-11, Issue-2; Feb, 2024
Journal Home Page Available: https://ijaers.com/
Article DOI: https://dx.doi.org/10.22161/ijaers.112.6

Applying Weighted Taylor Series on Time Series Water Wave Modeling

Syawaluddin Hutahaean

Ocean Engineering Program, Faculty of Civil and Environmental Engineering,-Bandung Institute of Technology (ITB), Bandung 40132, Indonesia

Received: 22 Dec 2023,

Receive in revised form: 30 Jan 2024,

Accepted: 15 Feb 2024,

Available online: 26 Feb 2024

Keywords*— *weighted Taylor series, time series water wave model.

***Abstract*—** *This study develops a time series model for water waves using a weighted Taylor series approach to analyze water wave dynamics. The model incorporates the continuity equation, Euler's momentum conservation equation, and the Kinematic Free Surface Boundary Condition, all formulated through the weighted Taylor series. By integrating the modified continuity equation across the water depth, utilizing depth-averaged velocity concepts, we derive the water surface elevation equation. Similarly, applying the Euler momentum conservation principle to the water surface yields an equation for the horizontal water particle velocity, which is subsequently converted into an expression for the horizontal depth-averaged velocity. The equations for water surface elevation and horizontal water particle velocity are solved using numerical methods. The application of the numerical model results in the generation of four distinct wave profiles: sinusoidal, Stokes, cnoidal, and solitary wave profiles, classified according to Wilson's (1963) criteria. The emergence of each wave profile type is influenced by the specified input wave height.*

I. INTRODUCTION

The Boussinesq equation, a cornerstone in the time series water wave model, has been developed in various forms by numerous researchers, including Boussinesq (1871), Dingermans (1997), Hamm, Madsen, and Peregrine (1993), Johnson (1997), Kirby (2003), and both the 1967 and 1972 works of Peregrine, among others. These versions encompass both the continuity and the water surface equations, as well as the water particle velocity equation. Each variant of the Boussinesq equation stems from the foundational principles of the continuity equation and Euler's momentum conservation equation, albeit with unique interpretations that lend each version its distinctive characteristics.

In our research, we developed a time series model that refines the basic hydrodynamic equations—the continuity equation and Euler's momentum conservation equation—through a weighted Taylor series approach. This method significantly minimizes, if not entirely eliminates, the truncation error typically associated with Taylor series approximations.

We derived the water surface elevation equation by integrating the continuity equation across the water depth, utilizing the concept of depth-averaged velocity. This integration employs the velocity potential equation from the solution to the Laplace equation for water particle velocity, ensuring precision in the integration process.

Furthermore, the horizontal water particle velocity equation was formulated by applying Euler's momentum conservation principle at the water surface. This equation was then converted into a horizontal depth-averaged velocity equation, leveraging the horizontal water particle equation from the velocity potential solution of the Laplace equation, thereby achieving exact transformation.

The core equations of our study—the surface water elevation equation and the horizontal depth-averaged water particle velocity equation—were solved numerically. The spatial differential was tackled using the Finite Difference Method, while the time differential was addressed through the predictor-corrector method. Both methods are characterized by second-order Taylor series accuracy, contingent upon the selection of an appropriately small grid size and time step to ensure the Taylor series is truncated to second-order differentials only. Our research calculated the grid size and time step to maintain the Taylor series truncation to first-order, aligning with the accuracy requirements of the Finite Difference Method.

Meticulous formulation of the basic hydrodynamic equations, governing equations, and numerical solutions, all executed with high precision will generate more reliable and accurate results.

II. WEIGHTED TAYLOR SERIES

Weighted Taylor series is a Taylor series that is truncated to only a first-order series, where the contribution of higher-order terms is expressed with coefficients called weighting coefficients (Hutahaean (2023a)).

For functions with two variables $f = f(x,t)$

$$f(x+\delta x, t+\delta t) = f(x,t) + \gamma_{t,2}\delta t \frac{\partial f}{\partial t} + \gamma_x \delta x \frac{\partial f}{\partial x} \quad \text{.....(1)}$$

$\gamma_{t,2}$ and γ_x are weighting coefficients.

For function $f = f(x,z,t)$ the weighted Taylor series is

$$f(x+\delta x, z+\delta z, t+\delta t) = f(x,z,t) + \gamma_{t,3}\delta t \frac{\partial f}{\partial t} + \gamma_x \delta x \frac{\partial f}{\partial x} + \gamma_z \delta z \frac{\partial f}{\partial z} \quad \text{.....(2)}$$

$\gamma_{t,3}$, γ_x and γ_z are weighting coefficients. There is no difference between γ_x in $f(x,t)$ and $\gamma_x$in f$((x,z,t)$. The basic values of the weighting coefficient are,

$\gamma_{t,2} = 2$; $\gamma_{t,3} = 3$; $\gamma_x = 1$; $\gamma_z = 1$

The foundational values in our model are obtained by eliminating higher-order even differential terms using the central difference method, a technique detailed by Hutahaean (2003a). The adjustments to weighting coefficients, addressing odd higher-order differential terms, are outlined in Table 1, where these coefficients are defined in relation to the optimization coefficient, ε. This relationship indicates that an increase in ε directly amplifies the impact of higher-order Taylor series terms on the analysis. Although the methodology for determining these coefficients is elaborated in Hutahaean (2023a), it is important to emphasize that the accuracy of the coefficients listed in Table 1 significantly exceeds those previously reported by Hutahaean (2023a), reflecting advancements in the precision of incorporating higher-order differential terms to enhance the model's predictive accuracy and reliability in hydrodynamic evaluations.

Table (1) Weighting coefficients.

ε	$\gamma_{t,2}$	$\gamma_{t,3}$	γ_x	γ_z
0.010	1.9998	3.0049	0.9988	1.0115
0.020	1.9992	3.0210	0.9951	1.0490
0.022	1.9990	3.0257	0.9941	1.0602
0.024	1.9988	3.0310	0.9930	1.0726
0.026	1.9986	3.0368	0.9918	1.0866
0.028	1.9984	3.0433	0.9904	1.1020
0.030	1.9981	3.0503	0.9890	1.1189
0.032	1.9979	3.0581	0.9875	1.1375
0.034	1.9976	3.0664	0.9858	1.1577
0.036	1.9973	3.0754	0.9841	1.1798
0.038	1.9970	3.0851	0.9823	1.2037
0.040	1.9966	3.0955	0.9803	1.2296

ε is the optimization coefficient, where in this time series model the selection of the weighting coefficient is determined by the wave amplitude the greater the wave amplitude the greater the ε, which is in the range of $0.015 < \varepsilon < 0.035$.

III. DEPTH INTEGRATION AND TRANSFORMATION COEFFICIENT

The formulation of the water surface equation is done by integrating the continuity equation with respect to water depth. The integration is carried out using the concept of depth average velocity (Dean (1991)) as follows.

$$U = \frac{1}{\beta_u D}\int_{-h}^{\eta} u\, dz \quad \text{.....(3)}$$

$U = U(x, z_0, t)$ is the horizontal particle depth average velocity, Fig (1)

z_0 is the elevation of U towards still water level.

$u = u(x,z,t)$ is the horizontal water particle velocity

β_u is integration coefficient

D is total water depth, $D = h + \eta$

h is water depth towards still water level

η is surface water elevation towards still water level

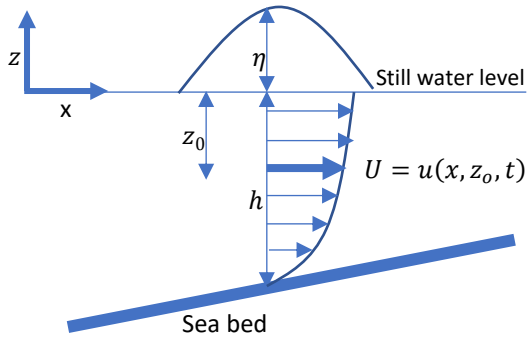

Fig (1). Depth average velocity concept

a. Integration coefficient β_u

In this study, a method for calculating the integration coefficient β_u was developed using the velocity potential equation and by establishing that the depth average velocity is $U = u(x, z_0, t)$, where the value of z_0 is determined (see Fig (1)).

Velocity potential solution of Laplace equation, at the characteristic point where $\cos kx = \sin kx$ (Hutahaean (2023b)) is,

$\phi(x, z, t) = 2G \cos kx \cosh k(h + z) \sin \sigma t$

$\phi(x, z, t)$ is potential velocity

G is wave constants

k is wave number

h is water depth towards still water level

σ is angular frequency

The horizontal velocity equation $u(x, z, t)$ is obtained using the velocity potential property:

$$u(x, z, t) = -\frac{\partial \phi}{\partial x}$$

$$u(x, z, t) = 2Gk \cos kx \cosh k(h + z) \sin \sigma t \quad \text{.....(4)}$$

It has been defined that the horizontal depth average velocity is the velocity at $z = z_0$ (Fig (1)), where z_0 is determined, then

$$U(x, z_0, t) = 2Gk \cos kx \cosh k(h + z_0) \sin \sigma t \quad \text{....(5)}$$

Employing (4) and (5),

$$\frac{u(x,z,t)}{U(x,z_0,t)} = \frac{\cosh k(h+z)}{\cosh k(h+z_0)} \quad \text{……(6)}$$

Equation (3) is written into the equation for the integration coefficient β_u,

$$\beta_u = \frac{1}{UD} \int_{-h}^{\eta} u \, dz$$

$$\beta_u = \frac{1}{D \cosh k(h + z_0)} \int_{-h}^{\eta} \cosh k(h + z) \, dz$$

Integration is completed,

$$\beta_u = \frac{\sinh k(h + \eta)}{kD \cosh k(h + z_0)}$$

$\eta = \frac{A}{2}$, A is wave amplitude, therefore

$$D = h + \frac{A}{2}$$

$$\beta_u = \frac{\sinh kD}{kD \cosh k(h + z_0)}$$

Hutahaean (2024) found that $kD = \theta\pi$ where $\tanh kD = \tanh \theta\pi \approx 1$, θ is the deep water coefficient, in this time series model research used $\theta = 1.80$. Determined $z_0 = -\xi h$, where $0 < \xi < 1$.. In deep water, $h \approx h + \frac{A}{2}$.

$$\beta_u = \frac{\sinh \theta\pi}{\theta\pi \cosh(\theta\pi(1-\xi))} \quad \text{……..(7)}$$

b. Transformation Coefficient $\alpha_{u\eta}$

In the process of integrating the continuity equation with respect to depth, there will be a horizontal surface water particle velocity u_η. This velocity must be transformed into the horizontal depth average velocity $U(x, z_0, t)$.

Using (4) and (5),

$$\frac{u_\eta}{U} = \frac{\cosh k\left(h + \frac{A}{2}\right)}{\cosh k(h + z_0)}$$

$$\frac{u_\eta}{U} = \frac{\cosh \theta\pi}{\cosh(\theta\pi(1 - \xi))}$$

Transformation coefficient $\alpha_{u\eta}$ is

$$\alpha_{u\eta} = \frac{\cosh \theta\pi}{\cosh(\theta\pi(1-\xi))} \quad \text{….(8)}$$

$$u_\eta = \alpha_{u\eta} U \quad \text{….(9)}$$

In the formulation of the equation for horizontal depth average velocity, the variable $u_\eta u_\eta$ must be transformed into U.

Using (4),

$u_\eta = 2Gk \cos kx \cosh k(h + \eta) \sin \sigma t$

$u_\eta u_\eta$ is mathematically expressed as

$u_\eta u_\eta = (2Gk \cos kx \cosh k(h + \eta) \sin \sigma t)^2$

However, since $u_\eta u_\eta$ moves simultaneously with u_η where the distribution of $u_\eta u_\eta$ according to space and time is the same as u_η, thus,

$u_\eta u_\eta = (2Gk)^2 \cos kx \cosh k(h + \eta) \sin \sigma t$

$UU = (2Gk)^2 \cos kx \cosh k(h + z_0) \sin \sigma t$

Therefore, the relation between $u_\eta u_\eta$ and UU is

$$u_\eta u_\eta = \alpha_{u\eta} UU \quad \text{……(10)}$$

As an illustration of the values of the integration coefficient β_u and the transformation coefficient $\alpha_{u\eta}$ can be seen in Table (2).

Table (2) The values of β_u and $\alpha_{u\eta}$

ξ	β_u	$\alpha_{u\eta}$
0.10	0.324	1.679
0.15	0.420	2.176
0.20	0.544	2.819
0.25	0.705	3.653

0.30	0.913	4.732
0.35	1.182	6.130
0.4	1.531	7.937

Table (2) shows that larger ξ is followed by deeper z_0, the larger the values of the integration coefficient β_u and the transformation coefficient $\alpha_{u\eta}$. In this study, a value of $\beta_u = 1$ was used, and using the Newton-Rhapson method, $\xi = 0.317612$ was obtained with a transformation coefficient value of $\alpha_{u\eta} = 5.183954$.

IV. WATER SURFACE ELEVATION EQUATION

4.1.Weighted continuity equation.

The continuity equation is formulated using the weighted Taylor series and by applying the principle of mass conservation,

$$\gamma_x \frac{\partial u}{\partial x} + \gamma_x \frac{\partial w}{\partial z} = 0 \qquad \ldots\ldots(11)$$

This equation is formulated under the condition that the horizontal particle velocity only changes along the horizontal axis, and similarly, the vertical particle velocity only changes along the vertical axis.

4.2. Integration of continuity equation

To obtain the water surface elevation equation, the continuity equation is integrated with respect to water depth, where the integration of the second term can be directly completed by ignoring the bottom vertical water particle velocity.

$$\int_{-h}^{\eta} \gamma_x \frac{\partial u}{\partial x} dz + \gamma_z w_\eta = 0$$

The vertical surface water particle velocity w_η is substituted with the Kinematic Free Surface Boundary Condition, where the weighted KFSBC (Hutahaean (2023a)) is as follows.

$$w_\eta = \gamma_{t,2} \frac{\partial \eta}{\partial t} + \gamma_x u_\eta \frac{\partial \eta}{\partial x}$$

Substituted into the integration of the continuity equation,

$$\int_{-h}^{\eta} \gamma_x \frac{\partial u}{\partial x} dz + \gamma_z \left(\gamma_{t,2} \frac{\partial \eta}{\partial t} + \gamma_x u_\eta \frac{\partial \eta}{\partial x} \right) = 0$$

The integration of the first term is solved by Leibniz integration (Protter, Murray, Morrey, & Charles, 1985),

$$\int_\alpha^\beta \frac{\partial f}{\partial x} dz = \frac{\partial}{\partial x} \int_\alpha^\beta f \, dz - f_\beta \frac{\partial \beta}{\partial x} + f_\alpha \frac{\partial \alpha}{\partial x} \qquad \ldots\ldots(12)$$

$$\int_{-h}^{\eta} \frac{\partial u}{\partial x} dz = \frac{\partial}{\partial x} \int_{-h}^{\eta} u \, dz - u_\eta \frac{\partial \eta}{\partial x} - u_{-h} \frac{\partial h}{\partial x}$$

The integration of the first term on the right side of the equation is completed using the concept of depth average velocity, and the horizontal bottom water particle velocity is ignored.

$$\int_{-h}^{\eta} \frac{\partial u}{\partial x} dz = \frac{\partial \beta_u UD}{\partial x} - u_\eta \frac{\partial \eta}{\partial x}$$

Substituted into the continuity equation integration, the surface velocity is transformed into depth average velocity, and the equation is written as the water surface equation,

$$\gamma_z \gamma_{t,2} \frac{\partial \eta}{\partial t} = -\gamma_x \beta_u \frac{\partial UD}{\partial x} + \gamma_x (1 - \gamma_z) \alpha_{u\eta} U \frac{\partial \eta}{\partial x}$$

……(13)

(13) is the water surface elevation equation that is used to calculate the water surface elevation.

V. EULER'S MOMENTUM CONSERVATION EQUATION

By using the weighted Taylor series and the same fluid flow conditions as those used in the formulation of the continuity equation, where horizontal water particle velocity only changes along the horizontal axis and vertical water particle velocity only changes along the vertical axis, Euler's momentum conservation equation in the horizontal and vertical directions, respectively are presented as follows.

$$\frac{\partial u}{\partial t} + \gamma_x u \frac{\partial u}{\partial x} = -\frac{1}{\rho} \frac{\partial p}{\partial x} \qquad \ldots\ldots(14)$$

$$\frac{\partial w}{\partial t} + \gamma_z w \frac{\partial w}{\partial z} = -\frac{1}{\rho} \frac{\partial p}{\partial z} - g \qquad \ldots\ldots(15)$$

Equation (15) is written as an equation for pressure p and integrated over water depth and the surface dynamic boundary condition $p_\eta = 0$ is performed

$$\frac{p}{\rho} = \gamma_{t,3} \int_z^\eta \frac{\partial w}{\partial t} dz + \frac{\gamma_z}{2} (w_\eta w_\eta - ww) + g(\eta - z)$$

Differentiated with respect to the x-horizontal axis,

$$\frac{1}{\rho} \frac{\partial p}{\partial x} = \gamma_{t,3} \frac{\partial}{\partial x} \int_z^\eta \frac{\partial w}{\partial t} dz + \frac{\gamma_z}{2} \frac{\partial}{\partial x} (w_\eta w_\eta - ww) + g \frac{\partial \eta}{\partial x}$$

Substituted to (14)

$$\gamma_{t,3} \frac{\partial u}{\partial t} + \frac{\gamma_x}{2} \frac{\partial uu}{\partial x} = -\gamma_{t,3} \frac{\partial}{\partial x} \int_z^\eta \frac{\partial w}{\partial t} dz - \frac{\gamma_z}{2} \frac{\partial}{\partial x} (w_\eta w_\eta - ww) - g \frac{\partial \eta}{\partial x}$$

This equation is worked out on the surface i.e. on $z = \eta$,

$$\gamma_{t,3} \frac{\partial u_\eta}{\partial t} + \frac{\gamma_x}{2} \frac{\partial u_\eta u_\eta}{\partial x} = -g \frac{\partial \eta}{\partial x}$$

The surface velocity is transformed into depth average velocity,

$$\gamma_{t,3} \alpha_{u\eta} \frac{\partial U}{\partial t} + \frac{\gamma_x \alpha_{u\eta}}{2} \frac{\partial UU}{\partial x} = -g \frac{\partial \eta}{\partial x} \qquad \ldots\ldots(16)$$

VI. VERTICAL WATER PARTICLE VELOCITY EQUATION

Both the water surface elevation equation and the horizontal water particle velocity do not include the variable of vertical water particle velocity. However, this velocity can be calculated in a simple manner, using the Kinematic Free Surface Boundary Condition:

$$w_\eta = \gamma_{t,2}\frac{\partial \eta}{\partial t} + u_\eta \frac{\partial \eta}{\partial t}$$

This surface velocity is transformed into depth average velocity.

$$W = \frac{1}{\alpha_{w\eta}}\left(\gamma_{t,2}\frac{\partial \eta}{\partial t} + \alpha_{u\eta} U \frac{\partial \eta}{\partial t}\right) \quad .....(17)$$

Where,

$$\alpha_{w\eta} = \frac{\sinh \theta\pi}{\sinh \theta\pi(1-\xi)} \quad .....(18)$$

Where θ and ξ are presented in Section 3.

VII. NUMERICAL SOLVING

Equations (13) and (16) are solved using numerical methods. The spatial differential is solved with the Finite Difference Method, and the time differential is solved using the predictor-corrector method.

7.1. Calculation of time step δt and grid size δx

Solving differential equations with numerical methods requires a specific time step and grid size to ensure good calculation results. The following section presents the equations for calculating these time steps and grid sizes. In principle, these equations are formulated based on the truncation of the Taylor series, which is the interval size where the Taylor series can be truncated to only a first-order series. The formulation of the equations can be seen in Hutahaean (2023a).

a. Time step δt calculation

Time step δt was measured using the following equation.

$$\frac{2}{3}\pi^2\varepsilon_t^2 - \pi\varepsilon_t + \varepsilon = 0 \quad ....(19)$$

ε is a small number that determines the size of the time step δt for example, $\varepsilon = 0.01$. The smaller the value of ε, the smaller ε_t and the smaller δt, where $\delta t = \varepsilon_t T$, T, with T being the wave period. In that equation, there are two values of ε_t; the smallest value is used.

b. Grid size δx measurement

The calculation of grid size δx requires the input time step δt obtained from (19). The equation to calculate δx is,

$$c_0 + c_1\varepsilon_x + c_2\varepsilon_x^2 = 0 \quad .....(20)$$

$$c_0 = 2\pi\varepsilon_t\varepsilon - 2\pi^2\varepsilon_t^2$$

$$c_1 = 2\pi\varepsilon + 4\pi^2\varepsilon_t$$

$$c_2 = -2\pi^2$$

There are two values of ε_x, the largest is used. Grid size $\delta x = \varepsilon_x L$,, where L is the wave length.

The formulations (19) and (20), with higher accuracy, can be seen in Hutahaean (2023a). However, the dominant factor determining accuracy is the choice of the value of ε. In principle, the smaller the value of ε. the better. In Table (3), the calculation results for δt and δx for waves with a wave period $T = 8.0$ sec, and a wave length $L = 16.0$ m are presented.

Table (3). Time step δt and grid size δx outcomes

ε	ε_t	ε_x	δt (sec.)	δx (m)
0.02	0.0065	0.0192	0.0516	0.3079
0.025	0.0081	0.0241	0.0648	0.3856
0.03	0.0097	0.029	0.078	0.4637
0.035	0.0114	0.0339	0.0913	0.542
0.04	0.0131	0.0388	0.1047	0.6207
0.045	0.0148	0.0437	0.1183	0.6997
0.05	0.0165	0.0487	0.1319	0.7791

As seen in Table (3), the larger the ε, the larger also the δt and δx. To check the compatibility between the time-step δt and the grid size δx, the Courant criterion (1928) is used as follows $\frac{\delta x}{\delta t} = 3\ C$

C adalah wave celerity dimana

$$C = \frac{\sigma}{k} = \frac{L}{T}\ m/sec$$

For example, for waves with a wave period $T = 8\ sec.$, and with a wave length $L = 16.0$ m, $C = 2.0\ m/sec$. The values of $\frac{\delta x/\delta t}{C}$ for δt and δx in Table (3) are calculated, with the calculation results presented in Table (4).

Table (4). Checking the Courant criteria

ε	δt (sec.)	δx (m)	$\delta x/\delta t$ (m/sec)	$\frac{\delta x/\delta t}{C}$
0.02	0.0516	0.3079	5.9639	2.982
0.025	0.0648	0.3856	5.9547	2.9774
0.03	0.078	0.4637	5.9454	2.9727
0.035	0.0913	0.542	5.9361	2.968
0.04	0.1047	0.6207	5.9267	2.9633
0.045	0.1183	0.6997	5.9172	2.9586
0.05	0.1319	0.7791	5.9076	2.9538

In Table (4), it is found that the values of δt and δx meet the Courant criterion, for all values of ε, which is ≈ 3.

Modeling in non-uniform water depths requires a non-uniform grid size as well. This is because different water depths have different wavelengths. In a non-uniform grid size, there is no difference or change in the Courant number.

$$\frac{\delta x}{\delta t} = \frac{\varepsilon_x}{\varepsilon_t}\frac{L}{T} = \frac{\varepsilon_x}{\varepsilon_t}C$$

The Courant number in this case is $\frac{\varepsilon_x}{\varepsilon_t}$. This value is constant for a given accuracy level ε, unaffected by wavelength or wave period. As an example, calculations for a sloping bottom with nonuniform wavelength are presented in Table (5), where a wave period of 8 sec is used, and the grid calculation uses $\varepsilon = 0.02$.

In Table (5), δt is constant, while δt is not, but the resulting Courant number,
is constant.

$$\frac{\delta x/\delta t}{C} = \frac{\varepsilon_x}{\varepsilon_t}$$

Table (5) Grid-size of non uniform water depth

L (m)	δt (sec.)	δx (m)	$\delta x/\delta t$ (m/sec)	$\frac{\delta x/\delta t}{C}$
16	0.05163	0.3079	5.9639	2.98195
14	0.05163	0.26941	5.21842	2.98195
12	0.05163	0.23093	4.47293	2.98195
10	0.05163	0.19244	3.72744	2.98195
8	0.05163	0.15395	2.98195	2.98195
6	0.05163	0.11546	2.23646	2.98195
4	0.05163	0.07698	1.49098	2.98195
2	0.05163	0.03849	0.74549	2.98195

The Finite Difference Method is formulated using a second-order Taylor series, where the Taylor series is truncated to second order only. Therefore, calculations with this method require small time steps and grid sizes. The time step and grid size calculated for the truncation of the first-order Taylor series definitely meet the requirements for the truncation of the second-order Taylor series.

c. Wave length measurement

For calculating grid size, information about the wave length is required. The following section discusses the method for calculating wave length.

The deep-water wave number is calculated using the equation,

$$\frac{gA_0}{2}k_0^2 - \frac{g\tanh(\theta\pi)}{\sqrt{\gamma_z}}k_0 + \gamma_{t,2}\gamma_{t,3}\sigma^2 = 0 \qquad \text{.....(21)}$$

g gravitational acceleration
A_0 deep water wave amplitude
$\sigma = \frac{2\pi}{T}$, T adalah wave period.
Deep water depth,

$$h_0 = \frac{\theta\pi}{k_0} - \frac{A_0}{2} \qquad \text{.....(22)}$$

Wave number of one water depth $h_x < h_0$,

$$k_x = \frac{k_0 h_0}{h_x}$$

Where wave length

$$L_x = \frac{2\pi}{k_x}$$

To conform to the wavelength model, in (21) the weighting coefficients are used: $\gamma_{t,2} = 1.8$, $\gamma_{t,2} = 2.6$, $\gamma_x = 1.0$ dan $\gamma_z = 1.0$.

7.2.Predictor-corrector method

When performing calculations with the finite difference method, a grid-points is established within the domain, using the grid size as previously discussed. At a given point i on the grid, the water surface elevation equation and horizontal water particle velocity can be rewritten as follows:

$$\frac{\partial \eta_i}{\partial t} = F_i(t)$$
$$\frac{\partial U_i}{\partial t} = G_i(t)$$

a. Predictor

The steps of predictor method requires the use of central difference method,

$$\eta_{i,pred}^{t+\delta t} = \eta_i^{t-\delta t} + 2\delta t F_i^t$$

After all $\eta_{i,pred}^{t+\delta t}$ values are obtained, the predictor step for water particle velocity is performed,

$$U_{i,pred}^{t+\delta t} = U_i^{t-\delta t} + 2\delta t G_i^t$$

After all the values of $\eta_{i,pred}^{t+\delta t}$ dan $U_{i,pred}^{t+\delta t}$ are obtained, the corrector step is performed.

b. Corrector

Corrector is done by using numerical integration of Newton-Cote with 3 integration points (Arden, Bruce W. and Astill Kenneth N. ,1970), as follows.

$$\int_{t-\delta t}^{t+\delta t} f(t)\,dt = \delta t\left(\frac{1}{3}f^{t-\delta t} + \frac{4}{3}f^{t} + \frac{1}{3}f^{t+\delta t}\right)$$

The three-point numerical integration is formulated using a three-point Lagrange polynomial that has an accuracy

equivalent to a second-order Taylor series. The time step calculated by (19) satisfies the time step requirement where the Taylor series can be truncated to second order.

Where $\eta_{i,pred}^{t+\delta t}$ dan $U_{i,pred}^{t+\delta t}$ dihitung $F_{i,pred}^{t+\delta t}$

$$\eta_{i,cor}^{t+\delta t} = \eta_i^{t-\delta t} + \delta t\left(\frac{1}{3}F_i^{t-\delta t} + \frac{4}{3}F_i^{t} + \frac{1}{3}F_{i,pred}^{t+\delta t}\right)$$

After all the $\eta_{i,cor}^{t+\delta t}$ values are obtained, the corrector step for the water particle velocity is performed,

$$U_{i,cor}^{t+\delta t} = U_i^{t-\delta t} + \delta t\left(\frac{1}{3}G_i^{t-\delta t} + \frac{4}{3}G_i^{t} + \frac{1}{3}G_{i,pred}^{t+\delta t}\right)$$

After all values of $\eta_{i,cor}^{t+\delta t}$ dan $U_{i,cor}^{t+\delta t}$) are obtained, convergence is checked, $\left|\eta_{i,cor}^{t+\delta t} - \eta_{i,pred}^{t+\delta t}\right| < \mu$, for all points, μ being a small number. If the convergence condition is not met, the result of the corrector step becomes the predictor result, $\eta_{i,pred}^{t+\delta t} = \eta_{i,cor}^{t+\delta t}$ and $U_{i,pred}^{t+\delta t} = U_{i,cor}^{t+\delta t}$, , and the corrector step is repeated. Generally, convergence is achieved in 3 replications

VIII. MODEL OUTCOME

An assessment or evaluation of the modelled results was carried out by comparing the modelled wave profiles with the wave profiles from Wilson (1963).

8.1. Wave profile based on Wilson's criteria (1963).

The grouping of water wave profiles according to Wilson (1963) is presented in Table (6), with the profile sketched in Fig (2).

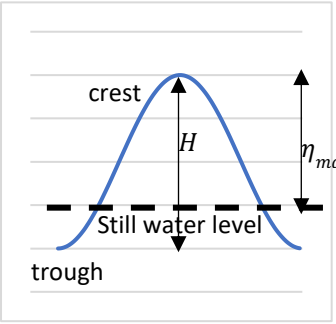

Fig (2). Wave profile based on Wilson (1963) criteria.

Table (6) Water wave profile criteria (Wilson (1963)))

Wave type	$\frac{\eta_{max}}{H}$
Airy/sinusoidal waves	< 0.505
Stoke's waves	$0.505 - 0.635$
Cnoidal waves	$0.635 - 1$
Solitary waves	$= 1$

a. Airy's Profile

The Airy wave profile is marked by its symmetrical nature, with the wave crest and trough being mirror images of each other, allowing for the wave height (H) to be approximately twice the wave amplitude (A), or $H \approx 2A$. This sinusoidal wave theory, also referred to as Airy wave theory or small amplitude wave theory, was pioneered by Airy in 1841. True to its designation, the theory is specifically tailored for waves of very small amplitudes, providing a foundational understanding of wave dynamics within this limited scope.

b. Stoke's Profile

Stokes wave theory, introduced by George Stokes in 1847, represents an advancement beyond the sinusoidal or Airy wave theory, earning it the alternative name of Finite Amplitude Wave Theory. This theory addresses some of the limitations of the Airy wave theory by accounting for waves with larger amplitudes. The distinguishing feature of the Stoke's wave profile is its asymmetry: the wave crests are sharper or steeper compared to the more gently sloped wave troughs, and it's possible for the wave profile to exhibit two distinct crests.

c. Cnoidal wave profile

The cnoidal wave theory was initially formulated by Korteweg and de Vries in 1895, upon observing the wave profile within a canal, thereby confirming its presence in natural settings. This particular wave profile is characterized by a significant disparity between the crest and the trough. Predominantly, the wave's surface is elevated above the level of still water, presenting a steep profile, whereas only a minor segment falls below, exhibiting a more gradual profile.

d. Solitary wave profile

In the case of a solitary wave profile, the entire surface of the wave remains above the level of still water. This type of wave was first identified by John Scott Russell in 1844 after he observed the phenomenon in a laboratory setting. The analytical foundation for understanding solitary waves was later established by Joseph Boussinesq in 1871. Hence, like the cnoidal wave, the solitary wave profile is also observed in natural environments.

8.2. Modeled wave profile in deep water.

The model operated at a constant water depth of $h = 30\ m$. At $x = 0$, a sinusoidal wave is introduced using the equation $\eta(0,t) = A\sin\sigma t$, where the wave period $T = 8\ sec$. This input is applied for the duration of one wave period only. The wave's amplitude is selected to match the desired wave profile. Calculations for determining the deep water depth h_0, using equations (21) and (22), categorize the 30 m water depth as deep water, as indicated in Table (7).

In the wavelength calculation results presented in Table (7), an inverse relationship is observed between wave amplitude and wavelength: as the wave amplitude

increases, the wavelength decreases. This trend contrasts with the findings.

from the numerical model, where an increase in wave amplitude results in a slightly longer wavelength. It is important to note, however, that the water depth of 30 m exceeds h_0 and thus falls into the category of deep water.

Table (7). Deep water depth h_0 measurement

A (m)	L_0 (m)	h_0 (m)
0.02	21.288	19.149
0.5	19.643	17.429
1.3	15.849	13.614

For the execution of this numerical model, a deep water coefficient $\theta = 1.8$. is employed. Additionally, a range for the weighting coefficient $\varepsilon = 0.015 - 0.035$ is used, where a larger wave amplitude corresponds to a higher value of ε the weighting coefficients are detailed in Table (1). The model runs over eight wave periods, equivalent to 80 seconds. During the initial two wave periods, the wave profile undergoes an evolution, rendering it unstable. From the third wave period onward, the wave profile achieves stability.

a. Sinusoidal profile

With input wave amplitude $A = 0.02\ m$, $\frac{\eta_{max}}{H} = \frac{0.02}{0.04} = 0.5$ is obtained (Fig(3)). This condition corresponds to Wilson's criterion for sinusoidal wave profile.

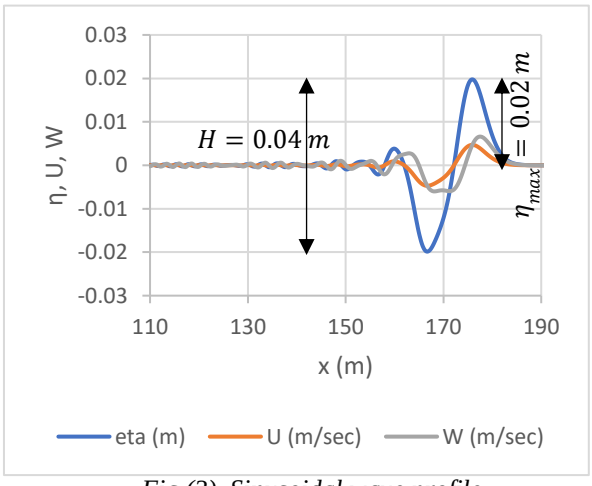

Fig (3). Sinusoidal wave profile

b. Stoke's wave Profile

Stoke's profile, obtained using $A = 0.5\ m$. The modelled results can be seen in Fig (4). $\frac{\eta_{max}}{H} = \frac{0.605}{1.0} = 0.605$ is obtained, this condition is in accordance with Wilson's criteria for Stoke's wave profile.

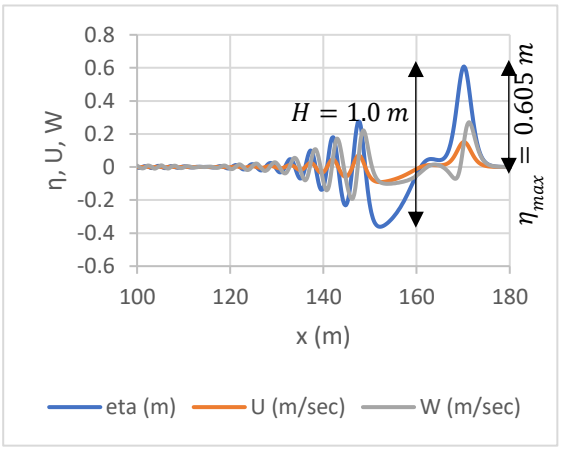

Fig (4). Stoke's profile

c. Cnoidal wave Profile

The model was executed with an input of $A = 1.30\ m$, or $H = 2.60$ m. This is the largest wave height for a wave period of 8 sec. $\frac{\eta_{max}}{H} = \frac{2.1}{2.6} = 0.808$ was obtained, in accordance with Wilson's criteria, for a Cnoidal profile. The image of this cnoidal profile is presented in Fig (5).

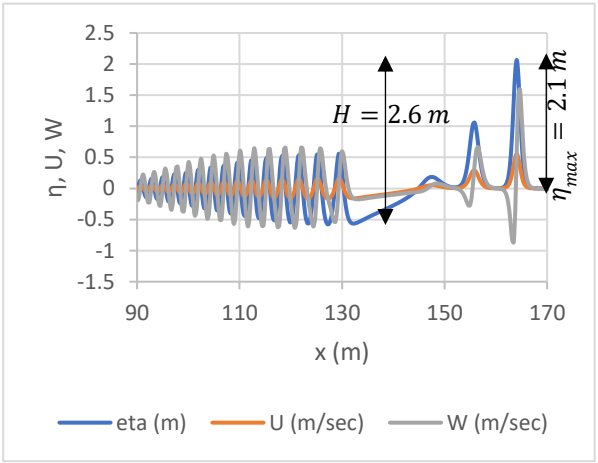

Fig (5). Cnoidal profile

In this section, it was found that the model execution in deep water did not obtain a solitary wave profile, even though the maximum wave amplitude was used.

8.3. The Effect of water depth on wave profile.

In this section, the effect of water depth on wave profiles is explored using a model that simulates a sinusoidal wave input at $x = 0.0$ expressed as $\eta(0,t) = A \sin \sigma t$, which is applied for the duration of a single wave period of 12.0 seconds. The model uses a wave amplitude of 2.0 meters, equivalent to a wave height $H = 4.0\ m$. For this scenario, the deep water depth h_0 is calculated to be 41.0 meters. The experiment is conducted at water depths of 41.0 meters, 20 meters, and 8.0 meters to observe the resulting wave profiles. At the depth of 41.0 meters, matching the deep water depth h_0, the model produces a Stoke's wave profile,

depicted in Fig (6). When executed at a water depth of 20 meters, the model forms a cnoidal wave profile, as shown in Fig (7) and in a water depth 8.0 m, solitary wave profile was obtained (Fig.(8)).

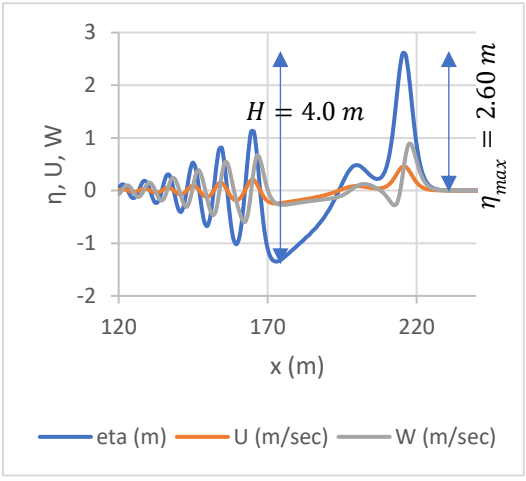

Fig (6).Stoke's profile $\frac{\eta_{max}}{H} = 0.6$

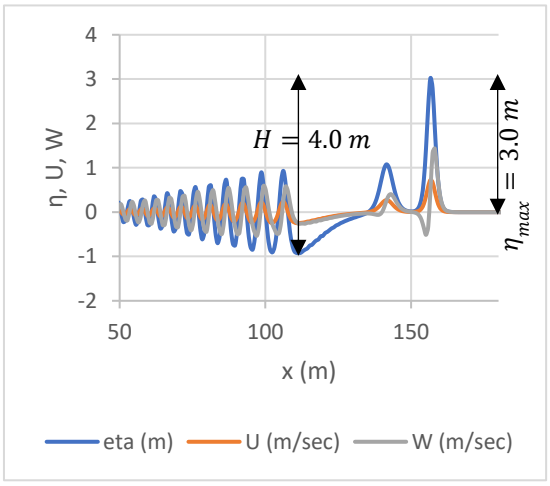

Fig (7).Cnoidal profile $\frac{\eta_{max}}{H} = 0.75$

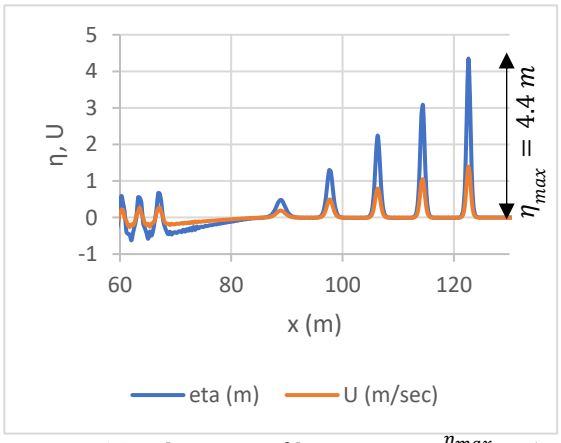

Fig (8).Solitairy profile $\eta_{max} = H, \frac{\eta_{max}}{H} = 1$

In the observed solitary wave profile, an increase in wave height is noted, from the initial 4.0 meters (input) to 4.40 meters. This increase is believed to be a result of the wave setup phenomenon, which is characteristic of shallow water effects. According to Wilson's criterion for solitary waves, the ratio of the maximum wave height $\frac{\eta_{max}}{H} = 1$. However, the wave trough is not considered in this analysis due to its minimal size and the presence of numerous other wave crests.

8.4. Model execution at the sloping bottom.

In a subsequent experiment, the model is applied to a canal featuring an upstream water depth of 15.0 meters and a downstream depth of 5.0 meters, with the channel extending over a length of 200.0 meters. The input for this setup is a sinusoidal wave characterized by a wave period of 8.0 seconds and a wave amplitude of 0.50 meters. The outcomes of this experiment are depicted in Fig (9), illustrating that at a water depth of 6.0 meters, the wave undergoes shoaling, which results in the wave height increasing to 1.40 meters and the wave adopting a solitary profile.

The results from executing the model reveal its capability to simulate various wave profiles, including sinusoidal, Stoke's, cnoidal, and solitary profiles. Importantly, the formation of these profiles is influenced not only by the wave amplitude but also significantly by water depth, particularly in the case of the solitary profile. An amplitude that results in a Stoke's profile in deep water conditions may lead to a cnoidal profile in shallower waters, and similarly, the same amplitude can generate a solitary profile in even shallower depths. This underscores the critical role that both water depth and wavelength play in determining the specific wave profile that emerges.

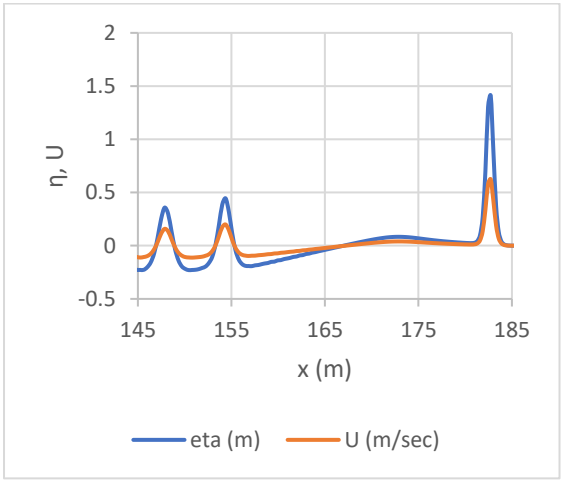

Fig (9). Solitary wave profil due to shoaling.

The occurrence of a solitary profile in shallow water suggests that the model's wavelength is sufficiently short

to facilitate the formation of such a profile. The weighting coefficient emerges as a crucial parameter in shaping the wavelength, indicating that this coefficient, as part of the weighted Taylor series, significantly influences the outcomes of the model. This observation highlights the interconnectedness of wave amplitude, water depth, wavelength, and model parameters like the weighting coefficient in the complex dynamics of wave profile formation.

IX. CONCLUSION

The study reveals that the time series model developed can generate wave profiles aligning with previous research, notably including the cnoidal and solitary wave profiles. This demonstrates the model's capability to effectively simulate water waves.

The solitary wave profile emerges at short wavelengths, where the model's wavelength determination hinges on the weighting coefficients within the weighted Taylor series. This suggests the selected weighting coefficients are well-suited for the task.

Moreover, the model's performance is influenced by the chosen time step and grid size. These parameters are aligned with the foundational hydrodynamics equations' assumptions, which presuppose truncation of the Taylor series to first order. Additionally, the time step and grid size adhere to the Finite Difference Method's requirements, where the Taylor series truncation is limited to the second order, ensuring a comparable level of numerical integration accuracy. The coherence between the time step and grid size also meets Courant's criteria, further validating the model's configuration.

In summary, the employment of a weighted Taylor series to formulate the time series model, coupled with the strategic selection of time step and grid size for numerical solution, leads to robust model outcomes.

REFERENCES

[1] Hutahaean, S. (2023a). Method for Determining Weighting Coefficients in Weighted Taylor Series Applied to Water Wave Modeling. International Journal of Advance Engineering Research and Science (IJAERS). Vol. 10, Issue 12; Dec, 2023, pp 105-114. Article DOI: https://dx.doi..org/10.22161/ijaers.1012.11.

[2] Dean, R.G., Dalrymple, R.A. (1991). Water wave mechanics for engineers and scientists. Advance Series on Ocean Engineering.2. Singapore: World Scientific. ISBN 978-981-02-0420-4. OCLC 22907242.

[3] Arden, Bruce W. and Astill Kenneth N. (1970). Numerical Algorithms : Origins and Applcations. Philippines copyright (1970) by Addison-Wesley Publishing Company, Inc.

[4] Hutahaean, S. (2023b). Water Wave Velocity Potential on Sloping Bottom in Water Wave Transformation Modeling . International Journal of Advance Engineering Research and Science (IJAERS). Vol. 10, Issue 10; Oct, 2023, pp 149-157. Article DOI: https://dx.doi..org/10.22161/ijaers.1010.15.

[5] Hutahaean, S. (2024). Breaking Index Study on Weighted Laplace Equation. International Journal of Advance Engineering Research and Science (IJAERS). Vol. 11, Issue 1; Jan, 2024, pp 34-43. Article DOI: https://dx.doi..org/10.22161/ijaers.11.6.

[6] Protter, Murray, H.; Morrey, Charles, B. Jr. (1985). Differentiation Under The Integral Sign. Intermediate Calculus (second ed.). New York: Springer pp. 421-426. ISBN 978-0-387-96058-6.

[7] Courrant, R., Friedrichs, K., Lewy, H. (1928). Uber die Pertiellen Differenzengleic hungen der mathematiscen Physik. Mathematiscen Annalen (in German). 100 (1);32-74, Bibcode : 1928, MatAn. 100.32.c. doi: 10.1007/BF01448839, JFM 54.0486.01 MR 1512478.

[8] Arden, Bruce W. and Astill Kenneth N. (1970). Numerical Algorithms : Origins and Applcations. Philippines copyright (1970) by Addison-Wesley Publishing Company, Inc.

[9] Wilson, B.W. (1963). Condition of Existence for Types of Tsunami Waves, paper presented at XIIIth Assembly IUGG, Berkeley, California, August 1963 (unpublish).

[10] Airy, G.B. (1841). Tides and waves. In Hughs James Rose: et.al (eds.) Encyclopedia Metropolitana. Mixed Science. Vol.3 (published 1817-1845). Also: Trigonometry, On the Figure of the Earth, Tides and Waves. 396 pp.

[11] Stokes, G.G. (1847). On the Theory of Oscillatory Waves.Trans Camb. Phil.Soc., Vol.8 pp.441-455. Also Math Phys. Papers, Vol. 1, Camb. Univ. Press, 1880.

[12] Korteweg, D.J. and De Vries, J. (1895). On the Change of Form of Longwaves Advancing, in a Rectangular Canal, and on a New Type of Long stationary Waves. Phil.Mag., 5th Series, Vol. 39, pp. 422-443.

[13] Russel, J.S., 1844. Report on Waves. 14th Meeting Brit. Assoc. Adv. Sci., pp. 311-390.

[14] Boussinesq, J. , 1871. Theori de L'intumesence Liquide , Apelee Onde Solitaire ou de Translation se Propageant Dans un Canal Rectangulaire. Comptes Rendus Acad . Sci., Paris, Vol.72, pp.755-759.

International Journal of Advanced Engineering Research and Science (IJAERS)
ISSN: 2349-6495(P) | 2456-1908(O)
Vol-8, Issue-5; May, 2021
Journal Home Page Available: https://ijaers.com/
Journal DOI: 10.22161/ijaers
Article DOI: https://dx.doi.org/10.22161/ijaers.85.X

Design Analysis of an IoT based Early Flood Detection and Alerting System

Okeke Remigius Obinna[1], Ehikhamenle Mathew[2]

[1]Department of Electrical/Electronic Engineering, University of Port Harcourt, Nigeria
Email: remigius.okeke@uniport.edu.ng
[2] Department of Electrical/Electronic Engineering, University of Port Harcourt, Nigeria
Email : mathew.ehikhamenle@uniport.edu.ng

Received: 03 Jan 2023,

Receive in revised form: 08 Feb 2024,

Accepted: 17 Feb 2024,

Available online: 26 Feb 2024

***Keywords*— IoT, mobile app, flood, alert system, ESP32**

***Abstract*—** *This study aims to develop and implement an Internet of Things (IoT) based early flood detection system that utilizes weather API parameters to trigger SMS alerts. The system employs an ESP32 microcontroller, integrated with sensing circuitry to measure water levels, and a GSM module responsible for sending timely SMS alerts to both residents and emergency response units in the event of critical flooding. Additionally, the system incorporates a liquid crystal display (LCD) to indicate the current system status and provide real-time weather parameter readings from the digital temperature and humidity module 11 (DHT11). To facilitate efficient monitoring and data access, the system is integrated with the Blynk mobile app, which offers unrestricted access to real-time water level and weather parameter data for both the controller chief and the forecasting unit.*

I. INTRODUCTION

Flood is defined as the inundation of substantial volumes of water onto normally dry land, and is regarded as one of the most severe types of natural disasters. It is primarily triggered by heavy rainfall, the overflow of rivers or lakes, the absence of proper drainage systems, and the rapid melting of snow or the impact of storm surges resulting from tropical cyclones or tsunamis in coastal areas. Floods can vary significantly in magnitude, ranging from a few inches to several feet of water [1]. The consequences of flooding can be severe, leading to hardships, damage to crops, loss of life, and extensive destruction of both private and public property.

According to Eric Holdeman, an emergency management writer, there are five common types of floods: river flood, coastal flood, storm surge, inland flooding, and flash flood [2]. Some floods manifest suddenly and recede rapidly, while others develop gradually over several days or even months, owing to variations in size, duration, and affected area [3].

Nigeria faces a considerable risk of flooding, with this natural disaster being the most prevalent in the country. In 2012, Nigeria suffered a total loss of 16.9 billion US dollars, 363 fatalities, and displacement of 2.3 million people from their homes due to flooding, as reported by the National Emergency Management Agency (NEMA) [4]. The three primary forms of flooding in Nigeria are coastal, river, and urban flooding [5]. Factors contributing to flooding in Nigeria include poor or non-existent drainage systems, inadequate waste disposal and management, unregulated urbanization, weak implementation of planning laws, and corruption, as explained by Adaku Jane Echendu, an environment researcher in The Conversation Africa 2022 [6].

Given the devastating effects of floods, flood disaster management becomes crucial. This management process encompasses several phases, including preparedness,

prevention, response, and mitigation [7]. The preparedness phase focuses on minimizing damages through prompt and efficient response strategies, such as prediction and risk zone identification, which can be facilitated by the development of an early flood detection system. The prevention phase involves early forecasting, monitoring, and the formulation of contingency plans before or during an event. The response and mitigation phases encompass activities undertaken after a flood disaster, such as damage assessment, controlling floodwater movement, and relief management, as stated by Glago Frank in [7].

Flood detection and alerting systems play a vital role in predicting potential flood-prone areas and issuing warning messages via SMS to emergency response units and residents of those regions [8]. By leveraging these systems, the impact of flooding can be mitigated, human lives safeguarded, and socio-economic losses reduced.

Furthermore, floods represent a formidable natural disaster with severe consequences, causing extensive economic damage, loss of human lives, threats to other species, and property destruction. In Nigeria, flooding stands as the most common and impactful disaster. The implementation of flood detection systems can greatly aid in predicting flood occurrences, thereby enabling proactive measures to safeguard lives and mitigate socio-economic losses.

II. LITERATURE REVIEW

A series of reviews focusing on flood detection techniques were conducted in the past, often as part of research papers and technical reports covering various geographical regions.

Ankesh Suresh Patil et al [9] developed a flood monitoring system utilizing Arduino. The hardware components included Arduino Uno, water float sensors, an ultrasonic sensor, LED, GSM module, liquid crystal display, and buzzer. The system measured water-levels on roads using the ultrasonic and float sensors, and the data was processed by Arduino Uno and displayed on the LCD. In case of a flood, the GSM module sent SMS alerts to residents until water levels returned to normal. Limitations were identified with the ultrasonic sensor and ZP2058 float switch sensor used for water level measurement due to their restricted measurement range and potential inaccuracies.

Muhammad Ahmad Baballe [10] conducted a comparative study of flood detection systems utilizing Arduino Uno, an ultrasonic sensor, GSM module, LCD, and buzzer. Water levels were measured by the ultrasonic sensor, and when they exceeded the threshold, the microcontroller triggered the GSM module to send SMS alerts to flood-prone areas. The limitation of the study was also the use of the ultrasonic sensor for water level measurement, with its limited range and susceptibility to false readings.

A. Vijaya Lakshmi et al [11] developed an IoT early flood detection and alerting system using Arduino Uno, an ultrasonic sensor, float sensor, flow sensor, and humidity sensor. These sensors were combined to predict floods and interfaced with Arduino Uno. In the event of a potential flood, authorities and nearby villages were notified via IoT with an alarm through a Wi-Fi module. The limitation was attributed to the use of the ultrasonic sensor for water level monitoring, with its constrained measurement range and susceptibility to false readings due to obstructions.

Ange Josiane Uwayisenga [12] created an IoT-based system for automated floodwater detection and early warning in East Africa. The system included an ultrasonic sensor, DHT22 temperature and humidity sensor, Arduino Uno microcontroller, GSM module, buzzer, and LCD. The ultrasonic sensor measured the distance to the water surface, while the DHT22 sensor measured temperature and humidity. The microcontroller processed the data and sent SMS notifications to alert local authorities, and the buzzer produced an alarm for the community near flood-prone areas. The limitation was related to the use of the ultrasonic sensor for water level monitoring, which had a limited range and could provide false readings when obstructed.

Jasmin Maurya [13] designed a flood avoidance system using IoT with Arduino Uno microcontroller, Wi-Fi module, DHT11 temperature and humidity sensor, water flow sensor, ultrasonic sensor, and LCD. The ultrasonic sensor detected water levels, while the DHT11 sensor measured temperature and humidity. The water flow sensor monitored water transfer. The system's data was displayed on the LCD, and IoT connectivity was provided through the Wi-Fi module. Limitations were identified with the use of the ultrasonic sensor for water level measurement, given its limitations in range and sensitivity to temperature variations.

Minakshi Roy et al [14] implemented a flood detector and water monitoring system using IoT with Arduino Wemos D1 R1, ultrasonic sensor, flow sensor, DHT11, float sensor, and liquid crystal display. The ultrasonic sensor measured water height, the flow sensor measured flow rate, and the DHT11 sensor measured temperature and humidity. The float sensor acted as a switch to send data to Arduino Wemos D1 R1, which triggered SMS alerts to an android application. Limitations were attributed to the use of the ultrasonic sensor and float

sensor for water level measurement, with the latter not precisely indicating water level height.

Wan Hassan et al [15] designed a flood indicator water level monitoring system with Arduino Uno, GSM module, ultrasonic sensor, and liquid crystal display. A float switch sensor determined water levels and sent data to Arduino Uno, which controlled the GSM module to send SMS alerts to authorities and the public. The limitation was the water measuring device, ZP2508 float switch sensors, which only detected rising water levels without precisely measuring height.

J.G. Natividad and J.M Mendez [16] built a flood monitoring and early warning system with an ultrasonic sensor, GSM module, and Arduino microcontroller. The ultrasonic sensor measured water distance, and when it exceeded the set threshold, the microcontroller triggered the GSM module to send warning alerts to response agencies. The limitation was the use of the ultrasonic sensor for water level measurement, which had limited range and was sensitive to temperature variations.

Yasir Hashim et al [17] designed a wireless flood monitoring system with an ultrasonic sensor for water level detection. GSM module and Bluetooth module were used for communication, and an MS-190 mini motor siren alerted locals during critical water levels. Limitations were attributed to the use of the ultrasonic sensor for water level measurement due to its limited detection range and sensitivity to obstructions.

Sukanth Behera and Saradiya Kishore Parida [18] developed an IoT-based flood monitoring and alerting system using Arduino Uno with rain sensor, water level sensor, and GPS. The Arduino Uno sent information or notification alerts to nearby villages and higher authorities based on sensor data. The limitation was the use of the water level sensor, which wasn't designed for submersion, leading to a short lifespan.

Dedi Satria et al [19] designed a google maps-based flood monitoring system with Arduino Uno, GSM module, ultrasonic sensor, and GPS U-Blox Neo 6 Module. Ultrasonic sensor measured water level, and GPS provided coordinates of the flood location to Arduino Uno, which sent data through SMS to an information system station. Limitations were related to the water level measuring device, the ultrasonic sensor, due to its limited detection range and sensitivity to temperature variations.

Amit Kumar et al [20] built an IoT-based early flood detection and precaution system with Arduino Uno, ultrasonic sensor, flow rate sensor, DHT11, ESP285 Wi-Fi module, and liquid crystal display. The ultrasonic sensor measured water level height, and data was uploaded to a cloud database for viewing on an android application. Limitations were attributed to the use of the ultrasonic sensor for water level measurement, given its limited range and sensitivity to obstructions.

Edwin et al [21] designed a flood detector using Arduino Yun microcontroller, ultrasonic sensor, LED, solar power bank, and camera. The ultrasonic sensor measured flood height, and the camera provided live stream feeds. Limitations were identified with the ultrasonic sensor for water level measurement due to its limited range and susceptibility to obstructions.

III. RESEARCH METHODOLOGY

An early flood detector is a comprehensive device designed for the prediction and detection of floods. It encompasses distinct units, including the sensing unit, processing unit, communication and display unit, and integration with the Blynk mobile app.

The sensing unit comprises a calibrated floater and a DHT11 module. The calibrated floater is equipped with a floater attached to a potentiometer, enabling precise water level measurements. Two thresholds are set within the floater, with the first threshold indicating a rising water level and the second threshold indicating a critical water level. The DHT11 module measures real-time weather parameters, including temperature and humidity, which are forwarded to the weather application programming interface (API) databank for analysis and weather predictions at specific geographical locations.

The communication and display unit includes a liquid crystal display, a buzzer, GSM module, and Blynk mobile app integration. The liquid crystal display presents essential information such as water level, temperature, and humidity values. The buzzer generates an alarm to alert operators at the control room when the water level surpasses the first threshold, signaling increased attention to rising water levels, though not necessarily indicating a flood situation. On the other hand, the SMS alert function, managed by the SIM800 GSM module, is triggered when the water level exceeds the second threshold, clearly indicating a flood. It initiates warning SMS messages to notify residents in the area, urging early evacuation to safeguard lives and valuable properties. Additionally, SMS alerts are sent to the emergency response unit, preparing them to respond promptly to potential life-threatening situations.

The system is powered by a 7.5-volt rechargeable direct current (DC) battery. To ensure the appropriate voltage supply of 5 volts for each component, a buck converter is utilized, effectively regulating the voltage. This precautionary measure safeguards the components

and circuit boards from potential failure and hazards, such as fire, that may arise due to excessive voltage.

Furthermore, the flood detector system is seamlessly integrated with the Blynk mobile app, providing the chief controller and forecast unit with unrestricted access to real-time data on water levels and weather parameters via their mobile phones. This integration facilitates faster rainfall predictions and overcomes geographical limitations, allowing access to real-time water level and weather information from outside the control room.

This section presents the design methodology employed in this study, outlining the constituent units comprising the system. Furthermore, this section expounds upon the flowchart algorithm and presents the block and circuit diagrams of the work, adopting a Top-down approach for clarity and coherence. The overall system design is represented in the Diagram seen in fig. 1 below.

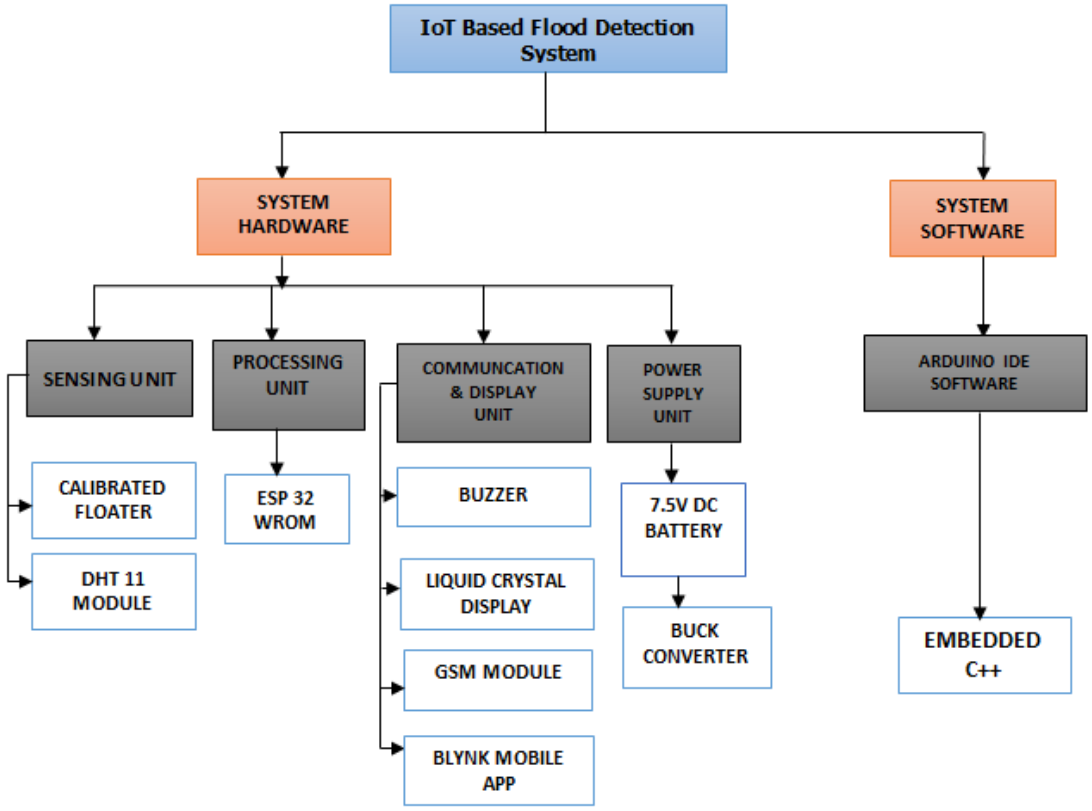

Fig. 1: Block Diagram of the IoT Flood Detection system.

1.1 Hardware (equipment) Used

1. ESP 32 WROM microcontroller
2. Floater
3. 10 Kilo ohms potentiometer
4. DHT 11 module
5. Buzzer
6. 16x2 liquid crystal display
7. SIM 800 GSM module
8. Smartphone with Blynk app installed
9. 7.5v rechargeable DC battery
10. Plastic bowl
11. Knockout box
12. Switch
13. Buck converter

From the datasheet, table 1 describes the common operating voltage required by the components and their respective current rating.

Table 1: Component Voltage and Current Specification

S/N	Component	Voltage rating (V)	Current rating(mA)
1	DHT 11	5	2.5
2	ESP 32	5	1200
3	Buzzer	5	20
4	LCD	5	1.5

5	SIM 800 GSM	5	1500

The following calculations were performed to determine the kind of power supply which depends on the total voltage and current required to efficiently power the circuit.

The determination of the total voltage required to power the circuit is based on the common operating voltage rating obtained from the datasheets of the individual components. As indicated in the component description provided table 1, each component necessitates a 5-volt input, thus establishing the minimum voltage required for the entire circuit as 5 volts. Given that the components are connected in parallel, the voltage supplied to each component remains consistent:

Vtotal = VDHT11 = VESP32 = VBuzzer = VLCD = VGSM = 5 volts.

To meet this voltage requirement, two 3.75-volt lithium batteries are utilized, chosen based on material availability. These batteries are connected in series, producing a total voltage of 7.5 volts. To ensure proper regulation of the voltage input to the various components, a buck converter is integrated into the power supply. This converter serves the crucial function of maintaining a stable 5-volt supply, enabling the efficient and safe operation of the circuit.

The total current required for the circuit is determined by summing the individual current ratings of the various components, as they are connected in parallel. Although the ESP 32 microcontroller features a 5V pin that could potentially power interfaced components, it was not directly utilized for this purpose to ensure optimal performance. This decision was based on the fact that the total current rating of the components surpasses the maximum output current of the microcontroller.

The batteries, connected in parallel, possess the same current rating. Specifically, each battery has a current rating of 3800mAh. This rating exceeds the total current required to power the circuit, ensuring sufficient capacity to effectively operate the system.

The calculation of the total current (Itotal) is as follows:

Itotal = IDHT11 + IESP32 + IBuzzer + ILCD + IGSM

Itotal = 2.5mA + 1200mA + 20mA + 1.5mA + 1500mA = 2724mA

Considering the individual current ratings and the capacity of the batteries, they serve as suitable power sources for the circuit, enabling its effective functionality. The circuit diagram for the hardware is shown in fig. 2.

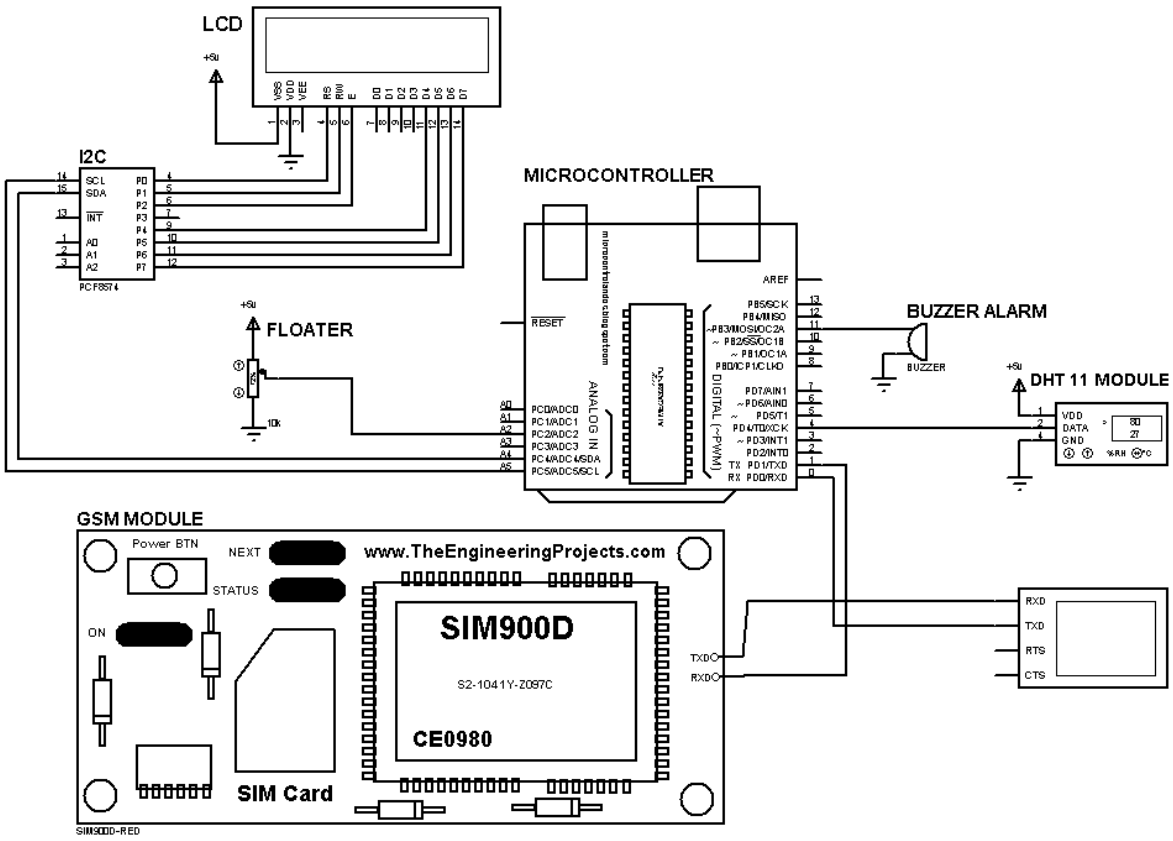

Fig. 2: Circuit Diagram of the System.

1.2 System Software

The ESP 32 WROM microcontroller utilized in this research was programmed using the embedded C++ programming language. C++ is a favored choice for developing software for microcontrollers due to its efficiency and extensive features that facilitate the creation of both simple and complex programs. Embedded C++ serves as a high-level programming language, whereas the native language understood by microcontrollers is machine language. To program the microcontroller using a high-level language, a compiler is essential to translate the high-level code into machine language. Consequently, an Integrated Development Environment (IDE) becomes crucial for this purpose.

An IDE is a software application that offers a comprehensive set of tools to assist programmers in writing, debugging, and maintaining software. These tools typically encompass a source code editor, a compiler or interpreter, a debugger, and various utilities for control, testing, and profiling. IDEs play a pivotal role in streamlining the development process, providing a cohesive environment for programming microcontrollers effectively. They can be tailored for specific purposes or used as general-purpose development platforms.

Arduino is a widely adopted open-source platform designed for creating electronics researches. The Arduino Software (IDE) is a free software application that operates on a computer, enabling users to write programs and subsequently upload them to the physical Arduino board. The IDE encompasses a text editor, compiler, and programmer, providing a comprehensive toolkit for programming convenience.

This section serves as a valuable reference for developers during the programming process. Moreover, the Arduino IDE can be enhanced to accommodate the ESP 32 Board through the Board Manager feature, allowing for seamless programming and code upload to the ESP microcontroller. By incorporating the ESP 32 Board, users can leverage its capabilities in conjunction with the familiar Arduino programming environment, enabling the development of sophisticated electronics projects.

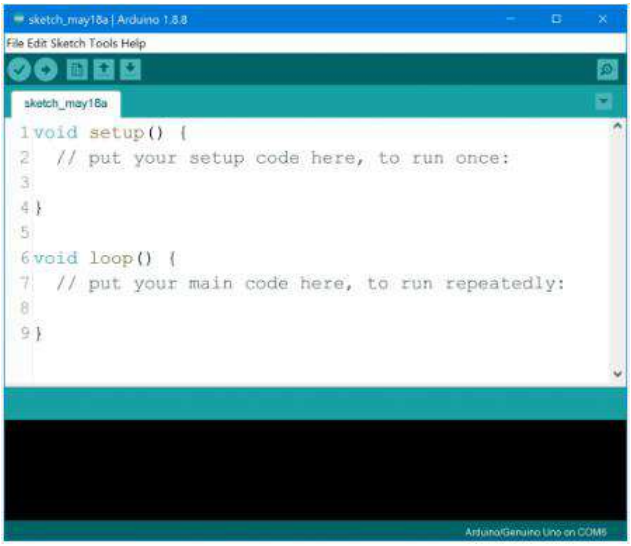

Fig. 3: Arduino IDE Interface

1.3 Flowchart Algorithm

The flowchart diagram in fig. 4 illustrates the step-by-step algorithm followed by the system. Upon activation, the sensors read water level, temperature, and humidity analogue values, which are subsequently transmitted to the microcontroller as inputs. The microcontroller then converts these analogue values into digital signals and outputs them on both the LCD and the Blynk app.

Next, the system measures the water height against two distinct thresholds. If neither threshold condition is met, the microcontroller continues to display the water level on the LCD. However, if the first threshold is met, the buzzer is triggered, and a caution message is displayed on the LCD every 2 seconds, accompanied by the water level, temperature, and humidity values.

In the event that the second threshold is met, the buzzer is again triggered, but this time a warning message is displayed on the LCD every 2 seconds, alongside the water level, temperature, and humidity values. Additionally, the system activates the GSM module to send a warning SMS to the residents of the affected area, the emergency response unit, and the government.

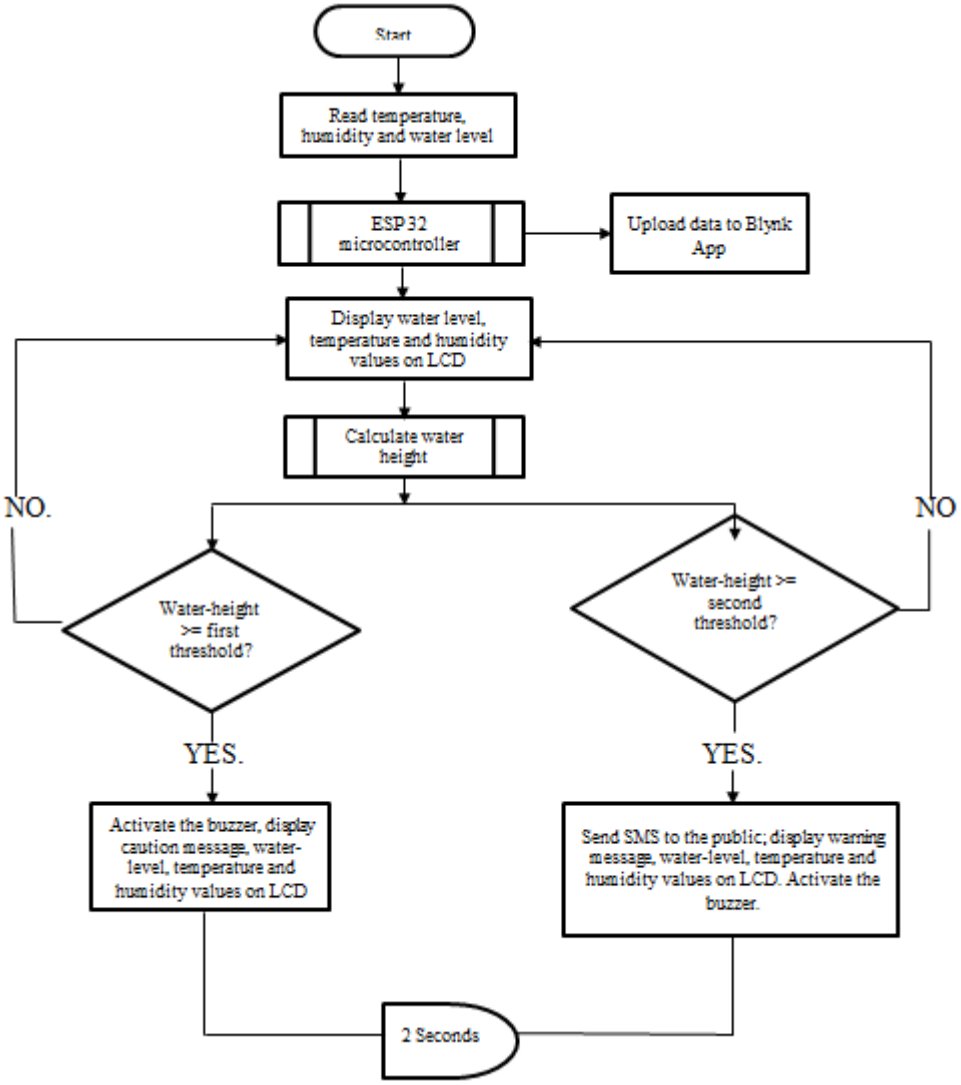

Fig.4: Flowchart Diagram

IV. RESULTS AND DISCUSSION

The proposed flood detector system underwent simulation to assess its viability and significance prior to the actual construction. The simulation process was carried out utilizing Proteus 8 Professional software as shown in the figure 6. The complete system development is partitioned into distinct hardware and software components. By constructing and testing individual segments of the system, the process achieved enhanced speed, efficiency, and minimized debugging time.

Prior to conducting the test, a thorough inspection of the battery was performed to ascertain if there was any physical damage. Subsequently, the batteries underwent individual testing, as well as testing while connected in series, to verify that they were capable of providing the necessary voltage and current required by the circuit. The battery test was conducted using a digital multi-meter as shown in fig. 5.

Fig. 5: Battery Test showing the Measured Voltage.

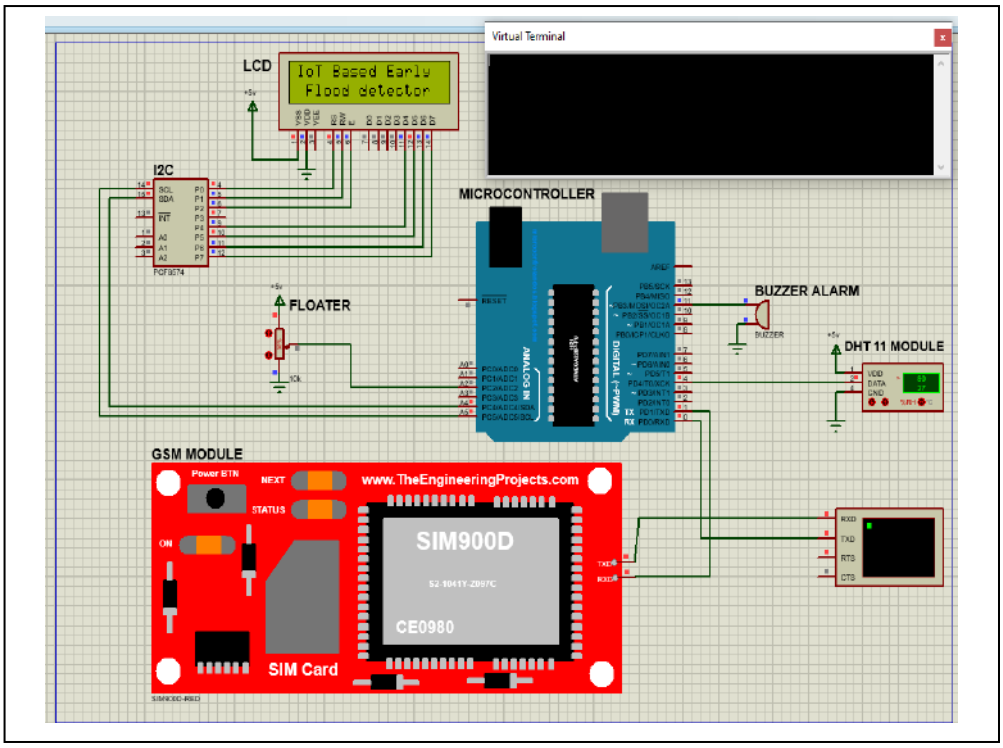

Fig. 6: Proteus Screenshot showing System simulation

Once the system is powered, it immediately measures water-level, temperature and humidity values. The initial threshold is activated when the water level surpasses 20 meters but remains below 44 meters. In such cases, a caution message will be exhibited on the LCD, and the buzzer alarm will be activated. Individual testing of each sensor was conducted to verify the accuracy of their water-level, temperature, and humidity readings, as well as to ensure their proper connection to the circuit. Additionally, the functionality of the sensor values and the warning messages displayed on the LCD was also examined through testing. Simulated and real test are shown in fig. 7.

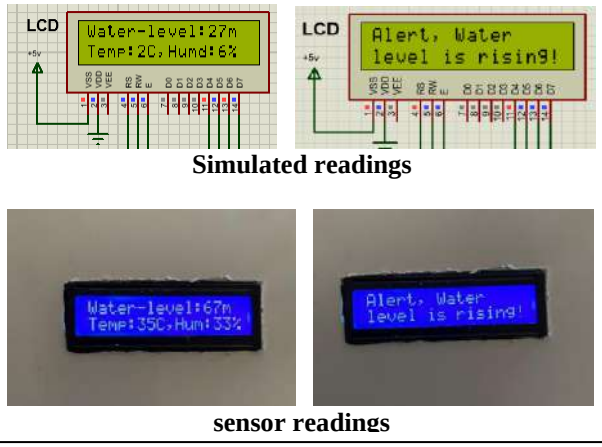

Fig. 7: 1st threshold results

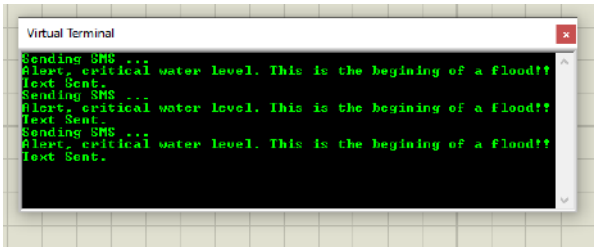

Simulated Virtual Terminal (Screen) displaying the sent SMS.

Display of the SMS Alert Message

Fig. 8: 2nd threshold results

The second threshold is reached when the water level rises to 45 meters and above. At this point, the system will activate the buzzer alarm, display a warning message on the LCD, and the GSM module will be utilized to send warning messages to both the emergency response units and the residents within that area. A comprehensive test was performed on the SIM800 GSM module to verify its

proper functioning in sending alert messages to the pre-programmed phone numbers when the second threshold value is triggered. Both simulated and real-time results are depicted in the accompanying figures. Both simulated and real test are shown in fig. 8.

The data synchronization of the sensor and floater values to the Blynk cloud were tested to ensure accurate display in the Blynk app.

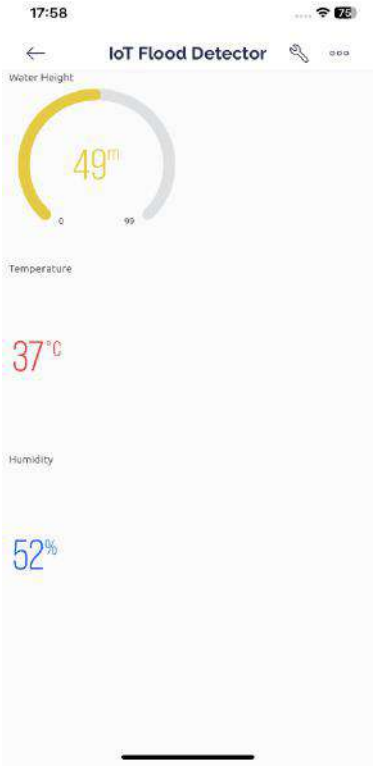

Fig. 8: Displaying Sensor Values in the Blynk App

V. CONCLUSION

This study presents the successful development and realization of a fully functional Internet of Things (IoT) based early flood detection and alerting system, integrating weather application programming interface (API) parameters. This prototype has demonstrated its efficacy in saving lives, protecting properties, and minimizing damages caused by flood disasters. To enhance flood management and mitigation efforts in Nigeria, it is imperative that responsible agencies, such as the Nigeria Hydrological Services Agency (NIHSA), the National Emergency Management Agency (NEMA), and other local government agencies and disaster management organizations across the states, equip themselves with this IoT flood detector and alerting systems. These systems enable effective real-time monitoring of water levels, facilitating proactive responses to potential flood events.

One notable contribution of this work to the existing body of research on flood detection systems lies in the incorporation of a calibrated floater for accurate water level measurement, SMS alert functionality, and real-time monitoring of water height, temperature, and humidity using the Blynk app.

Based on the observations made during the study, certain recommendations have been identified to further improve the system's performance. Firstly, integrating a solar panel with a battery can extend the system's operational duration, ensuring prolonged functionality even during extended periods of low sunlight. Secondly, the development of a third-party IoT app that provides water level data and weather forecasts to the general public without user restrictions, as opposed to the limited information sharing capabilities of the Blynk app, would enhance accessibility and outreach.

Moreover, the system's accuracy and efficiency can be enhanced by utilizing a custom-made spherical calibrated floater for water level measurement, as it offers better water displacement, thereby contributing to more precise readings.

In conclusion, the implementation of this IoT based early flood detection and alerting system, equipped with weather API parameters, offers significant potential to safeguard lives, protect properties, and mitigate flood-related damages. The integration of such systems by relevant agencies and the adoption of recommended improvements hold the promise of enhancing flood management practices and disaster response capabilities.

REFERENCES

[1] Hirsch, R. M., & Ryberg, K. R. (2012). Has the magnitude of floods across the USA changed with global CO2 levels? *Hydrological Sciences Journal*, *57*(1), 1-9.

[2] Holdeman, E. E. (2023). Emergency Management's Journey with Technology. In *Disaster Management and Information Technology: Professional Response and Recovery Management in the Age of Disasters* (pp. 3-23). Cham: Springer International Publishing.

[3] Yang, H., Wang, H., Lu, J., Zhou, Z., Feng, Q., & Wu, Y. (2021). Full lifecycle monitoring on drought-converted catastrophic flood using sentinel-1 sar: A case study of poyang lake region during summer 2020. *Remote Sensing*, *13*(17), 3485.

[4] Danhassan, S. S., Abubakar, A., Zangina, A. S., Ahmad, M. H., Hazaea, S. A., Ishak, M. Y., & Zhang,

J. (2023). Flood Policy and Governance: A Pathway for Policy Coherence in Nigeria. *Sustainability*, *15*(3), 2392.

[5] Ajumobi, V. E., Womboh, S. B., & Ezem, S. B. (2023). Impacts of the 2022 flooding on the residents of Yenagoa, Bayelsa State, Nigeria. *Greener Journal of Environmental Management and Public Safety*, *11*(1), 1-6.

[6] Echendu, A. J. (2023). Human factors vs climate change; experts' view of drivers of flooding in Nigeria. *Natural Hazards Research*, *3*(2), 240-246.

[7] Glago, F. J. (2021). Flood disaster hazards; causes, impacts and management: a state-of-the-art review. *Natural hazards-impacts, adjustments and resilience*, 29-37.

[8] Subashini, M. J., Sudarmani, R., Gobika, S., & Varshini, R. (2021, February). Development of Smart Flood Monitoring and Early Warning System using Weather Forecasting Data and Wireless Sensor Networks-A Review. In *2021 Third International Conference on Intelligent Communication Technologies and Virtual Mobile Networks (ICICV)* (pp. 132-135). IEEE.

[9] Patel, A., Kumar, A., Singh, S., Rani, R., & Usmani, M. H. (2022). IOT Based Early Flood Detection and Avoidance. *Available at SSRN 4159183*.

[10] Baballe, M. A., & Abbati, Z. A. (2022). A Review of Flood Detection Systems. In *1st International Conference on Applied Engineering and Natural Sciences, Konya, Turkey May*.

[11] Lakshmi, R. A., Lakshmi, M. M., Swetha, P., & Prakash, T. D. (2020). FLOOD DETECTION AND EARLY WARNING SYSTEM.

[12] Uwayisenga, A. (2021). *IoT-based system for automated floodwater detection and early warning in the East Africa Region: a case study of Arusha and Dar es salaam, Tanzania* (Doctoral dissertation, NM-AIST).

[13] Maurya, J., Pant, H., Dwivedi, S., & Jaiswal, M. FLOOD AVOIDANCE USING IOT.

[14] Roy, M., Pradhan, P., George, J., & Pradhan, N. (2020). Flood Detection and water Monitoring system using IoT. *International Journal Of Engineering And Computer Science*, *9*(07), 25113-25115.

[15] Hassan, W. H. W., Jidin, A. Z., Aziz, S. A. C., & Rahim, N. (2019). Flood disaster indicator of water level monitoring system. *International Journal of Electrical and Computer Engineering*, *9*(3), 1694.

[16] Natividad, J. G., & Mendez, J. M. (2018, March). Flood monitoring and early warning system using ultrasonic sensor. In *IOP conference series: materials science and engineering* (Vol. 325, No. 1, p. 012020). IOP Publishing.

[17] Hashim, Y., Idzha, A. H. M., & Jabbar, W. A. (2018). The design and implementation of a wireless flood monitoring system. *Journal of Telecommunication, Electronic and Computer Engineering (JTEC)*, *10*(3-2), 7-11.

[18] Behera, S., & Parida, S. K. (2018). IoT-based Flood Monitoring and Alerting System using Arduino Uno. *Turkish Journal of Computer and Mathematics Education (TURCOMAT)*, *9*(3), 702-706.

[19] Satria, D., Yana, S., Munadi, R., & Syahreza, S. (2017). Prototype of Google maps-based flood monitoring system using Arduino and GSM module. *Int. Res. J. Eng. Technol*, *4*(10), 1044-1047.

[20] Kumar, M. A., Singh, V., Chaubey, V. K., Bisht, V. S., & Sharma, S. (2016). Iot Based Flood Detector and Early Precaution Method Instructor to Avoid Any Hazardous Event.

[21] Guadaña, R. R., Santos, R. A., De Guzman, E., Cuadra, V. S., De Luna, A. G., & Villanueva, C. (2016, May). FLood Detector System Using Arduino. In *Proceedings of 37th The IRES International Conference*.

[22] Mokwe U.V, Omijeh B.O, Eludoyin O.S, Okeke R.O (2023). Development of Flash flood warning System for Nkpolu Road, Rumuigbo Port Harcourt. Vol 8(4)

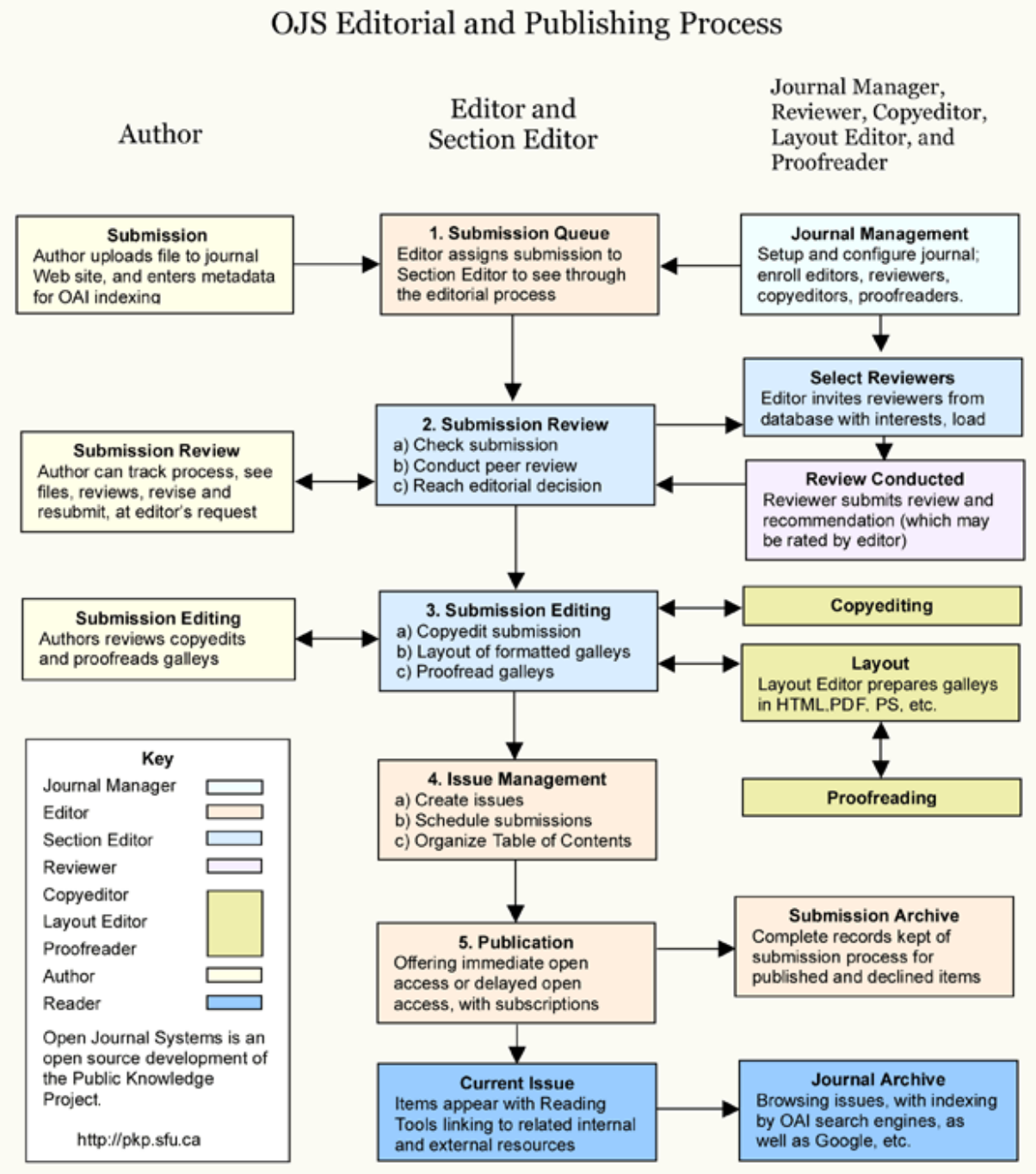

~IJAERS Workflow~

Important links:

Paper Submission Link:
https://ijaers.com/submit-paper/
Editorial Team:
https://ijaers.com/editorial-board/
Peer Review Process:
https://ijaers.com/peer-review-process/
Publication Ethics:
https://ijaers.com/publication-ethics-and-publication-malpractice-statement/
Author Guidelines:
https://ijaers.com/instruction-to-author/
Reviewer Guidelines:
https://ijaers.com/review-guidelines/

Journal Indexed and Abstracted in:

- Qualis-CAPES (A2)-Brazil
- Normatiza (Under Review-Ref.020191511)
- NAAS Score: 3.18
- Bielefeld Academic Search Engine(BASE)
- Aalborg University Library (Denmark)
- WorldCat: The World's Largest Library Catalog
- Semantic Scholar
- J-Gate
- Open J-Gate
- CORE-The world’s largest collection of open access research papers
- JURN
- Microsoft Academic Search
- Google Scholar
- Kopernio - powered by Web of Science
- Pol-Index
- PBN(Polish Scholarly Bibliography) Nauka Polaska
- Scilit, MDPI AG (Basel, Switzerland)
- Tyndale University College & Seminary
- Indiana Library WorldCat
- CrossRef DOI-10.22161/ijaers
- Neliti - Indonesia's Research Repository
- Journal TOC
- WIKI-CFP
- Scinapse- Academic Search Engine
- Mendeley-Reference Management Software & Researcher Network
- Dimensions.ai: Re-imagining discovery and access to research
- Index Copernicus Value(ICV): 81.49
- Citeseerx
- Massachusetts Institute of Technology (USA)
- Simpson University (USA)
- University of Louisville (USA)
- Biola University (USA)
- IE Library (Spain)
- Mount Saint Vincent University Library (Halifax, Nova Scotia Canada)
- University Of Arizona (USA)
- INDIANA UNIVERSITY-PURDUE UNIVERSITY INDIANAPOLIS (USA)
- Roderic Bowen Library and Archives (United Kingdom)
- University Library of Skövde (Sweden)
- Indiana University East (campuslibrary (USA))
- Tilburg University (The Netherlands)
- Williams College (USA)
- University of Connecticut (USA)
- Brandeis University (USA)
- Tufts University (USA)
- Boston University (USA)
- McGill University (Canada)
- Northeastern University (USA)
- BibSonomy-The blue social bookmark and publication sharing system
- Slide Share
- Academia
- Archive
- Scribd
- ISRJIF
- Cite Factor
- SJIF-InnoSpace
- ISSUU
- Research Bib
- infobaseindex
- I2OR
- DRJI journal-repository

AI Publication
International Journal of Advanced Engineering Research and Science (IJAERS)
104/108, Sector-10, Pratap Nagar, Jaipur, India